THESIS

TWO-STAGE DEVELOPMENT OF THE WIND RIVER BASIN, WYOMING: LARAMIDE SHORTENING FOLLOWED BY POST-LARAMIDE REGIONAL EXTENSION, LOCALIZED BACKSLIDING, AND ARCH COLLAPSE

Submitted by

Ryan Curtis Thompson

Department of Geosciences

In partial fulfillment of the requirements

For the Degree of Master of Science

Colorado State University

Fort Collins, Colorado

Spring 2010

COLORADO STATE UNIVERSITY

April 2, 2010

WE HEREBY RECOMMEND THAT THE THESIS PREPARED UNDER OUR SUPERVISION BY RYAN CURTIS THOMPSON TITLED “TWO-STAGE DEVELOPMENT OF THE WIND RIVER BASIN, WYOMING: LARAMIDE SHORTENING FOLLOWED BY POST-LARAMIDE REGIONAL EXTENSION, LOCALIZED BACKSLIDING, AND ARCH COLLAPSE” BE ACCEPTED AS FULFILLING IN PART REQUIREMENTS FOR THE DEGREE OF MASTER OF SCIENCE.

Committee on Graduate work

_____
J. Antonio H. Carraro

_____
Derek L. Schutt

_____
Dean P. DuBois

_____
Advisor: Eric A. Erslev

_____
Department Head: Sally J. Sutton

ABSTRACT OF THESIS

TWO-STAGE DEVELOPMENT OF THE WIND RIVER BASIN, WYOMING: LARAMIDE SHORTENING FOLLOWED BY POST-LARAMIDE REGIONAL EXTENSION, LOCALIZED BACKSLIDING, AND ARCH COLLAPSE

This study addressed mechanisms and timing of fracture development in basement-involved foreland basins. Fracture analyses were used to test hypotheses for the structural development of the Wind River Basin in central Wyoming. Current debates in the Rocky Mountains of North America include the mechanisms and timing of fracture development and how the fractures relate to the Laramide Orogeny, which was responsible for the bulk of Phanerozoic deformation in the region. These fracture systems have important implications, especially for hydrocarbon recovery.

This study tested hypotheses for fracture mechanisms and timing, including fracturing due to: 1) pre-Laramide distal compression or forebulge migration during the Sevier Orogeny; 2) syn-Laramide east-northeast directed horizontal compression; and 3) multiple post-Laramide hypotheses for fracture development including: i) near-surface topographic collapse and exhumation; ii) elastic strain release following Laramide shortening; iii) left-slip faulting resulting

in the basin's trapezoidal shape; iv) broad regional extension due to extensional plate interactions or epierogenic uplift; and v) localized extension coupled to backsliding on listric thrust faults and collapse of basin-bounding arches.

Multiple datasets of fractures were analyzed and eigenvectors were used to calculate the inferred axes of the stresses responsible for the deformation in the Wind River Basin. These datasets included 1447 fault strike segments digitized from geologic maps, 9107 subsurface fractures previously interpreted by log analysts from micro-resistivity image logs from 23 wells, and 1833 joints and minor faults measured at 42 stations in outcrops of Cambrian to Eocene units from throughout the basin.

Timing relationships and ideal σ_1 and inferred σ_3 results indicate two distinct fracture sets. The first set consists of 135 strike-slip faults and 330 thrust faults and was found in Cambrian through lower Eocene units. Using ideal σ_1 analysis for this set, a mean N66°E-trending, bedding-parallel maximum compressive stress was calculated, consistent with shortening due to the Laramide Orogeny.

The second set consists of 546 normal faults, one recent earthquake's previously calculated fault plane solution, 617 systematic joints, and the 9107 subsurface fractures. Timing relationships observed in the field indicate that these fractures are younger than those in set one. They were found in Cambrian through upper Eocene units and include modern fractures. Two distinct fracture strikes were observed in both the natural and modern fractures in this set, northwest-southeast and east-west. Eigenvector analyses indicate a N44°E-

trending minimum compressive stress from fractures with northwest-southeast strikes and a N7°E-trending minimum compressive stress from fractures with east-west strikes.

Previous workers have documented northwest-southeast-striking joints across Wyoming and Colorado, supporting the hypothesis of regional post-Laramide extension for these fractures. East-west-striking fractures, however, are parallel to, and localized in proximity to the northern and southern basin-bounding faults. The correlation between set two fracture strikes and the strike of the closest basin-bounding fault suggests a coupling of these features.

In conclusion, the thrust and strike-slip faults in set one are consistent with ENE-WSW Laramide horizontal shortening, and the normal faults and systematic joints in set two are consistent with post-Laramide extension. The two calculated stress axes from the post-Laramide fractures supports a combination of regional northeast-southwest extension, which may have unloaded Laramide arches bounding the basin and localized north-south extension coupled to backsliding on listric thrust faults and collapse of basin-bounding arches.

Ryan Curtis Thompson
Department of Geosciences
Colorado State University
Fort Collins, CO 80523
Spring 2010

ACKNOWLEDGEMENTS

Much appreciation goes to my advisor: Eric Erslev; my committee: Dean DuBois, Derek Schutt, and Antonio Carraro; and the department for their commitment to, and support of the project and myself.

Also greatly appreciated is EnCana Oil & Gas (USA) Inc. for funding my research stipend, tuition, and an integrated internship through the Wind River Basin team under the guidance of Dean DuBois & Terri Olsen.

The following are appreciated for funding a successful field season: Rocky Mountain Association of Geologists (Norman H. Foster Memorial Scholarship), American Association of Petroleum Geologists (Allan and Eleanor Martini Named Grant), Colorado Scientific Society (Ogden Tweto Memorial Fund Research Grant), and Wyoming Geological Association (Dr. J. David Love Field Geology Fellowship).

DEDICATION

To my wife Sherelle Moné: who lovingly supported and encouraged me

To my kids Shayne & Rylie: who gave much needed diversion

To my parents: who taught me how to learn and made it fascinating

To Art Chadwick: who inspires & shares my passion for geology

To my Creator: for everything

"But the falling mountain crumbles away

And the rock moves from its place"

Job 14:18 NASB

TABLE OF CONTENTS

CHAPTER 1. INTRODUCTION

The problems addressed by this study are the mechanisms and timing of fracture development in basement-involved foreland basins. The Rocky Mountain foreland of Wyoming (Fig. 1.1) is a complex network of anastamosing arches and intervening basins that formed during the Laramide Orogeny. The mean trend of these arches is N23°W, with trends varying between east-west and north-south (Erslev & Koenig, 2009). At the center of this structural complexity is the trapezoidal Wind River Basin and associated bounding arches, located in central Wyoming.

The Wind River Basin is bounded on its western and eastern margins by typical NNW-SSE-trending Laramide arches, the Wind River Mountains and Casper Arch. East-west-trending arches, the Owl Creek and Granite Mountains, bound the northern and southern margins (Fig. 1.2). Observations from seismic data and drilling through thrust hanging walls show that these arches are underlain by low-angle, thick-skinned thrust faults involving Precambrian basement (Gries, 1983).

Fractures in foreland basins give important clues to the structural development of a region by defining the causal stress axes and the sequence of deformation (Erslev & Koenig, 2009). Previous workers in the Rocky Mountains

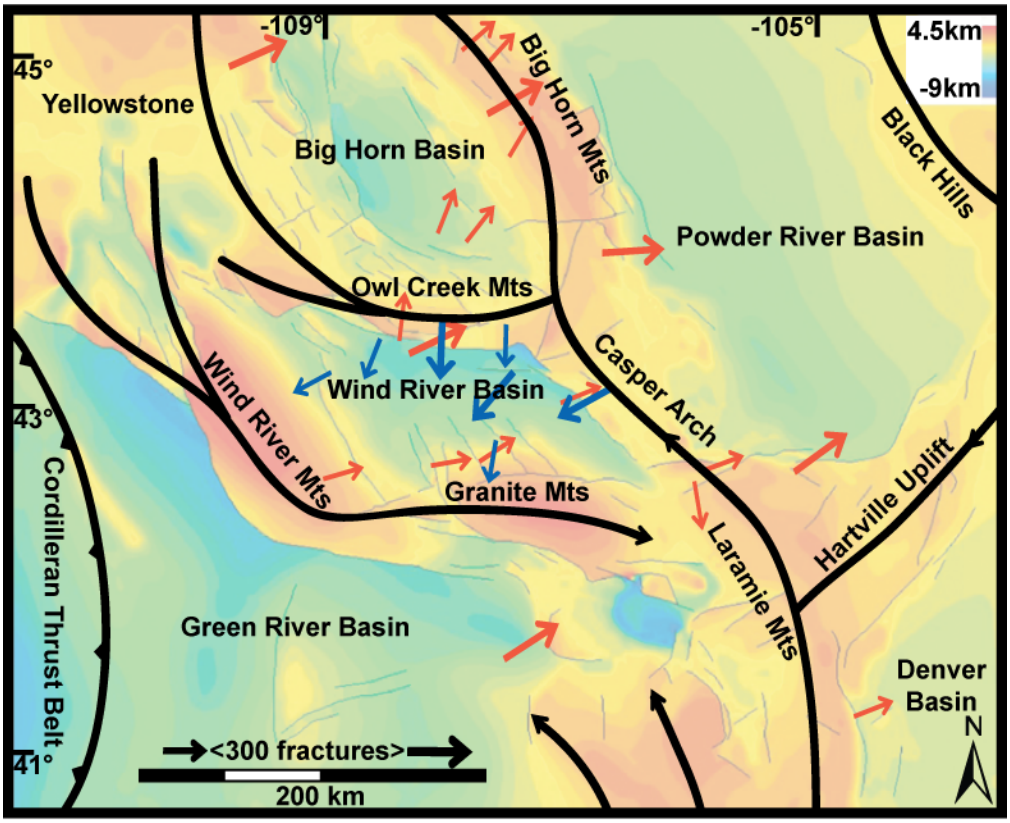

Figure 1.1 Foreland structural trends, Wyoming after Erslev & Koenig (2009) and Thompson & Erslev (2009); shortening arrows (red), extension arrows (blue); color contours from T. Neely, unpublished, based on Precambrian structure contours of Blackstone (1993).

have debated the mechanisms and timing of these fractures and how they relate to Laramide shortening (Bergh & Snoke, 1992; Varga, 1993; Paylor & Yin, 1993; Molzer & Erslev, 1995). More recent fracture studies are identifying extensional mechanisms, with debate centering on whether these fractures are pre-Laramide (Hennings et al., 2000; Bergbauer & Pollard, 2004) or post-Laramide (Ruf & Erslev, 2005; Gillett, 2009).

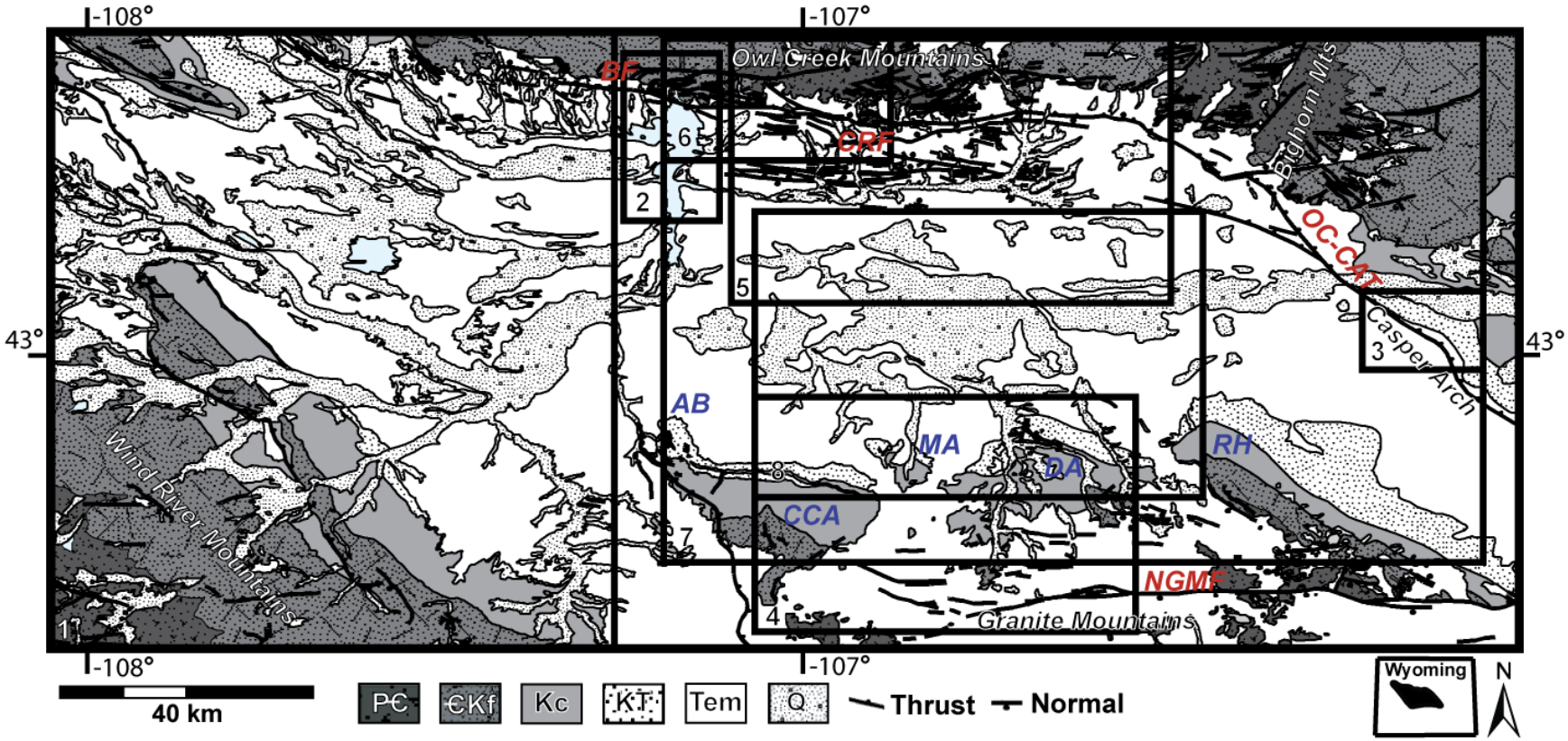

Figure 1.2 Wind River Basin geology after Love & Christiansen (1985) Insets, numbered at bottom left corner of box, show location of figures in Chapters 3 & 4. Unit abbreviations: PC: Precambrian; CKf: Cambrian-Frontier; Kc: Cody Shale; KT: Mesa Verde-Fort Union; Tem: Eocene-Miocene; Q: Quarternary. Fault abbreviations: BF: Boysen; CRF: Cedar Ridge; NGMF: N. Granite Mtns; OC-CAT: Owl Creek-Casper Arch Thrust. Anticline abbreviations: RH: Rattlesnake Hills; DA: Dutton; MA: Muskrat; CCA: Conant Creek; AB: Alkali Butte.

Observations, Hypotheses, & Predictions

The following is a list of hypotheses and their associated observations and predictions related to the problems of causal mechanisms and timing of fracture development in the study area. These hypotheses were tested using calculated eigenvectors, ideal σ_1, and 2θ vector mean fracture analysis methods described in Chapter 4.

1. Pre-Laramide fracturing:

   Based on observations of northwest-southeast-striking joints in both flat-lying and folded lower Cretaceous Frontier Formation sandstone, Hennings et al. (2000) and Bergbauer & Pollard (2004) proposed that these fractures are pre-Laramide and caused by distal compression or forebulge migration during the Sevier Orogeny. This hypothesis predicts that these fractures would be limited to the pre-Laramide units older than the Maastrichthian Lance Formation and would be caused by stresses independent of Laramide compression.

2. Syn-Laramide fracturing:

   Over 21,129 minor faults from across the Rocky Mountain foreland (Erslev, 2009) have been measured and used to calculate an mean ENE-WSW horizontal maximum compressive stress for the Laramide Orogeny. This dataset includes 718 minor fault

measurements from the Owl Creek Mountains (Molzer & Erslev, 1995).

Predicted thrust faults would strike NNW-SSE and left and right-slip faults would strike east-west and northeast-southwest respectively. Predicted joints and normal faults would strike either ENE-WSW, parallel to this compression, such as the splitting fractures at Dallas Dome (Brocka, 2005); or NNW-SSE, perpendicular to this compression due to outer-arc extension along anticlinal crests (Hennings et al., 2000).

3. Post-Laramide Fracturing:

Observations of fractures in post-Laramide units and modern drilling-induced fractures have led to multiple hypotheses for post-Laramide fractures. These hypotheses predict stress axes that are inconsistent with Laramide compression.

i. Near surface mechanisms

Normal faults and joints can form in the near surface stress field due to a variety of causes that include topographic collapse, where fracture strikes would parallel steep topography such as canyon walls (Whitehead, 1997) or in association with exhumation due to epeirogenic uplift (Keefer, 1970), where fractures may infill

parallel to existing fractures or abutt them orthogonally. In all these cases, fractures would not be predicted at depth in the subsurface.

ii. Elastic strain release

Normal faulting and jointing may occur in units lithified enough to store strain due to relaxation following Laramide shortening as stored strain is released. Predicted fractures would strike NNW-SSE, perpendicular to Laramide shortening and their minimum compressive stress axis would parallel the maximum compressive stress axis calculated from Laramide fractures.

iii. East-west left-slip faulting

The trapezoidal shape of the basin has led to speculation of left-slip faulting (Keefer, 1970) and east-west left-slip faults have been interpreted from seismic data transecting the study area (Stone, 2007; P.J. Wynne, 2008, personal communication). East-west left-slip minor faults have also been observed in pre- and syn-Laramide units (Paylor & Yin, 1993; Molzer & Erslev, 1995). The hypotheses to be tested are whether left-slip faulting occurred and was post-Laramide. Strike-slip faults and ENE-WSW-striking joints and normal faults would be predicted in modern fracturing if east-west left-slip faulting continued to the present.

iv. Broad regional extension

Northwest-southeast striking joints have been observed across Wyoming and Colorado (Oil Mountain anticline: Hennings et al., 2000; Emigrant Gap anticline: Bergbauer & Pollard, 2004; San Juan Basin: Ruf & Erslev, 2005; northeast Uinta Mountains & Tow Creek anticline: Gillett et al., 2007; northeast Laramie Range & Casper Arch: Cooley, 2009; Denver Basin: C.L. Allen, 2009, personal communication; and southeast corner of the Wind River Basin: L.E. Hamlin, 2009, personal communication). Possible causes of these joints include transtensional plate interactions in the Gulf of California along with Basin and Range extension which began in the Miocene (Bird, 2002) and broad outer-arc extension, possibly due to epeirogenic, Pliocene uplift (Keefer, 1970).

Other possible causes of regional extension include mid-Eocene to Miocene collapse of the Cordilleran (Constenius, 1996), which would produce north-south-striking joints and normal faults and late Miocene or early Pliocene collapse of the Granite Mountains (Bauer, 1934; Scott, 2002) which would produce east-west-striking joints and normal faults. The hypothesis that fractures formed during post-Laramide regional extension predicts that associated fractures would have consistent strikes and would be found across the region in post-Laramide units.

v. Localized extension

East-west-striking normal faults have been observed along the southern margin of the Owl Creek arch (Fig. 1.2). These faults have a different trend than the northwest-southeast-striking joints observed in the region.

One possible cause of localized extension is orogenic collapse. Orogenic collapse has been documented globally—in the Himalayas (Burg et al., 1996; Edwards & Harrison, 1997; Zeilinger et al., 2007), and the Caledonides of Scandinavia and Ireland (Fossen, 2000; Clift et al., 2004) to the much closer collapse of the Cordilleran (Constenius, 1996). Locally, the Owl Creek and Granite Mountain arches bounding the Wind River Basin have been down-dropped (Appendix B.5 & B.6) along normal faults bounding their margins (Bauer, 1934; Wise, 1963; Keefer, 1970; Hall & Chase, 1989).

Specifically, if regional extension has unloaded Laramide arches, then their underlying thrust faults could have backslid as listric normal faults, causing their margins to collapse. Predicted fractures would include normal faults and joints that would strike parallel to thrust faulted arch margins (Thompson & Erslev, 2009).

Objectives & Methods Overview

The objectives of this study included:

1. Collecting an extensive spatial and temporal database of fractures from digitized mapped faults, micro-resistivity image logs, and outcrop measurements.
2. Categorizing these fractures as either joints or faults and determining their timing from abutting relationships, relative age of host units, and their relationships to modern stress axes.
3. Calculating and comparing stress axes responsible for the fractures using eigenvector analysis, ideal σ_1 analysis (Compton, 1966), and 2θ vector means.
4. Analyzing the relationships between subsurface and outcrop fractures and between minor fractures and larger scale structures.
5. Building a structural model, consistent with seismic data, upon which future work, such as predicting zones of higher intensity fracturing, can be based.

Previous fracture studies on the northern margin of the basin (Paylor & Yin, 1993; Molzer & Erslev, 1995) and on the eastern margin (Hennings et al., 2000; Bergbauer & Pollard, 2004) as well as more recent studies (Gillett et al., 2007; Cooley, 2009) and regional studies across the Rocky Mountains (Varga, 1993; Erslev & Koenig, 2009) have utilized similar approaches and analysis techniques to test similar problems and hypotheses.

Significance

Globally, pre-, syn-, and post-orogenic processes all play significant roles in regional structural development. Understanding the mechanisms and timing of orogenic processes at global and regional scales are important for geohazard assessment and natural resource management.

Fractures, either in reservoirs or seals, can have tremendous effects on natural resources dependant on subsurface fluid flow. Fractures may enhance, compartmentalize, or baffle fluid flow (Hennings et al., 2000). There is a wide spectrum of fluids upon which fractures may have an influence, including, but not limited to, ore-forming fluids, in-situ recovery fluids, fluids from radioactive or chemical waste storage, water, or CO_2 sequestration (Sava & Mavko, 2007). Modeling and predicting fracture systems is particularly important for exploiting uranium and hydrocarbon economic reserves in the Wind River Basin (Fig. 1.3.).

Uranium

The majority of the basin's production was from the Tertiary roll-front deposits (Rackley, 1972) of the Gas Hills district along the southern margin of the basin (Fig. 1.3). These strip mines are now being reclaimed and there are also some abandoned shaft mines located in Precambrian rocks near Copper Mountain in the eastern Owl Creek Mountains. Synchronous with this study, Neutron Energy Inc. staked claims in the Steffen Hill-Cedar Ridge area near Copper Mountain.

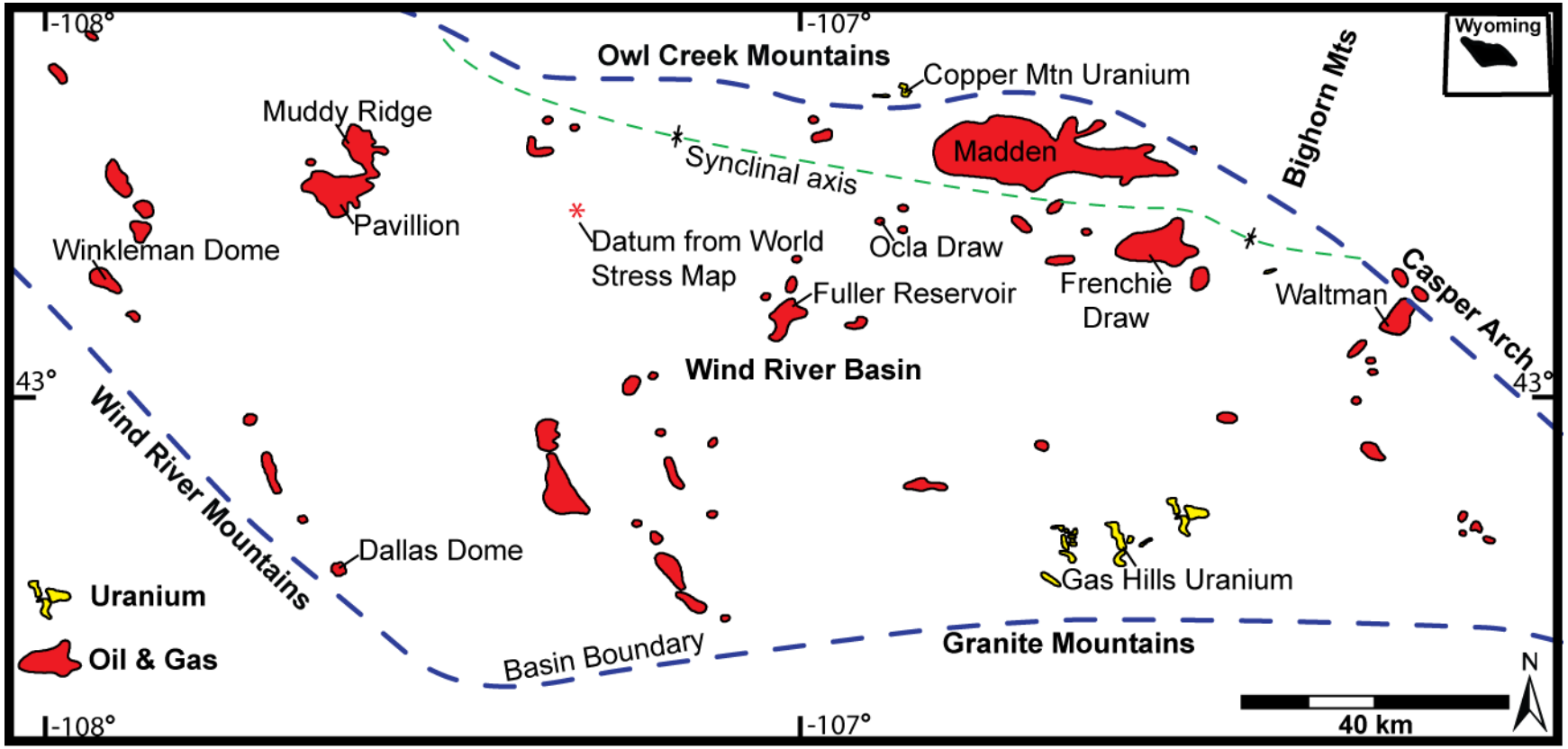

Figure 1.3 Wind River Basin energy resources after USBM (1990); basin boundary as shown parallels major basin-bounding faults.

In-situ recovery methods, which utilize reducing fluids, are not economically viable in highly-fractured areas (T. Wilton, 2009, personal communication). This is because fractures in the seal might allow contamination of groundwater aquifers and fractures in the reservoir would act to quickly channel fluids from injection to extraction sites, bypassing the majority of the uranium mineralization within the pore spaces of the matrix.

Hydrocarbons

Hydrocarbons have been known in the basin since natural oil springs at Dallas Dome provided lubricants for wagon axles headed west on the Oregon Trail. Wyoming's first oil well was drilled near these springs in 1883.

Understanding the structural context, stress axes, and natural fracturing present within a producing field is critical to predicting and modeling zones of higher intensity fracturing where increased fracture permeability may enhance production. Understanding the stress axes is also necessary for optimally orienting horizontal or slant wells and is also used in designing optimal fracture stimulations (Hennings et al., 2000). The timing of fracturing would also impact the migration and accumulation of hydrocarbons.

One end goal of this study is to better understand the production at Frenchie Draw gas field, operated by EnCana Oil & Gas (USA) Inc. It is the third largest gas field in the basin, located just south of the synclinal axis at the north-east corner of the basin, and it exhibits unusually high water production, approximating 1.5 Bbls of water per 1000 cubic feet of gas produced (Wyoming

Oil and Gas Conservation Commission, 2009). The discovery well was drilled in 1961 and has produced a near-constant million cubic feet per day of natural gas and it has reached only half of its expected ultimate recovery (D.P. DuBois, 2008, personal communication). The reservoir is located within the Lower Fort Union Formation in close association with a broad, northeasterly-trending and shallowly-plunging anticline (Normark, 1978; Mueller, 1989).

The field is considered an unconventional play due to its lack of significant structural or stratigraphic trapping and its steady, long-lived production. It is believed that the bulk of the production is coming from fractures, since the low permeability of the matrix is incapable of moving significant volumes of fluid (D.P. DuBois, 2009, personal communication). Another indication that the field is fractured is the unpredictable production. As of 2008, three out of four wells were marginally economic, with the top quartile supporting the economics of the play (D.P. DuBois, 2009, personal communication) and no solid correlation between production and any aspect of the geology identifiable in the borehole has been identified (C.E. Campbell, 2008, personal communication).

CHAPTER 2. GEOLOGIC FRAMEWORK

The Wind River Basin is a structural basin bounded by basement-involved, fault-bounded, asymmetric anticlinal arches that formed during the Laramide Orogeny (Bauer, 1934; Fanshawe, 1939; Wise, 1963; Keefer, 1970; Molzer & Erslev, 1995). A network of elliptical basins and anastomosing arches generally trends NNW-SSE across the Rocky Mountain foreland (Fig. 1.1), with notable exceptions including the east-west-trending northern and southern basin-bounding arches of the trapezoidal Wind River Basin, and the north-south-trending Colorado Front Range and Laramie Mountains (Erslev & Koenig, 2009). In cross section, the Wind River Basin is also asymmetrical, with the synclinal axis paralleling the northern margin between Madden and Frenchie Draw gas fields (Fig. 1.3).

On the western and eastern margins, the basin is bounded by the Wind River Mountains and Casper Arch that trend NNW-SSE. The Owl Creek Mountains and the Granite Mountains bound the northern and southern margins and trend east-west (Fig. 1.2). Following convention (Keefer, 1970), the Owl Creek Mountains herein includes the Bridger Mountains as part of the same basin-bounding arch. East of the Wind River Canyon it may be referred to as the eastern Owl Creek Mountains (Molzer & Erslev, 1995). Also for simplicity, the Big

Horn and Washakie Mountains, whose southern margins form the northeast and northwest corners of the basin, will also be included as part of the greater Owl Creek Mountains when discussing the northern margin.

Major high-angle normal faults bound these arches (Fig. 1.2) and include the Boysen and Cedar Ridge fault systems along the northern margin (Fanshawe, 1939), and the North Granite Mountains fault system along the southern margin (Bauer, 1934). Blind, low-angle thrust faults also bound the northern and eastern margins and are herein collectively referred to as the Owl Creek-Casper Arch Thrust. The Owl Creek Thrust includes the South Owl Creek and Shotgun Butte faults. These faults form a continuous thrust system from the southeastern to the northwestern corners of the basin (Gries, 1983).

Interior to the southern margin of the basin, there are at least five en-echelon, northwest-plunging anticlines (Fig. 1.2). From east to west these include: the Rattlesnake Hills, Dutton, Muskrat, Conant Creek, and Alkali Butte anticlines (Keefer, 1970). Along the western margin of the basin, a continuous series of back-limb tightening anticlines (Erslev, 2005) are arrayed from Winkleman Dome to Dallas Dome, northwest to southeast, respectively. These exposed anticlines, as well as other blind anticlines in the basin such as Pavillion, Waltman, Madden, and Frenchie Draw (Fig. 1.3) anticlines, are associated with the majority of the hydrocarbon reserves in the basin (Fox & Dolton, 1995). Generally, these anticlines are thick-skinned, basement-involved fault-propagation folds whose thrust faults are blind in most instances although some may also have thin-skinned thrust detachments.

Up until the onset of the Laramide Orogeny, the region was part of the stable foreland shelf just east of the Cordilleran fold and thrust belt and was covered by shallow seas that deposited a sequence of parallel units (Keefer, 1965). Beginning in the Maastrichtian, east-northeast directed Laramide horizontal compression (Erslev & Koenig, 2009), possibly driven by the tectonic collision and subduction of the Farallon oceanic plate under the North American cratonic plate (Brown, 1993), caused the break-up of the foreland into the present network of basins and anastamosing arches (Erslev, 2005). Previous workers in the Wind River Basin considered the Laramide to have lasted until the latest Paleocene or earliest Eocene (Bauer, 1934; Fanshawe, 1939; and Keefer, 1970). This was followed by down-dropping of the east-west-trending bounding arches by at least 760 meters, based on observed separation along the Boysen and North Granite Mountains faults, which possibly occurred in the late Miocene or early Pliocene (Bauer, 1934; Fanshawe, 1939; Keefer, 1970, and Scott, 2002). More recently, the area may have undergone epeirogenic uplift of 900-1500 meters during the Pliocene (Bauer, 1934; Keefer, 1970).

Previous Structural Research

The majority of the published structural field research has focused on the northern margin of the basin, probably due to the excellent outcrops exposed in the Wind River Canyon, which transects the Owl Creek Mountains from the south to the north. However, Keefer (1970) describes each of the major structures

surrounding the basin and Bauer (1934) primarily worked along the southern margin and in the Granite Mountains.

Detailed research into the structural geology of the basin and bounding arches was conducted in the early 1930's (Bauer, 1934; Jones, 1939; Fanshawe, 1939). These early papers were descriptive in nature, describing unit lithology and thickness, stratigraphic relationships, and type of faulting with amount of throw and relative timing based on cross-cutting relationships. Low-angle thrust faults were observed stratigraphically below the normal faults in the Wind River Canyon (Jones, 1939; Fanshawe, 1939) by these workers before being obscured by the reservoir created by the modern Boysen Dam, which was completed in 1952.

Wise (1963) proposed an upthrust model for the Owl Creeks (Fig. 2.1) based mainly on the observation of high-angle faults along the arch margin. In this model, as vertical uplift progresses, decompression results in thrusting and folding over the basin, shortly followed by extensional collapse of the fold and gravity sliding into the basin. Wise (1963) also noted even younger normal faults in the basin footwall, which down-dropped the arch with respect to the basin. During this same time, Keefer (1965; 1970) published descriptive works on the stratigraphy and structure of the basin as a whole.

During the late 1970's and 1980's, the vertical uplift and upthrust models (Stearns, 1978) came under scrutiny, partly due to the lack of a viable mechanism for vertical tectonics, but mainly due to observations from seismic

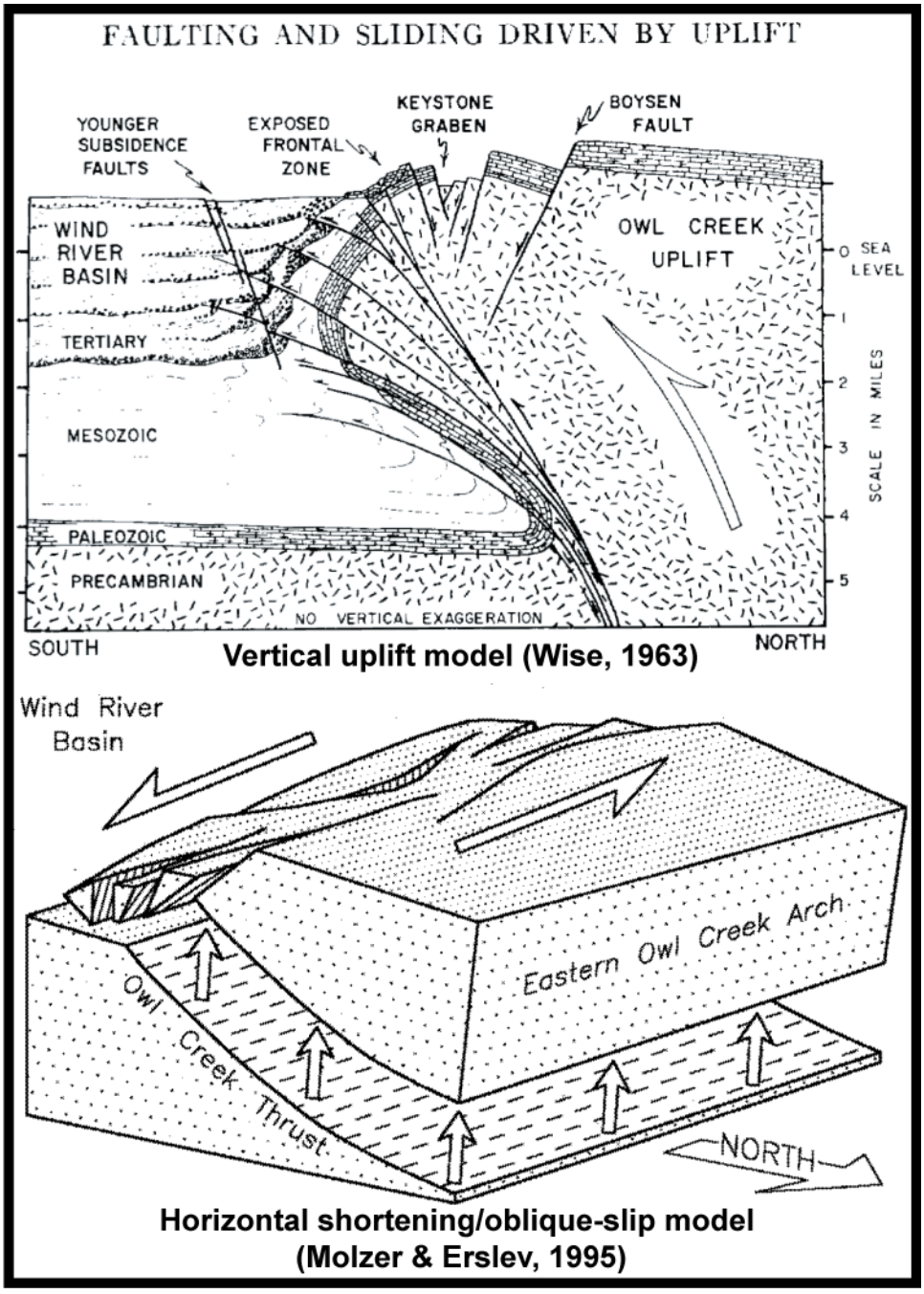

Figure 2.1 Comparison of vertical uplift & horizontal shortening models for the Owl Creek Mountains. Note the differences in the mechanisms explaining the normal faulting along the arch margin.

data of low-angle thrust faults underlying these basin- bounding arches and from drilling through the basement hanging walls (Gries, 1983).

To explain how the diverse trends of Laramide arches, such as those bounding the Wind River Basin, formed due to horizontal compression, Gries (1983) proposed a rotating horizontal compression direction where north-south-trending arches formed first and east-west-trending arches formed last during counter-clockwise rotation of the compression direction. In the Shirley Basin, on the southeastern corner of the Granite Mountains, Bergh & Snoke (1992) used field mapping and minor fault data to support a similar polyphase deformation. However, the onset of deformation for these diverse arch trends was shown to be synchronous based on stratigraphic observations (Brown, 1988; Dickinson et al., 1988). Based on stress tensor analysis (Angelier, 1984) of 27 minor faults from the Wind River Canyon, Varga (1993) concluded that the Owl Creek arch was emplaced perpendicular to the compression direction in a partitioned stress field.

Working in the eastern Owl Creek Mountains, Molzer and Erslev (1995) analyzed a larger dataset of 718 minor faults using eigenvector analysis and stress inversion (Angelier, 1990). They concluded that this east-west-trending arch was the result of a combination of left-slip and thrust faulting on the oblique-slip Owl Creek Thrust (Fig. 2.1). This was consistent with the conclusion drawn by Paylor & Yin (1993) who observed left-slip faulting in the western Owl Creek Mountains and proposed that the Owl Creeks were a bridge between the Wind River and Bighorn Mountain arches. The calculated stress axes by Molzer and Erslev are consistent with this oblique thrusting being caused by east-northeast directed horizontal compression. Later research by Erslev et al. (2004) and Erslev and Larson (2006) showed that minor faults also suggest that north-south

trending arches, such as the Colorado Front Range and Laramie Mountains, were also oblique to the mean ENE-WSW maximum compressive stress axis.

Since the beginning of structural research along the northern margin of the Wind River Basin, the majority of both thrust and normal faults on the arch margin were generally considered part of the same orogenic event. Molzer and Erslev (1995) interpreted the normal faults as resulting from the hangingwall tip undergoing synchronous left-slip and normal faulting, with the normal faulting possibly caused by collapse due to compaction in the underlying basin footwall. However, the east-west normal faults in the basin footwall were interpreted by Wise and Keefer as younger, possible subsidence faults with the consensus being that they down-dropped the arch with respect to the basin (Wise, 1963; Keefer, 1970). Keefer went so far as to suggest that one of these, the Cedar Ridge fault, followed the surface trace of the Owl Creek Thrust and that the normal faulting on the northern margin might be synchronous with the normal faulting on the southern margin, which also down-dropped the east-west Granite Mountains with respect to the basin along the North Granite Mountains fault (Bauer, 1934).

Seismic Observations

During an internship with EnCana Oil & Gas (USA) Inc., 2D and 3D seismic data from across the basin were structurally interpreted. This was done very conservatively, with faults only picked where obvious separation of the units occurred. Because this is a proprietary dataset, in some instances owned by

multiple interests, permission to display this data was not obtained. Instead, a schematic cross section, based on the seismic, well, and map data was generated (Fig. 2.2). This cross section is oriented north-south from the Owl Creek Mountains north of the Madden field, through Frenchie Draw gas field and Dutton Anticline, to the Granite Mountains.

This cross section shows the structural styles observed in the seismic data. First, basement-involved thrust faults are present in pre- to syn-orogenic units across the basin and include the Owl Creek-Casper Arch basin-bounding thrusts, thrusts below the Madden and Frenchie Draw gas fields, and thrusts under most of the southern anticlines. Second, and likely co-genetic with these thrusts, are thin-skinned thrusts such as the thin-skinned thrust at Dutton Anticline which becomes layer-parallel within the Cody Shale. Third, east-west-striking normal faults and down-dropped blocks are present near the surface in younger units. These normal faults were not observed farther than 20 km from the basin margins and did not propagate to great depth. Also, the folds above some of the thrust faults have flattened crests, such as at Frenchie Draw, and some appear to have reversed fold vergence, such as at Alkali Butte anticline, indicating post-thrusting normal movement and anticlinal collapse.

Stratigraphy

The Wind River Basin contains exceptional localities where the stratigraphy is well exposed. The Wind River Canyon, which transects the Owl

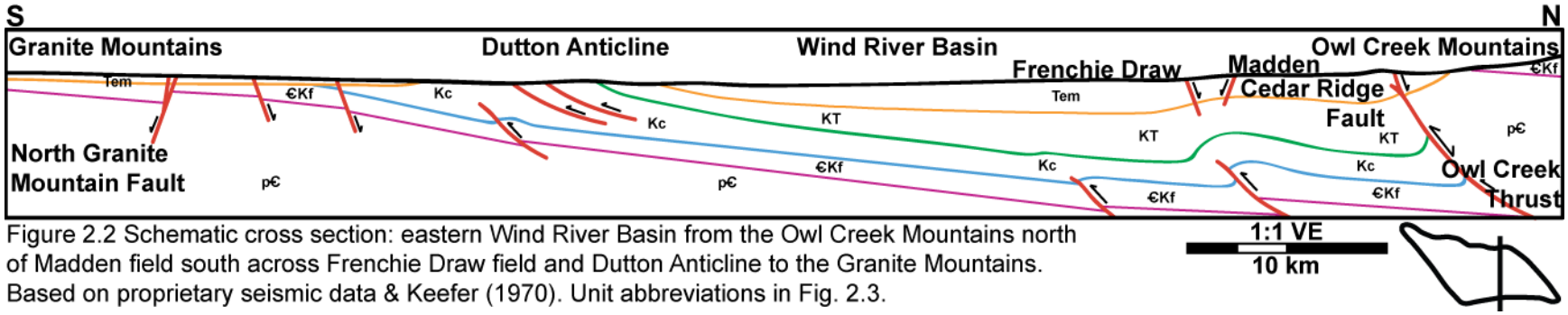

Figure 2.2 Schematic cross section: eastern Wind River Basin from the Owl Creek Mountains north of Madden field south across Frenchie Draw field and Dutton Anticline to the Granite Mountains. Based on proprietary seismic data & Keefer (1970). Unit abbreviations in Fig. 2.3.

Creek Mountains from south to north and attains a depth of 760 meters, exposes rocks from Precambrian basement to Upper Cretaceous Mowry Shale for a distance of 25 km. The Eocene Wind River Formation is also found onlapping the arch, in angular unconformity with the older units (Appendix B.11). Hell's Half Acre, a common sightseeing stop and eroded area on the eastern margin of the basin above the blind Casper Arch Thrust, beautifully exposes the steeply-dipping Mesa Verde through Fort Union formations. The shallow-dipping lower member of the Wind River Formation, the Lysite Member, is exposed here above the angular unconformity between Eocene and Paleocene units. Conant Creek and Dutton anticlines along the southern margin of the basin have excellent exposures of Cambrian through Paleocene units. Here the Lance Formation hosts numerous petroglyphs at Castle Gardens.

The stratigraphic sequence in the Wind River Basin has been well described in detail by Bauer (1934), who described mainly the Upper Cretaceous and younger sediments, and Keefer (1965), who provided cross sections, isopach maps, and paleogeographic reconstructions for each formation. Thaden (1978, 1980a-c) provided detailed lithologic descriptions of each unit in conjunction with mapping done in the eastern Owl Creek Mountains and the adjacent basin. Jones (1939) and Fanshawe (1939) focused on the Wind River Canyon and northern margin, with Fanshawe grouping the formations into incompetent and competent units.

Figure 2.3 shows the stratigraphic column used in this study, with thicknesses from Bauer (1934), which were measured along the southern

margin, and formation names from Gower (1978). An approach similar to that of Fanshawe's competency units is used to generalize and group the stratigraphic units for this study and simplify the geologic base map, insets, and cross section.

Precambrian (**ᴘЄ**)

The Precambrian basement is composed of three generalized rock types. The oldest units are Archean supracrustal gneisses composed of metasediments and metavolcanics. Archean granites intruded these during later magmatism (Chamberlain et al., 2003). A few unmetamorphosed mafic dikes at Copper Mountain (Hausel et al., 1985) and those in the Granite Mountains have a mean trend of N40°E and cut the two older units. Precambrian foliations in the eastern Owl Creek Mountains have a mean trend of N76°E (Molzer, 1993).

Cambrian to Frontier (**ЄK$_f$**)

The Paleozoic, Triassic, Jurassic, and Lower Cretaceous formations are predominantly composed of competent, well-cemented limestones, dolostones, and sandstones with interbedded shales. Most slickensides were found in the quartzitic Flathead Sandstone, which lies directly on the non-conformity with the basement. To a much lesser extent, slickensides were also found in sandstones in the Gros Ventre Formation, which grades downward into the Flathead Sandstone, the sandstones of the Tensleep Formation, Chugwater Formation

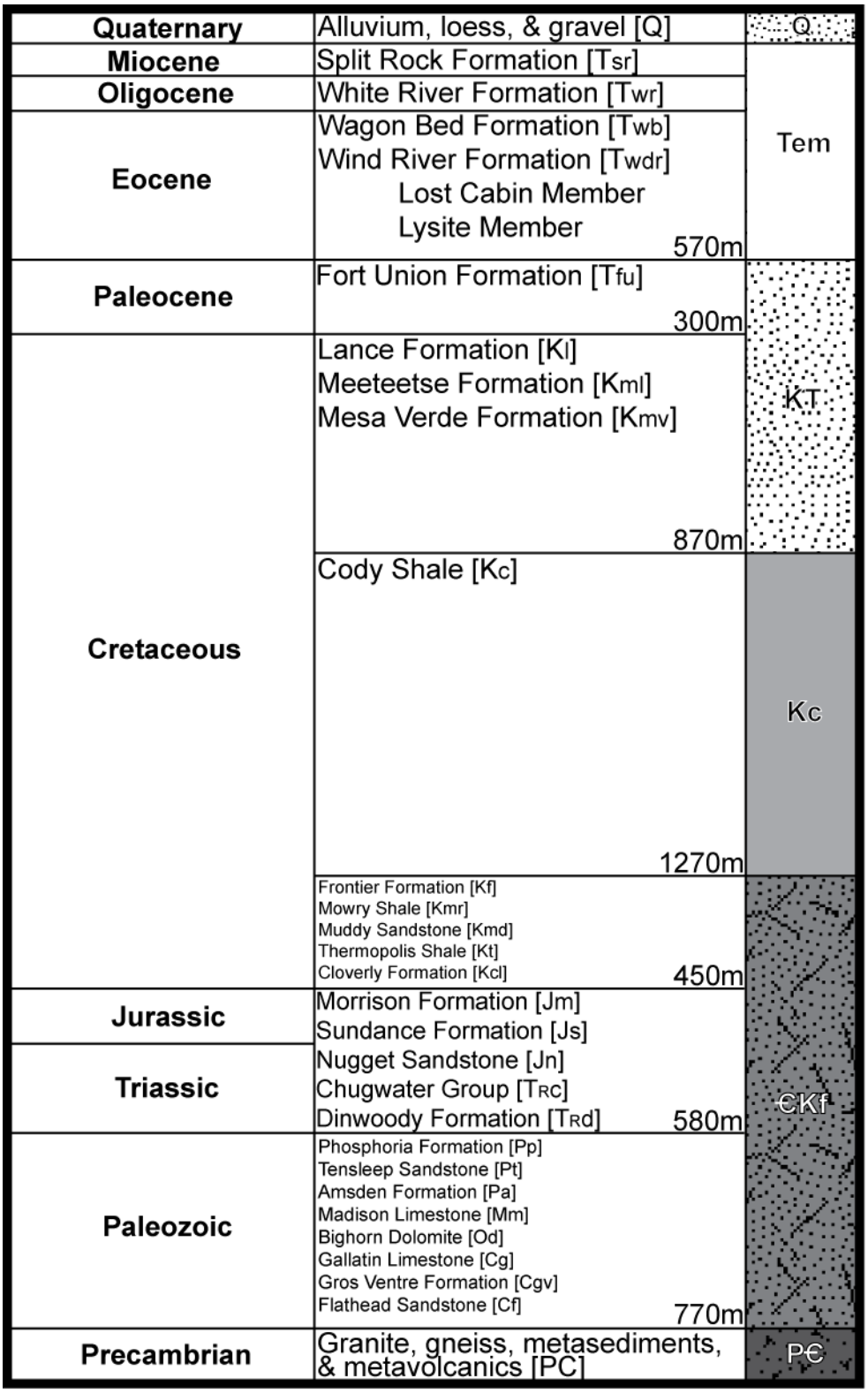

Figure 2.3 Stratigraphic column scaled to thicknesses from Bauer (1934) measured along southern margin of the basin. Syn-orogenic "KT" units thicken significantly toward the northeastern margin.

redbeds and Alcova Limestone Member, and also a few in the Cloverly Formation conglomerates.

The Cambrian section is comprised of the Flathead Sandstone, which is dark orange to brown and generally crossbedded, the greenish and maroon sandy shales of the Gros Ventre Formation, and the Gallatin Limestone, which is orange or olive and contains beds of flat pebble conglomerate.

The Ordovician and Mississippian section is comprised of the Bighorn Dolomite and Madison Limestone, both of which are yellowish-gray and thickly bedded. They can be distinguished based on their calcium carbonate content. The dolomites tend to form sharp ridges and pits due to weathering whereas the limestones tend to form calcite filled vugs.

The Pennsylvanian Amsden and Tensleep Formations are white to yellow-brown and crossbedded. The main difference between the two formations is the very thickly bedded nature of the Tensleep and its lack of thin, interbedded shales.

The Permian section is the Phosphoria Formation, a phosphatic limestone and mudstone. The Triassic is composed of the Dinwoody Formation and the Chugwater Group. The Dinwoody Formation is yellowish-white, silty sandstone. The Chugwater Group contains the Red Peak Member, a red, thin-bedded siltstone commonly with ripples; the Alcova Limestone Member, a gray, thinly-bedded limestone with algal mound structures; and the Crow Mountain Sandstone Member, whose red and thickly bedded sandstones sometimes have whitish halos around the fractures indicating fluid movement.

The Jurassic-Triassic boundary is spanned by the Nugget Sandstone (Gower, 1978) which is a white sandstone containing frosted grains. The Jurassic contains the Sundance Formation, which is an olive to yellow-brown limestone and siltstone with some sandstone, flaggy bedding, and an abundance of Belemnite fossils with some bivalves; and the Morrison Formation, which is composed of yellow to green, poorly cemented mudstone and sandstone.

The lower Cretaceous units include the Cloverly Formation, a greenish pebble conglomerate to whitish coarse sand; the Thermopolis Shale, a dark gray claystone; the light brown Muddy Sandstone; the Mowry Shale, a yellowish to white claystone; and the Frontier Formation, which is composed of brownish sandstone with interbedded gray mudstone and coal.

Cody Shale (κ_c)

The Cody Shale, a lower Cretaceous marine shale deposited in the Western Interior Seaway (Steidtmann, 1993), is a major incompetent unit and is as much as 71% as thick as the entire preceding Phanerozoic section as measured by Bauer (1934) along the southern margin of the basin. It is gray to buff colored, mainly silt and clay with some sands in the upper section, and is thinly laminated and fissile. Based on these unique characteristics, the Cody has been not been combined with any other group. The Flathead Sandstone through the Cody Shale formations are all deposited roughly parallel to each other, indicating a lack of syn-orogenic deposition during this time, and are considered pre-Laramide. The Cody Shale may act as a regional detachment zone.

Cretaceous-Tertiary (**KT**)

Above the Cody Shale, observations from seismic data show that a syn-orogenic sedimentary wedge began to form in response to the encroaching Sevier and later Laramide orogenies. Formations included in this group include the Upper Cretaceous Mesa Verde though Paleocene Fort Union formations. Each of the formations in this group consists of thin coals and interfingering mudstones and poorly-to-moderately-sorted sandstones. The mudstones are gray to black and clay rich. The sandstones of the Mesa Verde and Meeteetse formations are orange and those of Lance and Fort Union formations are whitish with thin brown, hardened veneers on the upper surface of many Lance Formation sandstones (Appendix B.10). These units are marginal marine to fluvial and soft-sediment deformation is common (Thompson, 2006). In the subsurface, the Waltman Shale, the middle member of the Fort Union Formation, attests to a major event when a majority of the basin was occupied by a lake.

Along the northern and eastern margins of the basin, these units are steeply dipping. In the sandstones, iron-rich fluids, possibly responsible for the hardened veneers, preserved slickensides and the open fractures have dark brown halos from fluid movement through the fractures.

Eocene to Miocene (**T_{em}**)

The Eocene through Miocene units are similarly composed of a variable sequence of mudstones and poorly sorted sandstone lenses but are grouped separately from the KT units because of their lack of significant tilting. The first of

these units, the mid-Eocene Wind River Formation, is composed of the lower Lysite Member, which is a variegated sequence of light maroon and gray mudstones and yellowish-white sandstones, and the upper Lost Cabin Member, which is similar but contains thicker, more frequent, and darker sandstone lenses. The Late Eocene Wagon Bed Formation is composed of greenish-white tuffaceous claystone and siltstone. Fractures in these units are found in sandstones and joints were typically open and free of mineralization whereas minor faults tended to manifest as cataclasite bands rather than as slickensides.

The Oligocene and Miocene White River and Split Rock formations are included in the stratigraphic column (Fig. 2.3) for reference because digitized faults along the southern margin of the basin cut these units. These units are not exposed within the basin and are only found in the Granite Mountains surrounding remnant knobs of the Precambrian core. Preservation of these young units on top of the collapsed arch aids in bracketing the timing of this collapse. These units are also composed of a variable sequence of mudstones and poorly-sorted sandstone lenses.

Quaternary (**Q**)

Quaternary alluvium is also shown (Fig. 1.2) because the modern drainages tend to parallel faults observed from seismic data (P.J. Wynne, 2008, personal communication). These generally east-west-trending linear drainage features give clues to the modern stress state as some of the major faults in the area have had Quaternary movement (Machette, 1999) and some activity

continues to the present. The large non-linear patches in the middle of the basin, however, are modern dune and loess sand deposits and do not necessarily correlate with deformation.

Study Areas

Three major field areas were studied and are placed in their geologic context below. Excepted from this is a description of the geologic context for the subsurface fracture data from micro-resistivity data at Frenchie Draw, which is described in the significance section, and the two isolated outcrop stations in the western half of the basin. The station near Winkleman Dome (station WD1) is located along trend with a series of back-limb tightening folds while the other, along Muddy Creek (station MC1), is well into the basin and removed from major structures exposed at the surface.

Hell's Half Acre

Hell's Half Acre was selected as a study area because of its repeated occurrence in the literature, its ease of access and frequency as a stop on field trips, and its excellent outcrops. Two other stations near the Waltman and Cave Gulch gas fields are included along with the stations at Hell's Half Acre. Steeply dipping units of the Upper Cretaceous and Paleocene are tucked into the gently rolling hills. In sharp contrast, the shallow-dipping units of the Eocene outcrop above an exceptionally visible angular unconformity. Its location on the hanging wall of the Casper Arch Thrust makes it a good place to study development of

the arch and compare and contrast fracturing in the Paleocene and older units with fracturing in the Eocene units.

Southern Margin

Along the southern margin of the basin are a series of five northwest-plunging, en-echelon anticlines. These anticlines contain outcrops of the majority of the geologic column and make for an ideal area to document the difference between Laramide fold-related jointing and later joints. These anticlines tend to terminate along the major North Granite Mountains normal fault system. This east-west-striking fault down-dropped the arch with respect to the basin and a zone of associated east-west-striking faults extends about 20 km into the basin to Muskrat anticline.

Due to the onset of harsh weather at the end of my field season, only a few stations were collected and these were mainly from younger units. In addition to the outcrops in the anticlines, other possible locations for future fracture data collection would be the large Uranium strip mines in the area.

Northern Margin

The primary area of focus for this study was the northern margin of the basin, which included the Wind River Canyon. The canyon and outcrops along the Boysen Reservoir were used to obtain a fracture transect across the southern flank of the Owl Creek Arch and out into the basin—from the core of the anticline on the hanging wall of the Owl Creek Thrust to the basin footwall. Numerous

normal faults, located on the southern flank of the Owl Creek Arch at the entrance to the canyon, add complexity to this area.

A 20 km zone between the northern margin of the basin and Badwater Creek contained outcrops and fractures. Here, as with Hell's Half Acre, the Eocene units are in angular unconformity with the older units, giving a record of the uplift of the arch and the subsidence and filling of the basin. Located along the northern margin are several inliers of steeply-dipping units isolated by the discontinuous Eocene cover. These inliers provided good outcrops for collecting fracture data. Also in this 20 km zone there are numerous, more recent normal faults and modern drainages, which expose the lenticular, fractured sandstones of the Wind River Formation. Farther into the basin, outcrops with units lithified well enough to contain fractures were rare to non-existent.

Due to the low-angle nature of the Owl Creek thrust fault, the surface trace of this blind fault is highly irregular, deflecting around such structures as Copper Mountain, where the faults surface trace is further into the basin, and the embayment in which the Madden gas field is located. This additional complexity aided in testing the hypothesis that later fracturing in the basin footwall is highly localized and parallel to the pre-existing thrust.

CHAPTER 3. DATA COLLECTION

Fracture data was collected into three datasets that included 1447 fracture strike segments digitized from geologic maps, 9107 subsurface fractures previously interpreted by log analysts from micro-resistivity image logs, and 1833 outcrop fractures measured specifically for this study. Other fracture data came from one well in the World Stress Map (Heidbach et al., 2008) database with borehole breakout data and a May 17th, 2009 normal fault earthquake's previously calculated fault plane solution (Hermann, 2009).

Mapped Fractures

Digitized fracture data aided in bridging the gap between the minor fracture data from outcrop and well logs, and the larger-scale structures in the basin. This data was obtained by digitizing fault strike traces from geologic maps (Fig. 3.1).

The faults were digitized as line end-points on a digitizing tablet using CALINE (Erslev, 1995) and converted to 10° smoothed rose diagrams using LDIS (Erslev, 1998a) which also calculated the 2θ vector mean. The 2θ vector

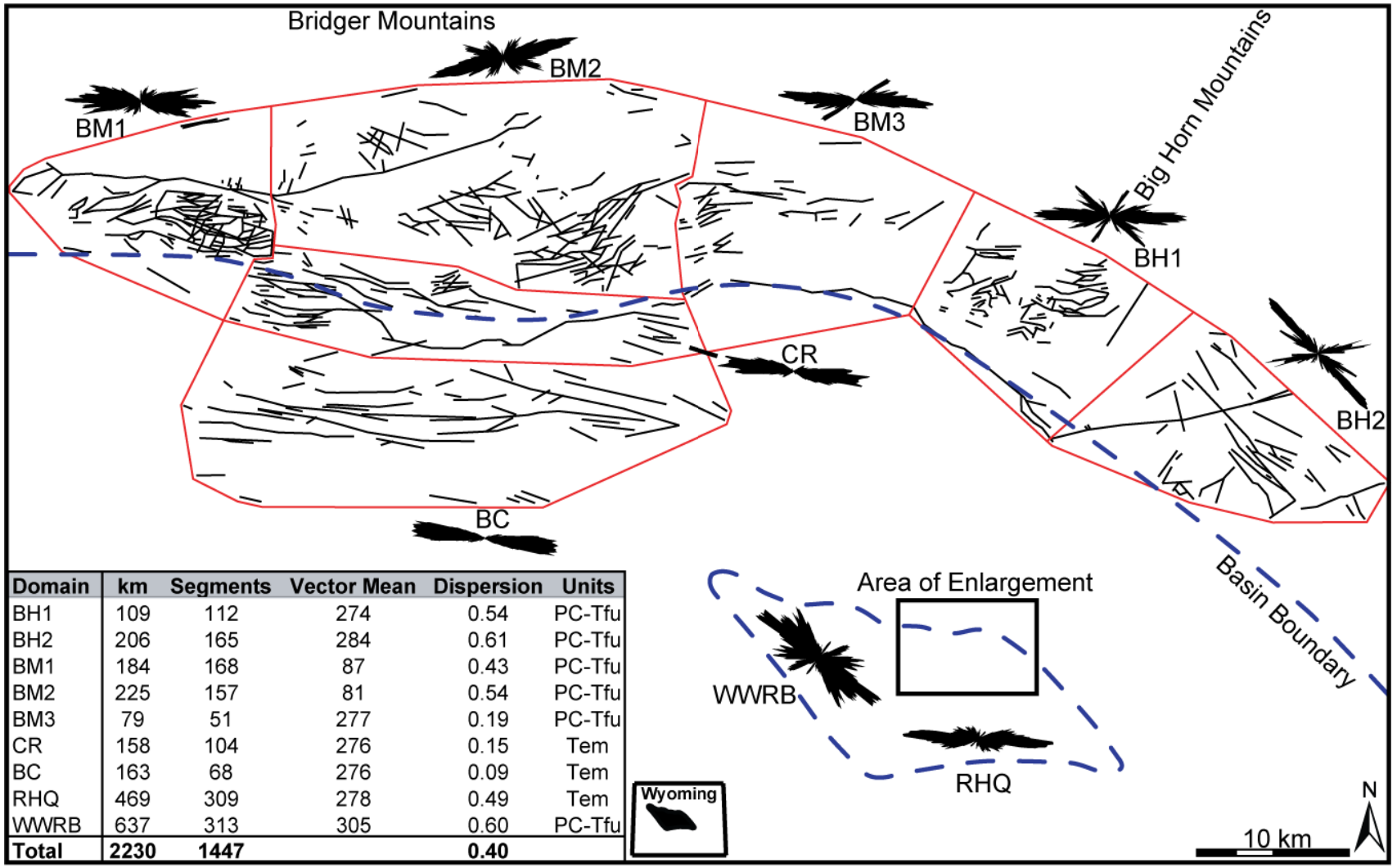

Domain	km	Segments	Vector Mean	Dispersion	Units
BH1	109	112	274	0.54	PC-Tfu
BH2	206	165	284	0.61	PC-Tfu
BM1	184	168	87	0.43	PC-Tfu
BM2	225	157	81	0.54	PC-Tfu
BM3	79	51	277	0.19	PC-Tfu
CR	158	104	276	0.15	Tem
BC	163	68	276	0.09	Tem
RHQ	469	309	278	0.49	Tem
WWRB	637	313	305	0.60	PC-Tfu
Total	**2230**	**1447**		**0.40**	

Figure 3.1 Digitized domains & data, unit abbreviations: PC: Precambrian; Tfu: Fort Union Fm; Tem: Eocene-Miocene.

mean is a simple calculation for averaging azimuthal data that is 180° apart (Krumbein, 1939) to get the mean strike. Also calculated was the dispersion, where values closer to zero equate to more highly-clustered data.

Longer faults, whose strikes varied, were broken down into smaller straight-line segments. The mapped faults from the Thermopolis (Love et al., 1979) and Arminto (Love et al., 1978) 1° x 2° quadrangles were sub-divided into domains based on natural breaks in the fault density and relationships to the basin margin (Fig. 3.1). The other two domains include all faults from the basin west of Boysen Reservoir (Keefer, 1970) and all faults along the southern margin of the basin from the Rattlesnake Hills 30’ x 60’ quadrangle (Hausel & Sutherland, 2003).

Dip and slip sense data was not available for the majority of these faults and so it was not used. The timing of faulting was only resolvable by the youngest strata cut. For each domain, a significant majority of the faults fall into one of two age categories: those that cut Eocene and younger strata and those that did not. The basin margin, which parallels the major Cedar Ridge normal fault on the north, is a good dividing line between these domains. Exceptions are the few faults that cut Eocene strata in the Owl Creek Mountains or the few associated with the anticlines on the southern margin. Faults in this dataset cut Precambrian to Miocene units and most were mapped as normal faults.

From the data, there does not appear to be a strong temporal variation in the strike of the faults, rather the variation appears to be spatial and parallels the

basin margins with two dominant modes that strike northwest-southeast and east-west.

Subsurface Fractures

Subsurface fracture data previously interpreted by log analysts from micro-resistivity image well logs provided mid-basin data where outcrops are poor or absent. Drilling-induced fractures also allow for analysis of the modern stress axes. This fracture data was previously interpreted by industry log analysts and came mainly from Schlumberger's Formation Micro-Imager but a few came from Halliburton's Electrical Micro-Imaging tools. These logging tools give a very detailed, three-dimensional, image-like log of the borehole's shallow electrical conductivity/resistivity. The dataset was compiled and analyzed during a 12 week internship with EnCana Oil & Gas (USA) from mid-May to the beginning of August, 2008. This dataset includes 23 well logs, 20 of which are from Frenchie Draw and 22 of which typically logged the upper part of the lower, unnamed member of the Fort Union Formation (Table A.5) and sometimes part of the Waltman Shale Member above this. Because this is proprietary data, the exact wells and their locations are not given.

Fracture Categories

Bed boundaries, cross sets, and fractures appear as discontinuities in the conductivity/resistivity of the borehole wall. Multiple fracture categories were previously interpreted by Schlumberger and Halliburton log analysts and consist

of conductive, resistive, drilling-induced, and faults. Conductive fractures were interpreted as open fractures (potassium-chloride and salt-based drilling mud would enhance the conductivity of these fractures making them more resolvable) whereas resistive fractures were interpreted, based on the presence of highly resistive cement, as healed or partially healed, depending on the degree of mineralization (gas bubbles and oil-based drilling mud may also cause a high resistivity response). Schlumberger analysts went further to interpret different categories of open fractures, including those in coal, and continuous fractures, which were defined as large fractures transecting the borehole. Schlumberger analysts also interpreted lithologically-bound fractures, which terminate at bed boundaries. These fractures may be either natural or induced as induced fractures can be lithologically bound. Some lithologically bound fractures were re-interpreted as drilling-induced, however, most are probably natural. Visual inspection of the 70 previously identified faults from the Frenchie Draw dataset revealed that a little over half have no obvious bedding separation. No conclusive method for determining the sense of separation was found for those that had minor offsets.

Drilling-induced fractures form as a result of differential stress during drilling, weight on bit, and interaction between the mud column and the formation adjacent to the borehole wall. They trend perpendicular to the modern minimum compressive stress and parallel to the maximum compressive stress. Borehole breakouts, which form perpendicular to the induced fractures, were also used to

get the modern minimum compressive stress in a couple wells where induced fracture data was not available.

Combining all the fracture categories except drilling-induced fractures and borehole breakouts gave the non-induced category. This category of predominantly natural fractures may contain a few misidentified induced fractures, especially in the lithologically-bound category.

Because the subsurface fractures are predominantly bedding-perpendicular and have a mean trend of northwest-southeast with very little variation, they are grouped into only two categories, natural and induced. This will be further discussed in chapter 4. The east-west-striking fractures observed in the digitized data are not observed in the subsurface fractures because the wells were not located in the same area.

Outcrop Fractures

Field research was conducted from the beginning of August through the first week of October 2008. There were also shorter reconnaissance and follow-up trips to the area, with a total of 10 weeks spent in the field. 1833 fracture measurements were taken at 42 stations in earliest Cambrian to late Eocene units from across the entire basin (Table A.1, Figs. 3.2-3.6). Outcrop fractures, although less in number, form the bulk of this study's fracture analyses as they had the full suite of information including fracture type and sense of movement.

Fracture Measurement

The goal at each station where fractures were measured was to collect at least 20 fracture measurements that included the full suite of data. For minor faults this included bedding strike-dip, fracture strike-dip, slip sense, and lineation trend-plunge. For joints, only the bedding strike-dip and fracture strike-dip could be measured. Strike-dip of fracture planes and trend-plunge of lineations were measured in the field by direct contact methods (Marshak & Mitra, 1988; Barnes & Lisle, 2004) whenever possible. Direct contact methods provided the greatest accuracy for these measurements and involved placing my field book on the bedding or fracture plane to measure strike-dip or placing it in the vertical plane along the lineation to measure trend-plunge. In the case of shallow planes dipping less than 16° where strike measurements were less reliable, dip direction was measured, and for lineations on high-angle planes dipping greater than 74°, the pitch was measured as more reliable than trend-plunge. Both dip and pitch were measured clockwise of strike.

Fracture Type Identification

For clarity, fractures are defined as planar discontinuities in the rock. Two types of fractures were measured—joints (n=822) and minor faults (n=1011). Joints are opening mode fractures, across which there has been no observable fracture-parallel slip (Van der Pluijm & Marshak, 2004). Plumose or strain shadow effects were only observed at station WRC9, so joints were usually identified based on their bedding-perpendicular nature and the lack of any lineations, conjugate sets, or observable slip. Minor faults are fractures across

which there has been fracture-parallel slip observed in the form of slickensides, cataclasite bands, or bedding separation. Lineations, Riedel fractures, and conjugate sets were common features of the minor faults.

Joints measured included systematic joints (J_s=617), which in this study had a mean 89° dip in relation to the bedding plane, and non-systematic joints (J_{ns}=205). In this study, systematic joints are defined as dominant, continuous, generally evenly spaced and planar joints. The non-systematic joints are more discontinuous, not necessarily planar, and not parallel to the systematic joints (Van der Pluijm and Marshak, 2004).

Two domains trending northwest-southeast and east-west were observed in the systematic joints just as in the digitized data. Non-systematic joints typically abutted systematic joints and formed a secondary set of joints. Non-systematic joints are more variable in strike-dip and are sub-orthogonal to the systematic joints.

The majority of joints were open; however, the east-west trending systematic joints at stations DA2, WRC8, and SH2 had patchy mineralization and about half those at BC3 were fully mineralized and resistant to erosion. Halos from fluid flow through the fractures were present around systematic joints along the Casper Arch and Owl Creek Mountains.

Minor faults included slickensides, some of which have been shown to be micro-cataclasite veneers (Molzer, 1993) in a similar study in the eastern Owl Creek Mountains, and cataclasite bands, which were usually slickensided when split open. Stations where cataclasite bands dominated the data included BR2

(Appendix B.1), SM1, DA1, MA3, and W2. In addition, normal faults were identified at BR3 and BC1 & 2, where conjugate fractures had a vertical acute bisector (Appendix B.2) and no indication of opening mode fracturing; and at WRC7, where normal separation was observed.

Lineations measured included slickenlines at most stations, calcite growth fibers at SM1, clayey slicks at BC2, and linear undulations at HHA4 & 7 and MA1. Slickenlines were predominantly found in pre-Laramide, well-cemented sandstones, with the exceptions being limestones of the Gallatin Formation at WRC8 and the Alcova Limestone Member at CCA1. Slickenlines were also found in syn-Laramide sandstones at HHA2 and W1, where hardening from iron-rich fluids may have occurred. Linear undulations in the form of ridges and grooves (Means, 1987) were found in poorly cemented, younger sandstones at HHA 4 & 7 and MA1 and were interpreted as slip-parallel.

Fault slip sense determinations were made in the field utilizing the surface morphologies described by Petit (1987). Most minor faults were of the RM type surfaces, which were composed of the slickensided and often striated main slip surface (M) and Riedel (R) fractures that form at low-angles to the M surface (Appendix B.3). The small wedge of rock formed where these planes intersect usually broke off at the tip, giving a stepped appearance to the main surface. Slip sense was then determined as being against these steps. This method was used to determine slip sense and has been supported with petrographic evidence (Molzer, 1993) in a similar study in the eastern Owl Creek Mountains. The slip sense, thus determined, always agreed with the conjugate geometries observed,

where the maximum compressive stress was parallel to the acute bisector. Other methods of determining slip sense, which were used when this method was unavailable, were conjugate geometries and observed separation of the units. At one location, SM1, slip sense was determined from calcite fibers growing from the lee side of asperities on the fault surface. Faults were identified as right-slip, left-slip, thrust, or normal and are more fully described in chapter 4.

Correction of Lineation Measurements

Lineations, as measured in the field, commonly plot just off of the plane of the fault due to slight errors in field measurements. This was easily corrected by calculating plunge from trend, which was the more accurate measurement on low-angle planes, and trend from plunge, which was the more accurate measurement on high-angle planes. Trend and plunge may also be calculated from pitch and vice-versa. The mean correction made was 1° for the 476 lineations. This corrected outcrop fracture data is presented by station on stereonets (Figs. 3.2-3.6).

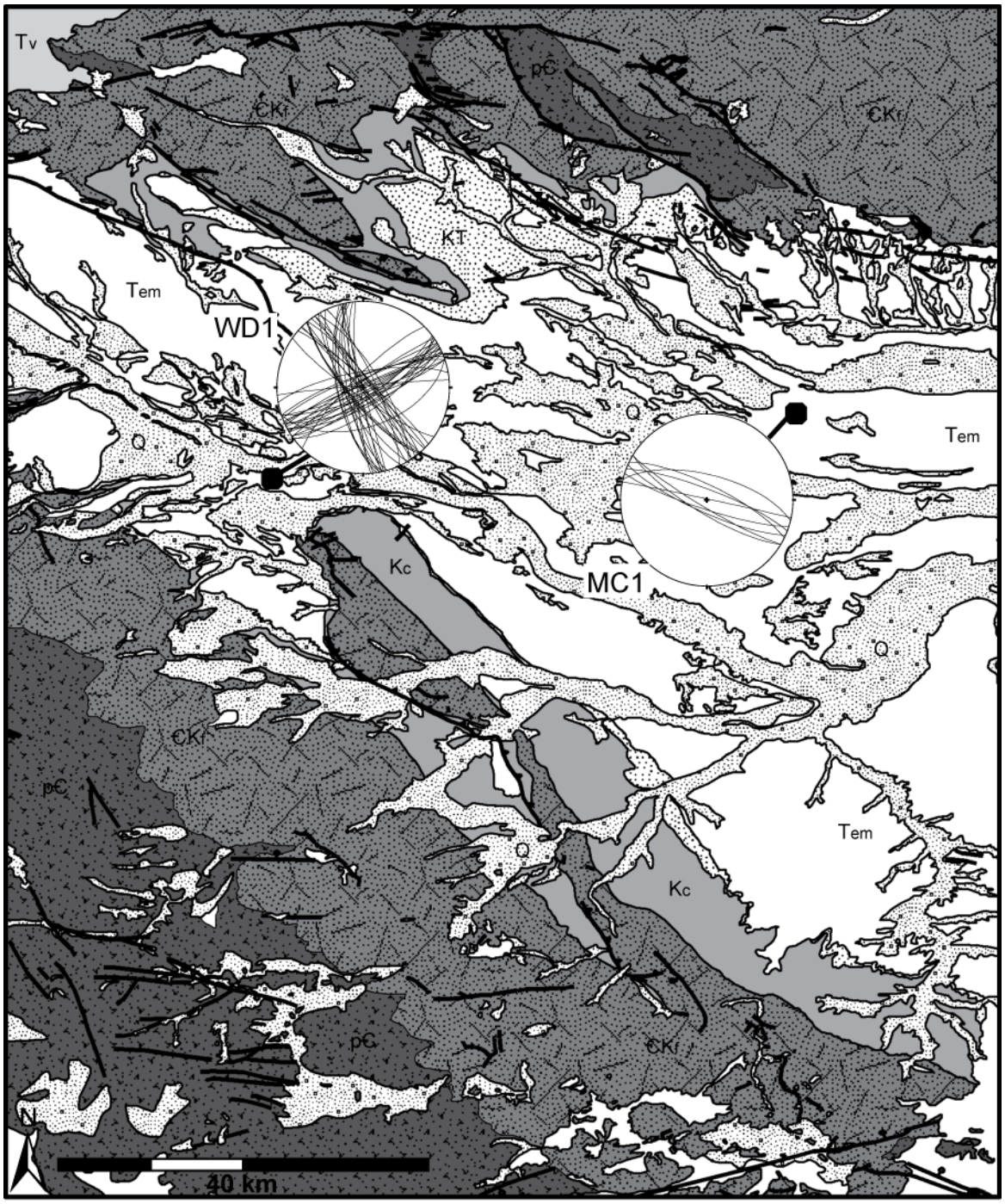

Figure 3.2 Stereonets of outcrop systematic joints (arcs): western Wind River Basin, see inset 1, Fig. 1.2 for location & unit abbreviations.

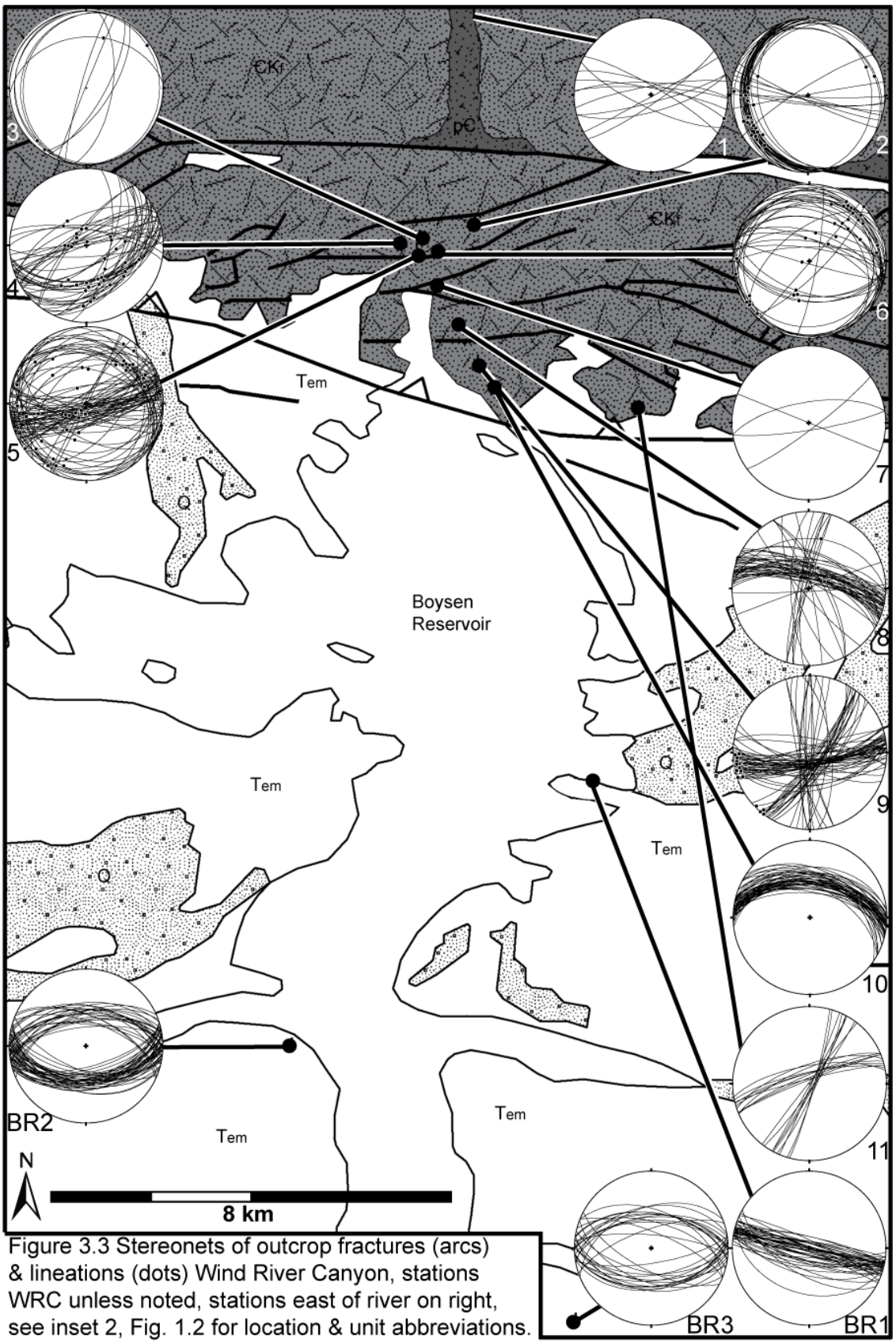

Figure 3.3 Stereonets of outcrop fractures (arcs) & lineations (dots) Wind River Canyon, stations WRC unless noted, stations east of river on right, see inset 2, Fig. 1.2 for location & unit abbreviations.

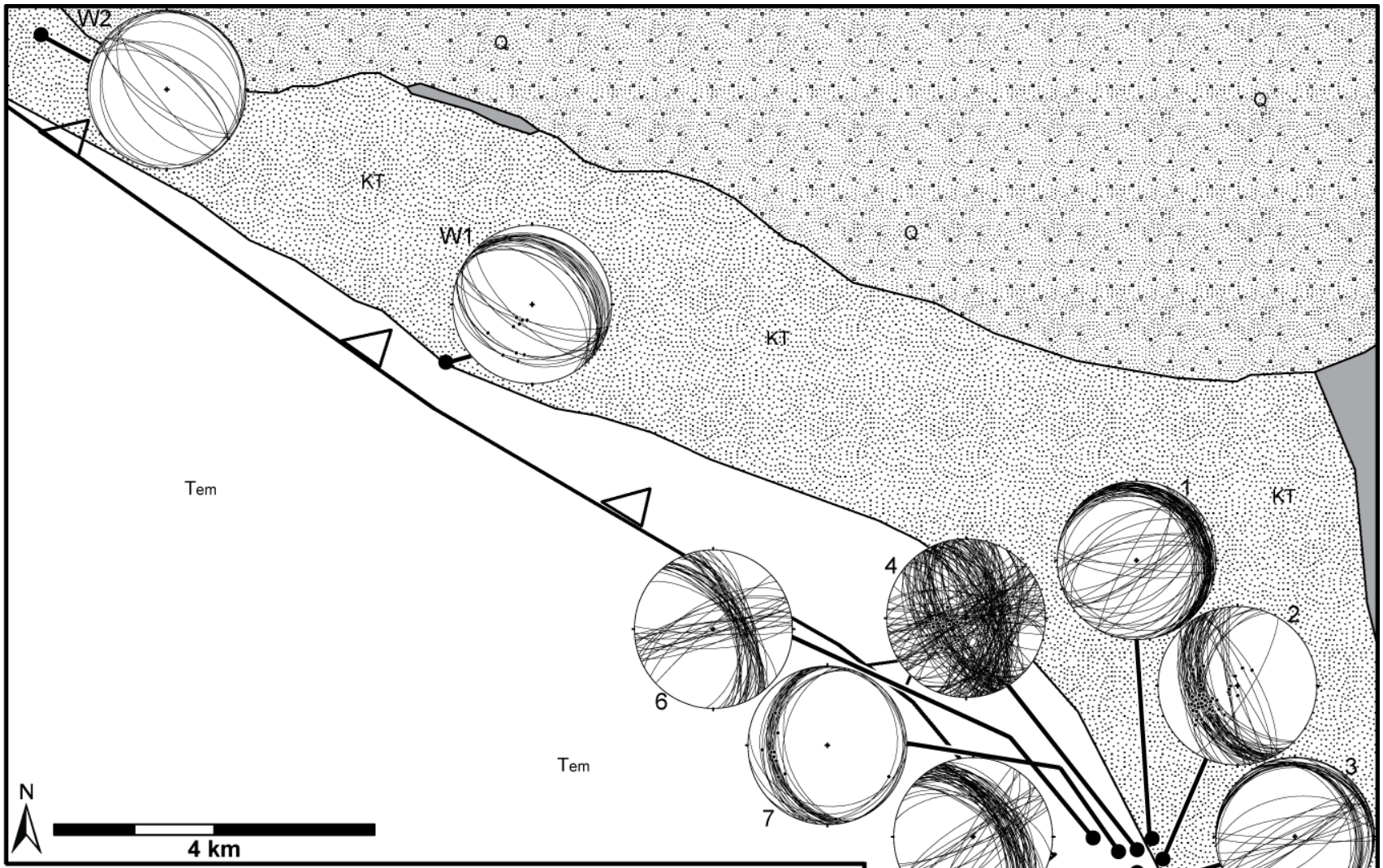

Figure 3.4 Stereonets of outcrop fractures (arcs) & lineations (dots): Casper Arch, stations HHA unless noted, see inset 3, Fig. 1.2 for location & unit abbreviations.

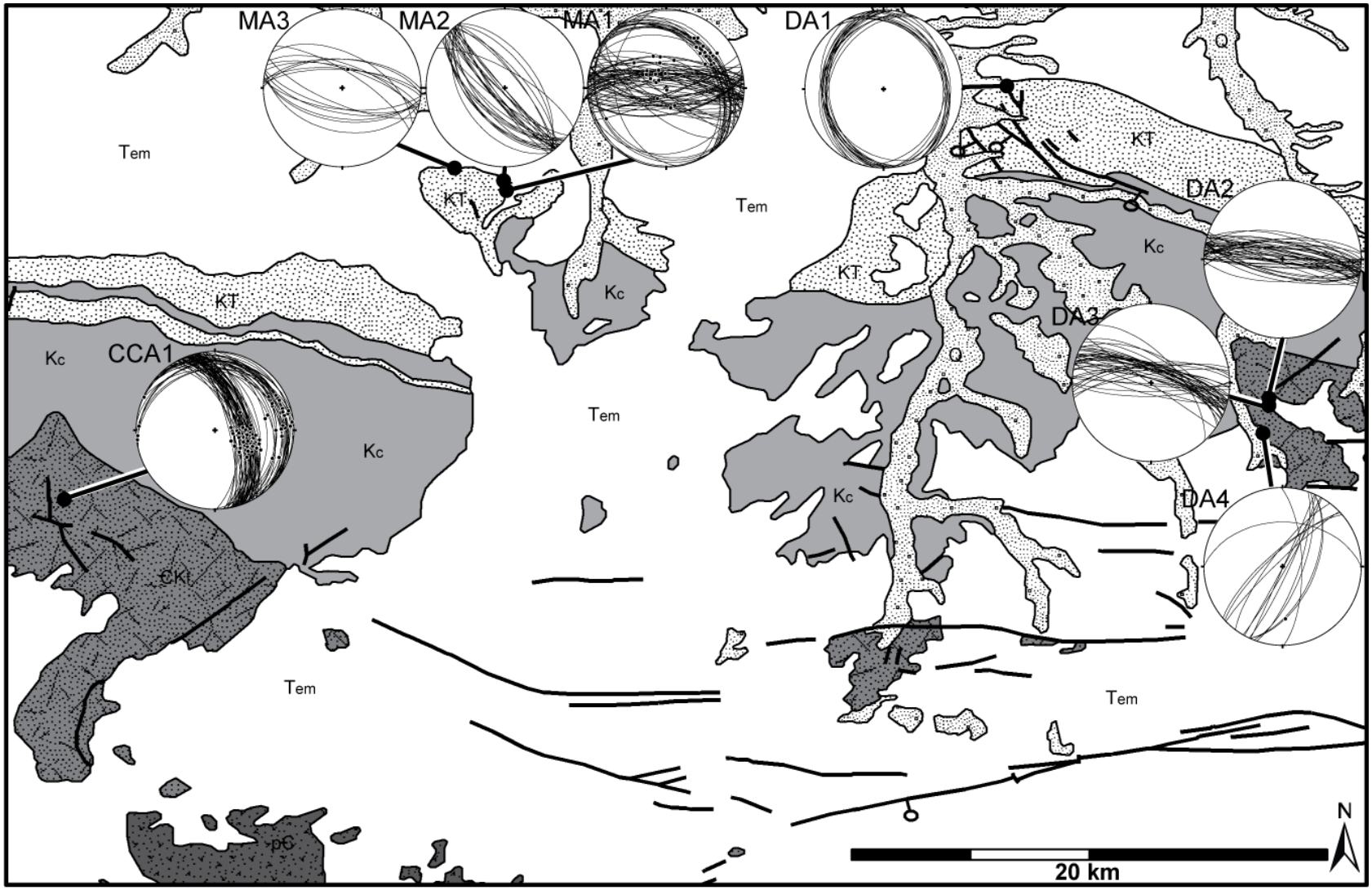

Figure 3.5 Stereonets of outcrop fractures (arcs) & lineations (dots): southern margin anticlines, see inset 4, Fig 1.2. for location & unit abbreviations.

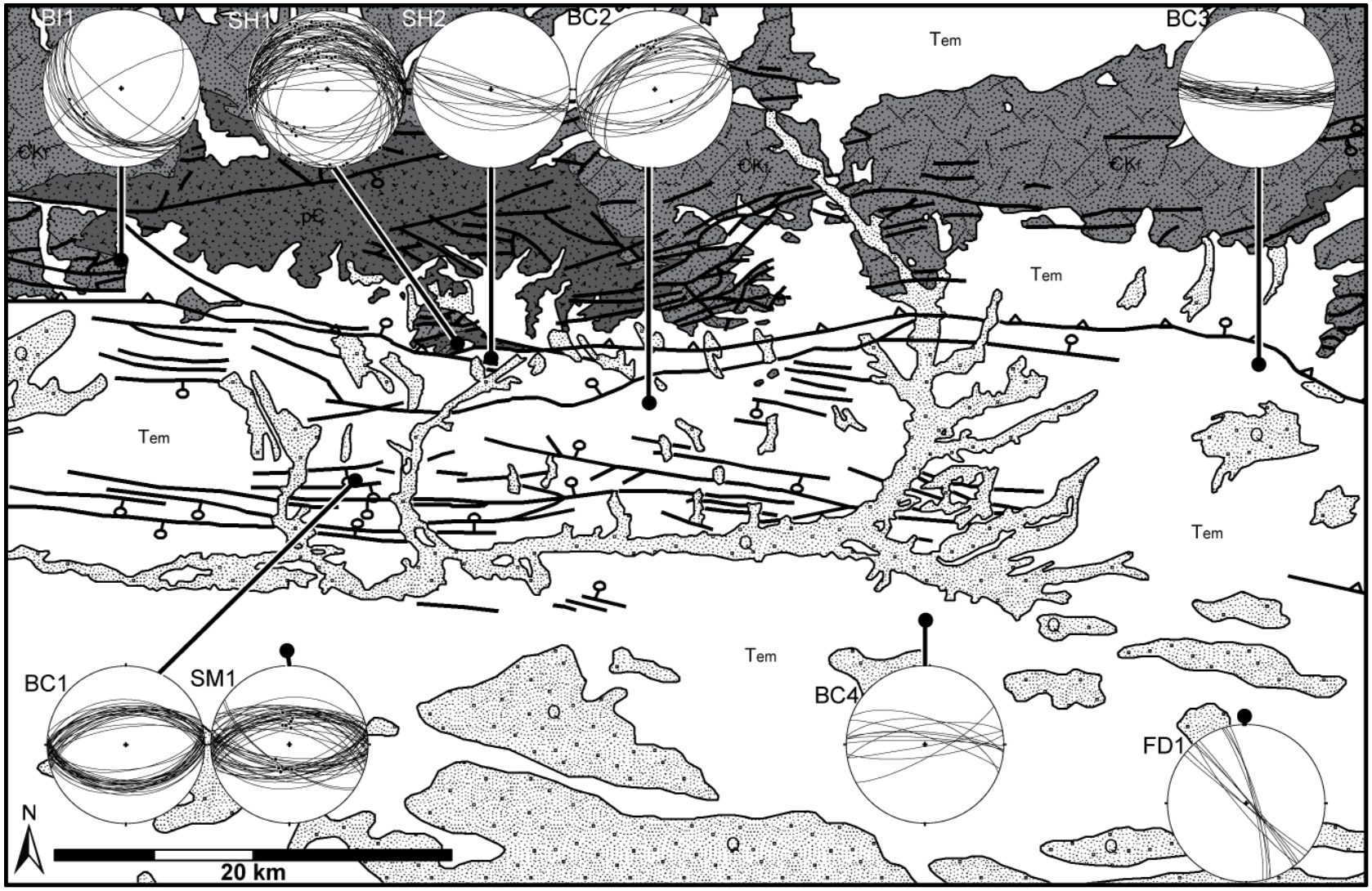

Figure 3.6 Stereonets of outcrop fractures (arcs) & lineations (dots): northern margin, see inset 5, Fig. 1.2 for location & unit abbreviations.

CHAPTER 4. FRACTURE ANALYSIS

Fracture analyses were performed on the previously calculated (Hermann, 2009) fault plane solution for the May 17th, 2009 earthquake, all subsurface fractures, and 1628 of the outcrop fractures. The purpose of performing fracture analyses was to model the kinematics—the movement path of the rocks—and the dynamics—the causal stresses acting on the rocks.

This required calculating the inferred stress axes responsible for the fracturing, and extrapolating to the structural development of the basin and basin-bounding arches. The maximum compressive stress, σ_1, and the minimum compressive stress, σ_3, which is perpendicular to the maximum compressive stress, were the two most important stress axes for this study. The calculated results are given in the appendix (Tables A.2-A.6). For the digitized faults, analysis beyond the 2θ vector mean and dispersion calculations already given (Fig. 3.1) was impossible due to the lack of dip data.

Bedding Rotation

Where the bedding dip was more than 15° (Table A.1), outcrop fractures were rotated about the bedding strike back so that bedding was again horizontal. The purpose of rotating the outcrop fracture data was to remove the bedding dip

variable. This brought the outcrop fracture data into the same reference plane as the digitized faults and subsurface fracture data. Subsurface fractures were not rotated because the mean bedding dip, previously interpreted by log analysts from the micro-resistivity image data, was only 2° (calculated from 17 of the 23 wells having bed boundary data in Table A.5) and never above 15°. Comparing a summary of the non-rotated and rotated data (Fig. 4.1) highlights the fact that the fracture data showed strong correlations to bedding, whether they were bedding-perpendicular systematic joints or conjugate minor faults with either bedding-perpendicular or bedding-parallel acute bisectors. Consistency with non-rotated stations in flat-lying units supported rotating the data and the trend of the fractures did not change significantly (Fig. 4.1). Rotation did not noticeably affect the non-systematic joints, as they were generally parallel to bedding dip.

One assumption made when rotating the data was that the bedding strike paralleled the axis of rotation during the tilting of the units, which is typical of cylindrical folds. This assumption does not preclude multiple stages of tilting about the same axis which may have occurred at station SH1 where the bedding may have been tilted syn-Laramide in response to folding along the Owl Creek Thrust and again post-Laramide when the Cedar Ridge normal fault formed parallel to the older thrust.

Rotating the stations in the steeply-dipping units along the Casper Arch (HHA1-3 and W1 & 2) is questionable due to their proximity to the thrust and the possibility that they were emplaced after the bedding was tilted and were due to extension in a shear zone (Erslev, 1991). It appears that the systematic joints

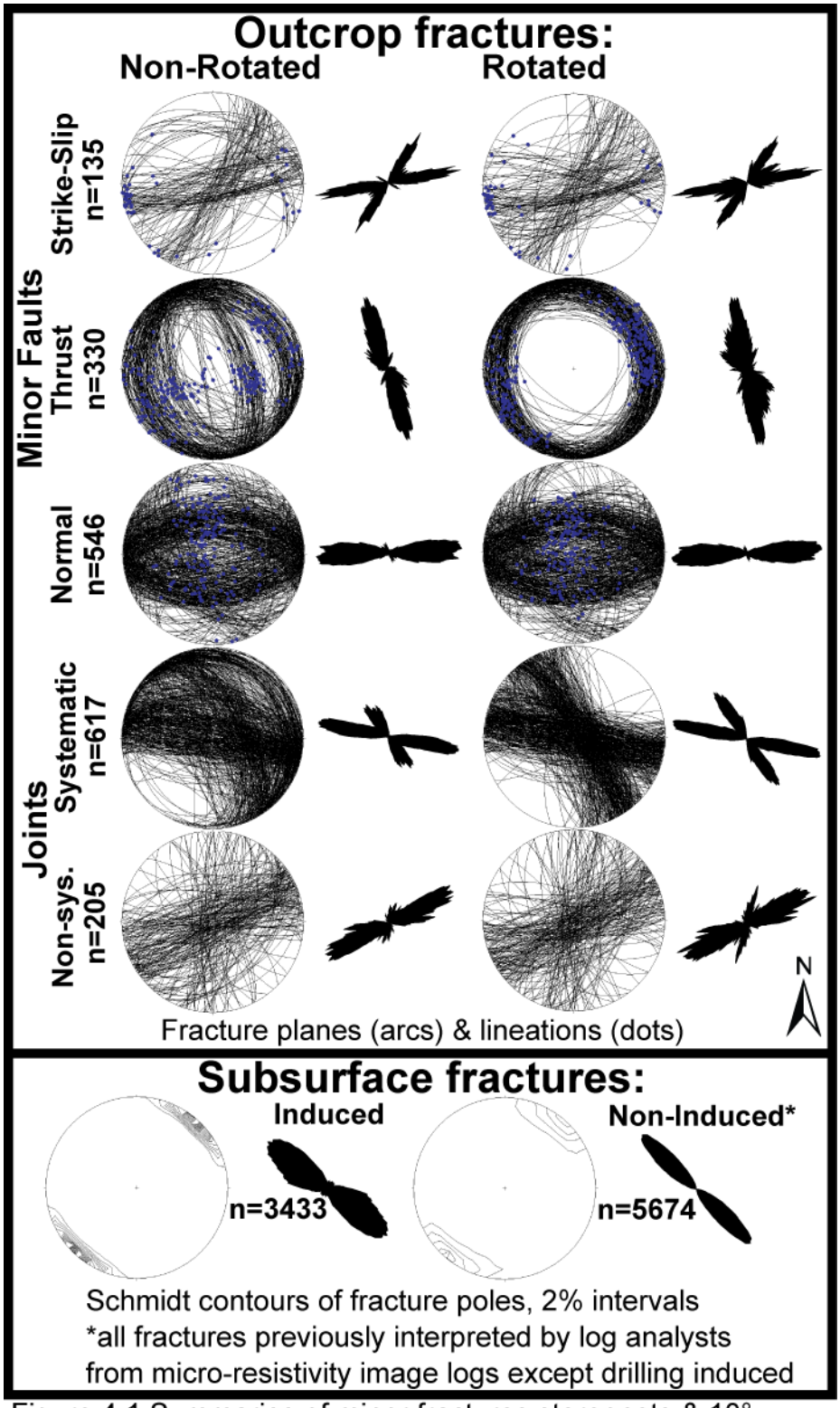

Figure 4.1 Summaries of minor fractures stereonets & 10° smoothed strike rose diagrams

at these stations may have formed shortly after the thrust faults because hardening due to iron-rich fluids preserves both.

Calculating Stress Axes

Eigenvector analysis was performed on the poles to fracture planes and lineations at each station using STEREONET (Allmendinger, 2005) and the results are given as trend-plunge (Tables A.2-A.5). The results include the E_1 vector, which gave the mean pole to the fracture planes or mean lineation; the E_2 vector, which gave the mean conjugate acute bisector; and the E_3 vector, which gave the mean point where conjugate planes cross. Note that for planar features, the E_2 and E_3 vectors are meaningless as they can plot anywhere parallel to the plane. The eigenvalues, which sum to one, are given in parentheses next to the corresponding eigenvector. The E_1 value is a measure of the degree of clustering and can approach one, which is perfect clustering. Theoretically, the E_1 value should be higher for planar features with uni-modal clustering, such as systematic joints, than it would be for conjugate fractures, such as normal faults, with bi-modal clustering. The type of fracturing determined the eigenvector that was inferred to a specific stress axis (Fig. 4.2) following the Andersonian theory of fracturing (Van der Pluijm & Marshak, 2004) which gives thrust, strike-slip and normal faulting end members (Fig. 4.2B) in which the stress axes are orthogonal to the earth's surface.

The assumption made when linking eigenvector analysis to the stress axis is that the fractures analyzed were not influenced by pre-existing weaknesses such as existing fractures. Pre-existing fractures in preferred orientations would

Figure 4.2 Comparison of styles of fracturing with associated strain & stress axes assuming no pre-existing weaknesses. Stereonets (A) show the strain axes associated with a single fracture plane (colored arc & pole) with ε_3 being 45° from the lineation on the fault (gray dot). Block diagrams (B) show end member fracture styles & associated stress axes where the stress axes are orthogonal to the earth's surface. Stereonets (C) show the eigenvectors, which are calculated from the conjugate planes shown, and the inferred stress axes. Note: for jointing only one strain & stress axis is given because the other two axes can lie anywhere in the plane of a joint.

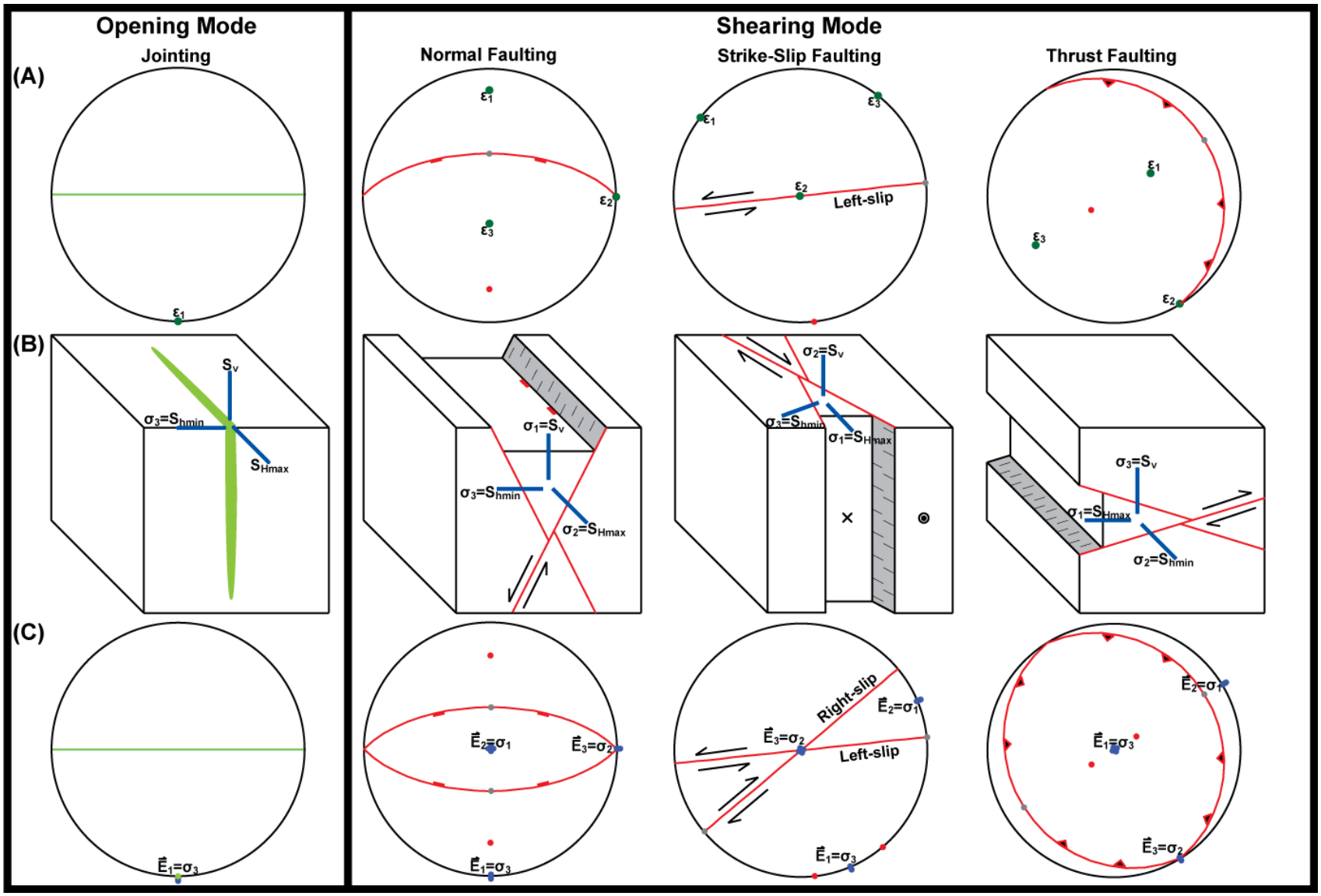
Opening Mode
Shearing Mode
Jointing
Normal Faulting
Strike-Slip Faulting
Thrust Faulting
(A)
(B)
(C)
ε_1
ε_2
ε_3
Left-slip
Right-slip
S_v
S_{Hmax}
$\sigma_3=S_{hmin}$
$\sigma_1=S_v$
$\sigma_2=S_{Hmax}$
$\sigma_1=S_{Hmax}$
$\sigma_2=S_v$
$\sigma_2=S_{hmin}$
$\vec{E}_1=\sigma_3$
$\vec{E}_2=\sigma_1$
$\vec{E}_3=\sigma_2$

slide before new fractures formed because the coefficient of sliding friction is usually less than the coefficient of internal friction (Fig. 4.3). The possible range of orientations for pre-existing fractures to slide is defined by these two coefficients and the differential and mean effective stresses. Observations supporting control by pre-existing weakness, such as reactivation of slickensides with over-printing slickenlines, were not found in this study.

For uni-modal features like bedding and joints, the eigenvector analysis directly calculates the mean pole, which in the case of joints is the inferred minimum compressive stress. When analyzing conjugate fractures however, eigenvector analysis was performed twice. This was because there is usually more of one conjugate at any given station, for example, more left-slip than right-slip faults, and doing this avoids weighing the analysis towards the more measured conjugate. This was done by calculating the mean pole for each conjugate using eigenvector analysis. The mean planes could then be easily calculated from these poles. The mean lineation associated with each conjugate was also calculated using eigenvectors.

Eigenvector analysis was then performed a second time on the two mean conjugate planes in order to calculate the inferred stress axes (Fig. 4.2). Performing the eigenvector analysis a second time on the mean lineations for each conjugate calculated the inferred slip vector as E_1. Eigenvector analysis was done a third time to find means from multiple stations.

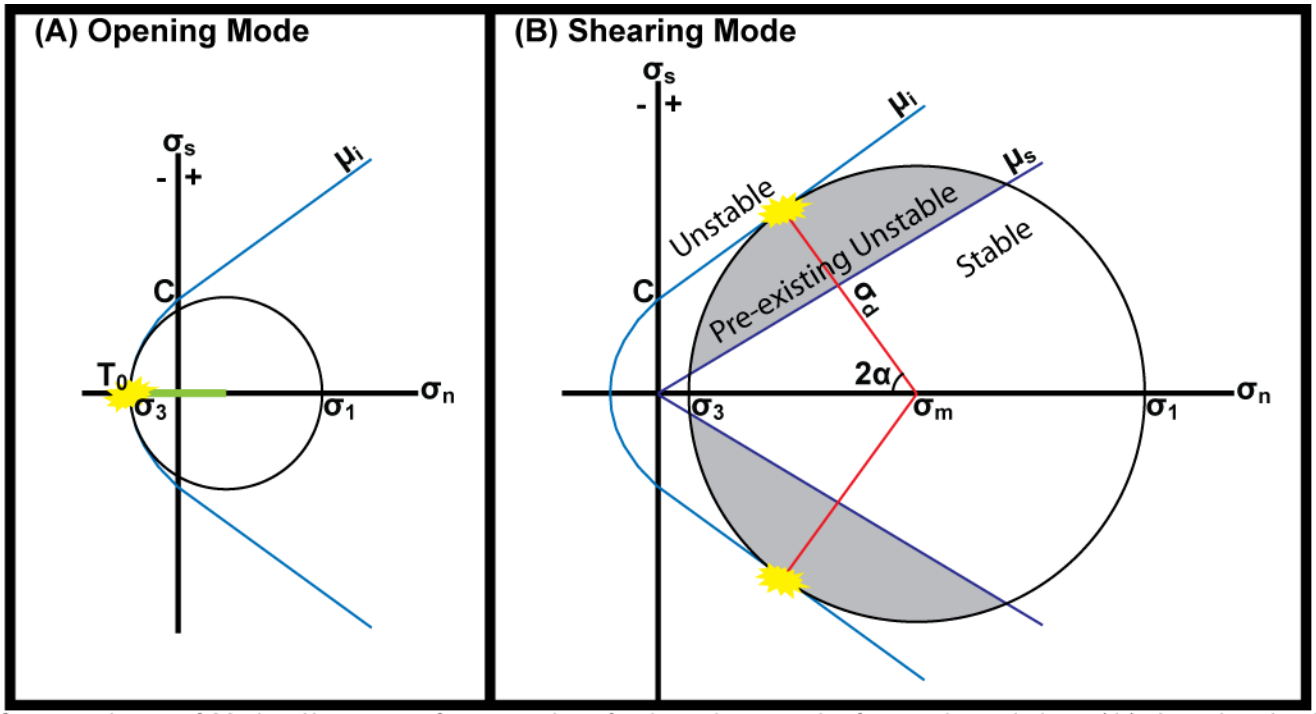

Figure 4.3 Comparison of Mohr diagrams for opening & shearing mode fracturing. Joints (A) develop in the plane of zero shear stress (σ_s) parallel to the σ_1 direction when the σ_3 magnitude equals the tensile failure (T_0) of the rock. Faults (B) develop in non-fractured rock when the deviatoric stress (σ_d=radius of the Mohr circle defined by the magnitudes of σ_1 & σ_3) intersects the failure envelope whose slope equals the coefficient of internal friction (μ_i) at an angle (α) which is the acute angle between the fault plane and the σ_1 direction. The cohesion (C) is a measure of the shear strength of the rock. Pre-existing fractures whose 2α angle intersects the failure envelope defined by the coefficient of sliding friction (μ_s) will slide before new fractures form. Decreasing pore pressure raises the mean stress (σ_m) and drives the Mohr circle to the right along the normal stress (σ_n) axis.

In addition to eigenvector analysis, the ideal σ_1 method (Compton, 1966) was also calculated using SELECT (Erslev, 1998b) with a specified 20° alpha angle which is typical for conjugate sets from across the Rocky Mountains (Erslev & Koenig, 2009) and is the mean for all the conjugate sets from all 42 stations in this study. The ideal σ_1 is only calculated when lineation data is available, so this method did not work for all of the data. This method was used because it calculated trend-plunge of an ideal maximum compressive stress, σ_1, for each lineation, giving more calculated data points than eigenvector analysis (Fig. 4.4). Eigenvector analysis was then performed on the calculated ideal σ_1 results to find their mean.

Thrust and strike-slip faults were typically found in older units whereas the normal faults were typically found in younger units. The station at Muskrat Anticline showed normal faults cross-cutting older thrust faults. Ideal σ_1 and inferred σ_3 results also indicate two distinct fracture sets (Fig. 4.4) and so the minor faults were divided into two sets. Joint

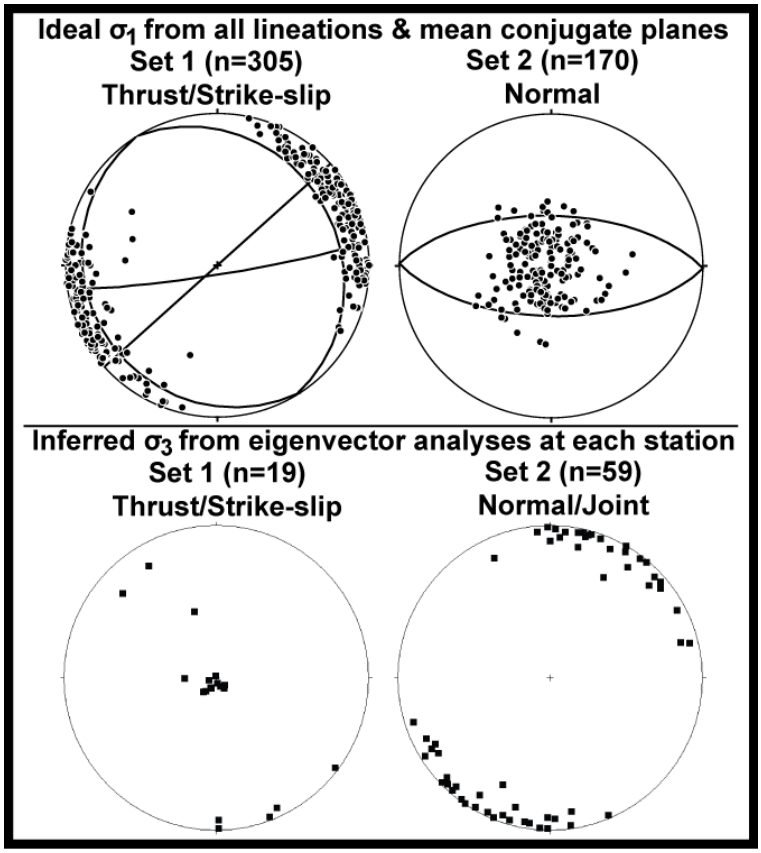

Figure 4.4 Comparison of ideal σ_1 versus inferred σ_3 and set 1 versus set 2 fractures.

and subsurface fractures were included with the normal faults in set two because they are also found across the basin, unlike the strike-slip and thrust faults which are only found along the basin margins, and they both result from a similarly trending bedding-parallel minimum compressive stress (Fig. 4.4).

Set 1: Strike-slip and thrust faults (465 in outcrop)

Both strike-slip (n=135) and thrust (n=330) faults show a bedding-parallel maximum compressive stress whereas the minimum compressive stress varies between bedding-parallel and bedding-perpendicular. The rotated strike-slip and thrust fault data is presented on stereonets (Figs. 4.5-4.7).

Mainly thrust fault slickensides were found along the Casper Arch in the hardened veneers on the steeply-dipping Lance Formation sandstones (Appendix B.10) and these thrust trends closely parallel the approximate surface trace of the Casper Arch Thrust (Fig. 4.5). Along the southern margin, thrust faults parallel local fold axes and the thrust faults at station MA1 (Fig. 3.5) were cross-cut by later normal faults. Excellent outcrops in the Wind River Canyon (Fig. 4.7) show excellent strike-slip conjugates, such as at station WRC9 in the Chugwater Formation, and thrust conjugates in the Flathead Sandstone at station WRC5.

The ideal σ_1 analysis results (Fig. 4.8) of set 1 lineations indicate a N66°E trending maximum compressive stress and range from NNE-SSW to ESE-WNW (Fig. 4.4). Eigenvector analysis of the conjugate sets was also performed (Table A.2) to show its consistency with the ideal σ_1 analysis.

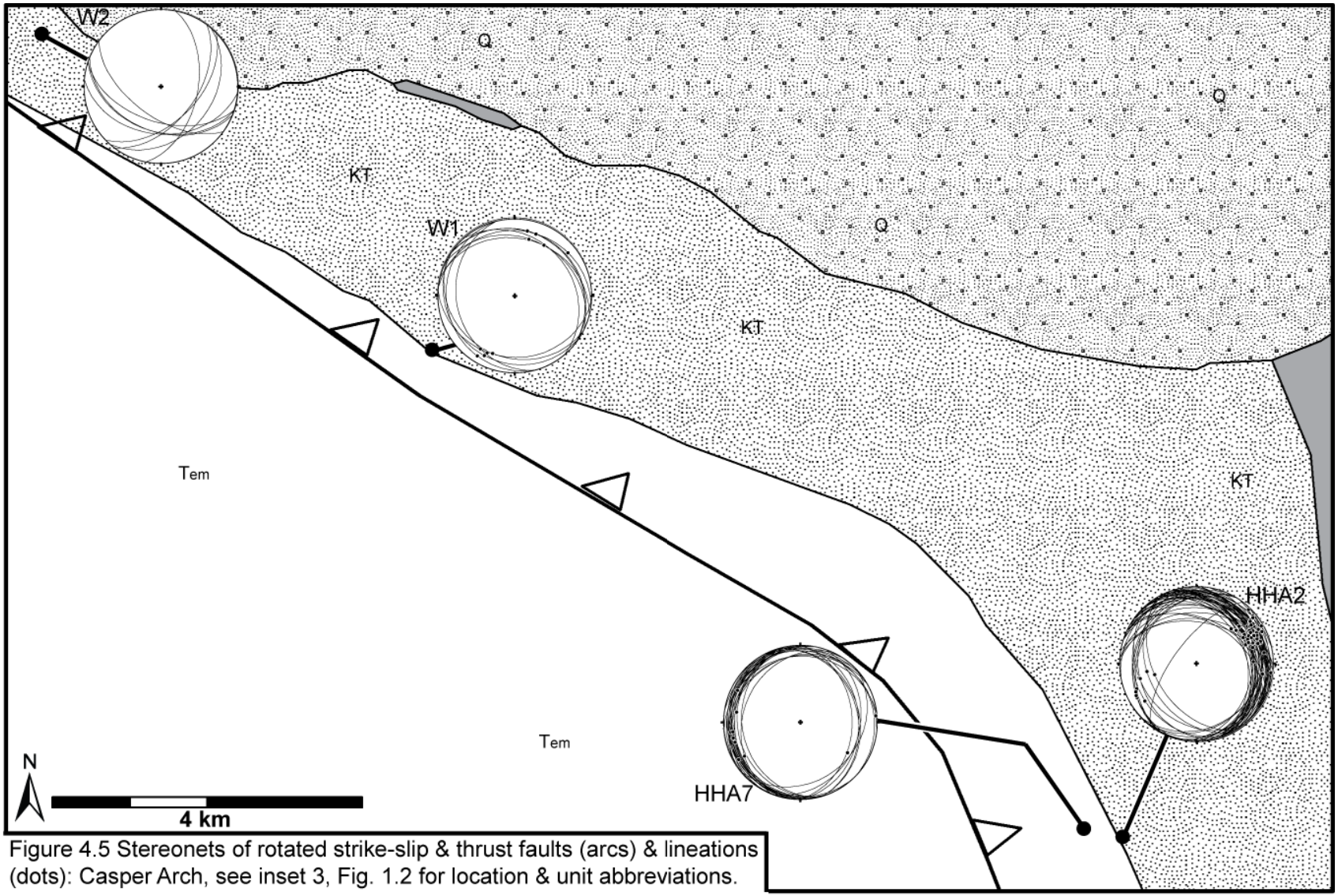

Figure 4.5 Stereonets of rotated strike-slip & thrust faults (arcs) & lineations (dots): Casper Arch, see inset 3, Fig. 1.2 for location & unit abbreviations.

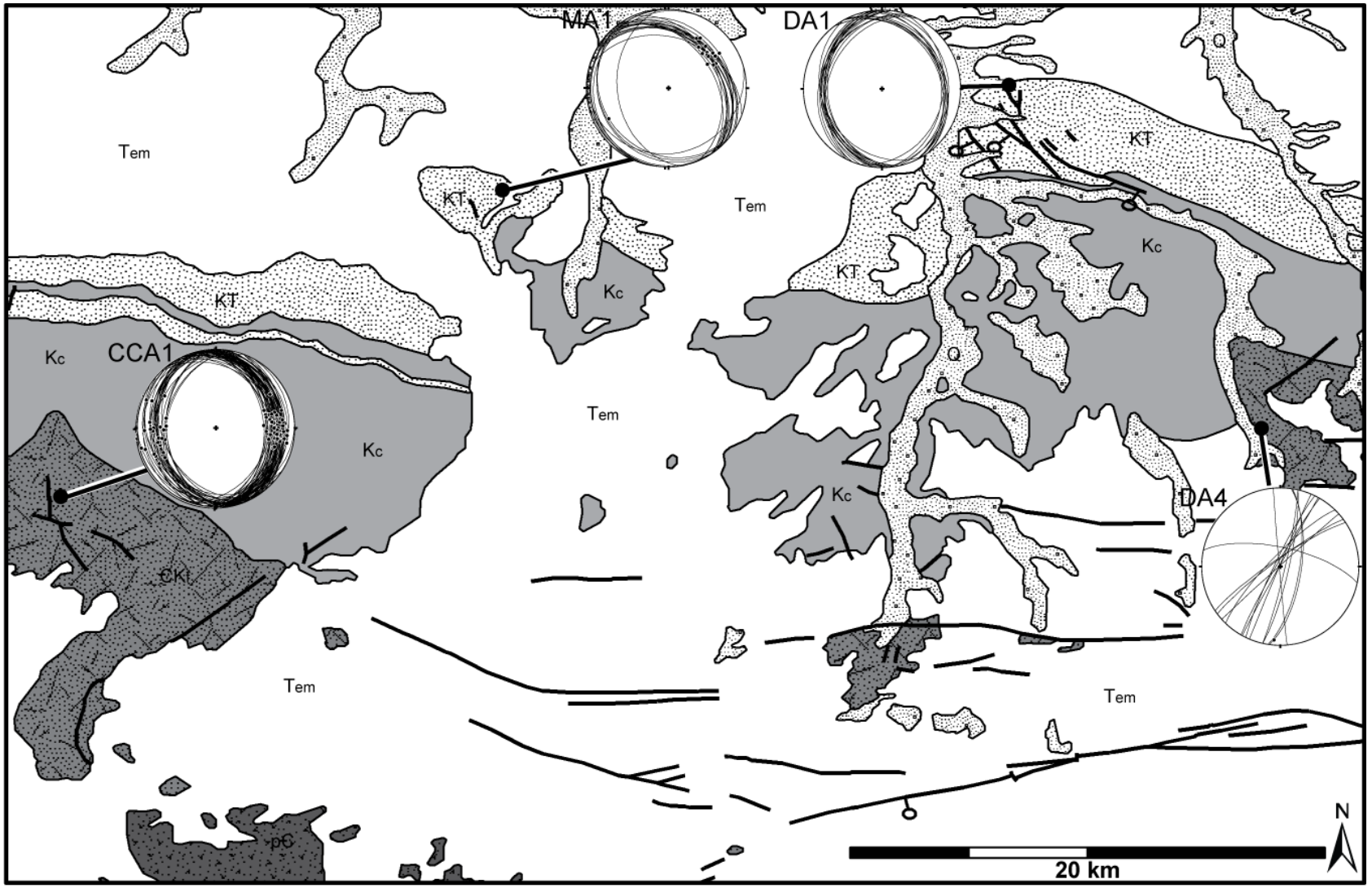

Figure 4.6 Stereonets of rotated strike-slip & thrust faults (arcs) & lineations (dots): southern margin anticlines, see inset 4, Fig. 1.2 for location & unit abbreviations.

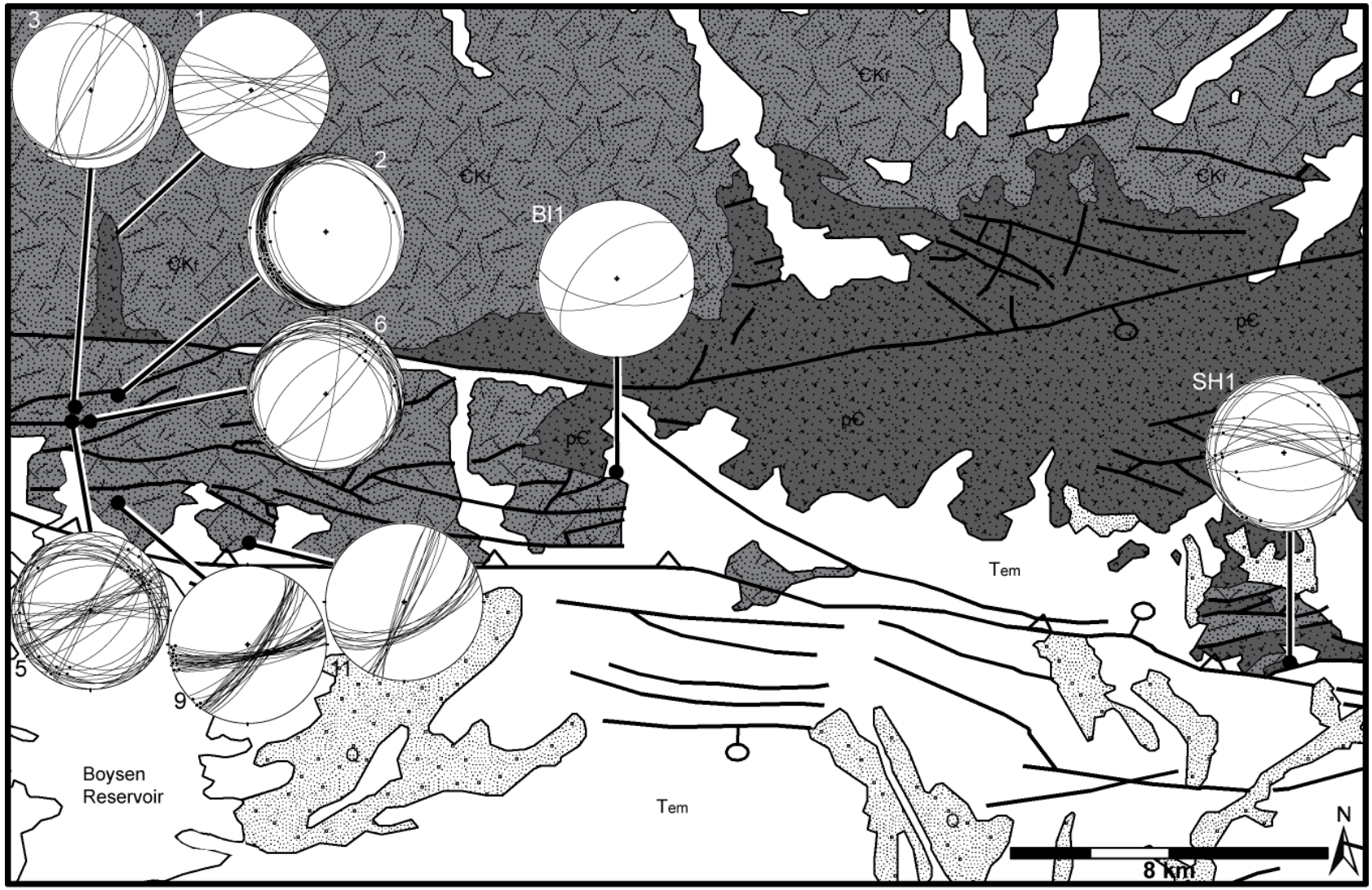

Figure 4.7 Stereonets of rotated strike-slip & thrust faults (arcs) & lineations (dots): Owl Creek Mtns, **s**tations WRC unless noted, see inset 6, Fig. 1.2 for location & unit abbreviations.

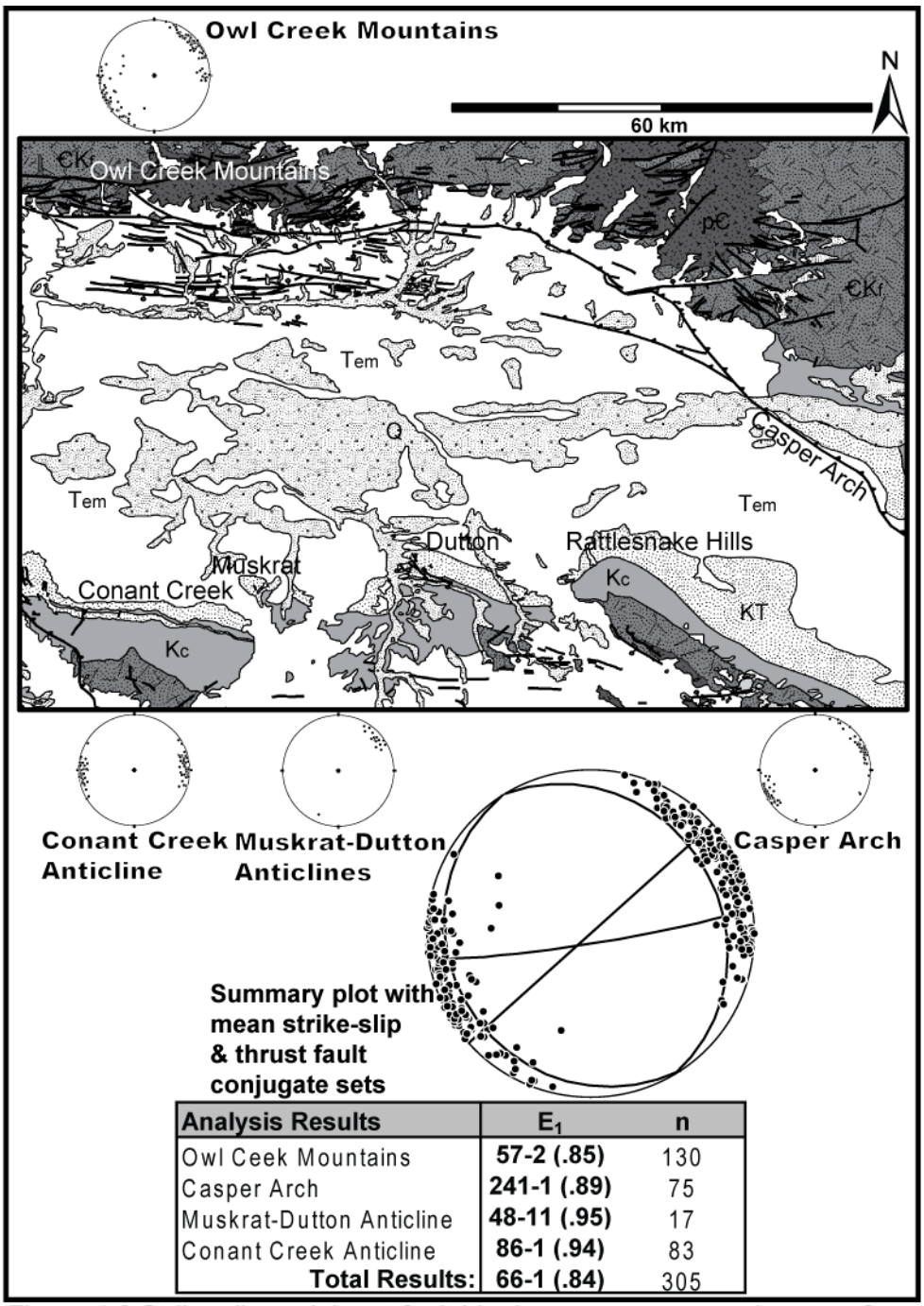

Analysis Results	E_1	n
Owl Ceek Mountains	**57-2 (.85)**	130
Casper Arch	**241-1 (.89)**	75
Muskrat-Dutton Anticline	**48-11 (.95)**	17
Conant Creek Anticline	**86-1 (.94)**	83
Total Results:	**66-1 (.84)**	305

Figure 4.8 Strike-slip and thrust fault ideal axes, mean conjugates, & mean results, see inset 7, Fig. 1.2 for location & unit abbreviations.

In this set, the E_2 vector corresponded to an inferred σ_1 for these faults as it parallels the acute bisector of the conjugate planes.

Set 2: Normal faults & systematic joints (1163 in outcrop, 9107 in subsurface, 1 earthquake)

Both normal faults (n=546 in outcrop) and systematic joints (n=617 in outcrop) give a bedding-parallel minimum compressive stress whereas the maximum compressive stress may be bedding-perpendicular, in the case of the normal faulting in this study (Fig. 4.4), or parallel to the plane of joints, in which case it may, or may not be, bedding-perpendicular. The rotated normal fault and systematic joint data from outcrop is presented on stereonets (Figs. 4.9-4.13).

In the western portion of the Wind River Basin, the systematic joints observed (Fig. 4.9) either paralleled anticlines on the western margin (station WD1) or the northern basin-bounding faults (station MC1). As a side note, northwest-southeast-trending discontinuities parallel the systematic joints at WD1 in the Wind River Formation. These discontinuities look like stretch marks and may be indicative of jointing in unconsolidated sediment. They are 1 cm deep, 5 cm wide, and tens of meters long, with ridges in the depression perpendicular to the long axis of the feature and they appear to be composed of the same fine-sand and silt as the surrounding matrix.

In the Wind River Canyon (Fig. 4.10), normal faults and joints on the eastern side of the Wind River, in the Bridger Mountains proper, have a more WNW-ESE trend whereas those on the western side of the Wind River, in the Owl Creek Mountains proper, have a more WSW-ENE trend. Slickensided normal faults are common in the Paleozoic units whereas cataclasite bands and

conjugate fractures with vertical, bedding-perpendicular acute bisectors are common in the Tertiary units.

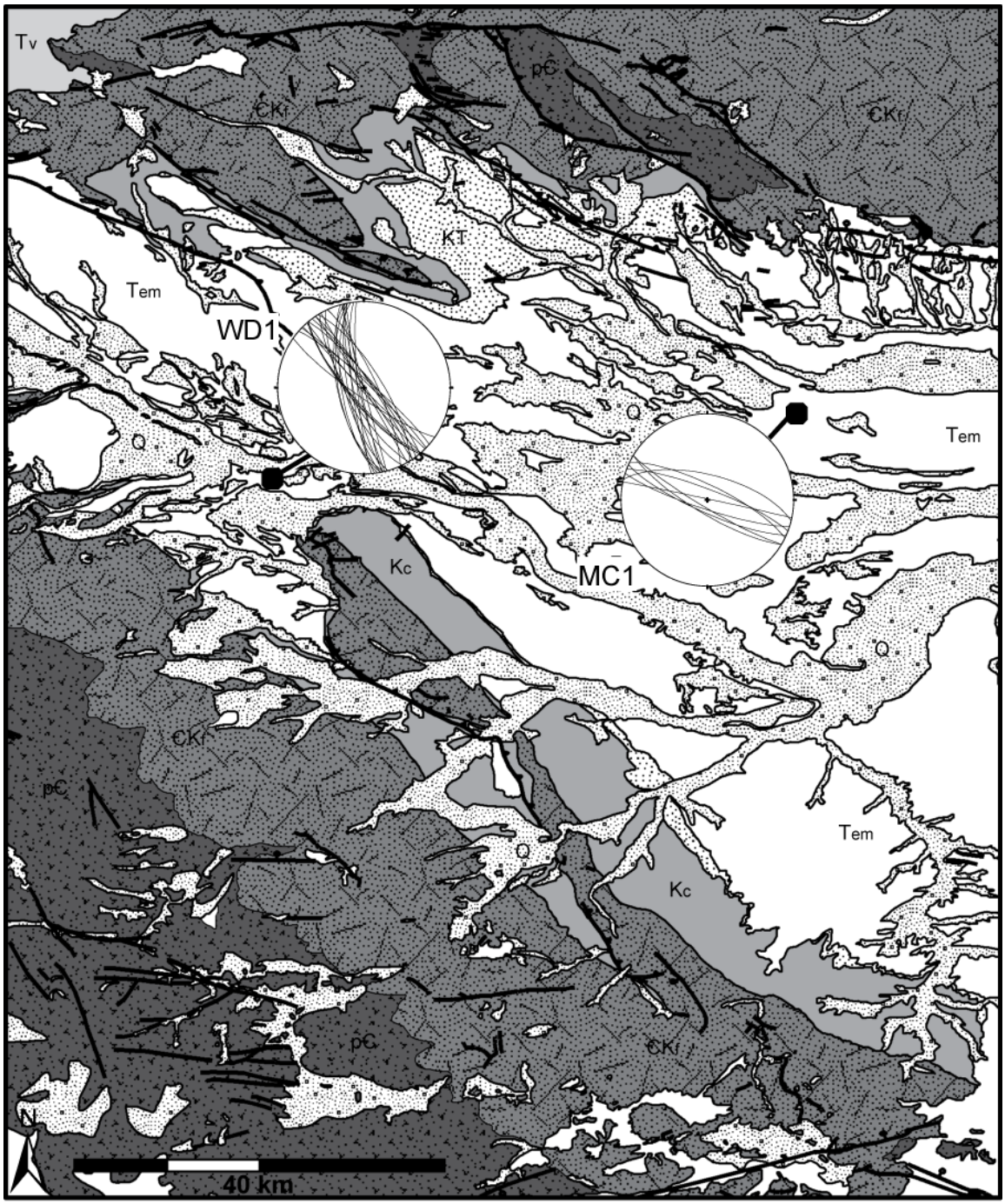

Figure 4.9 Stereonets of rotated systematic joints (arcs): western Wind River Basin, see inset 1, Fig. 1.2 for location & unit abbreviations.

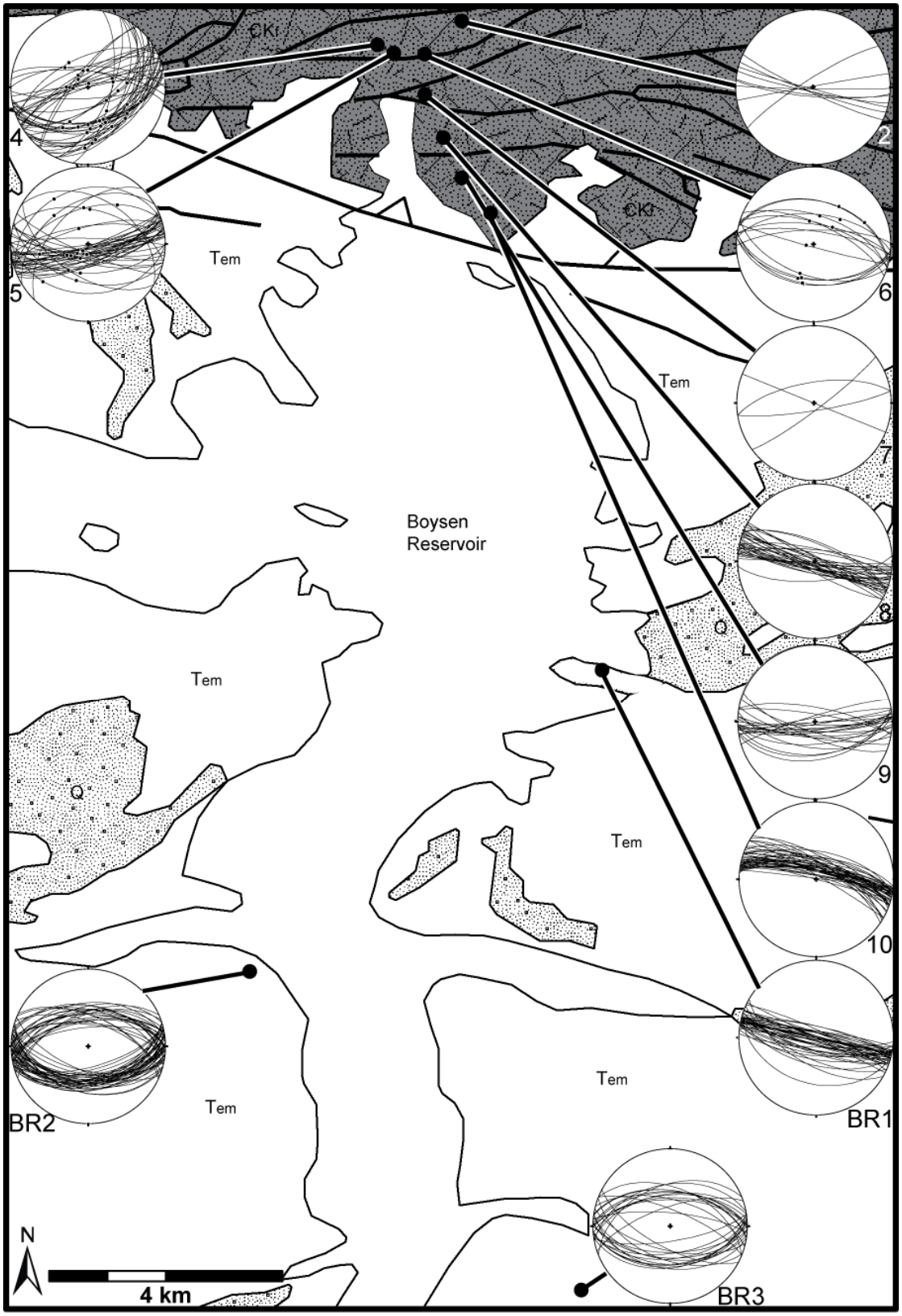

Figure 4.10 Stereonets of rotated systematic joints & normal faults (arcs) & lineations (dots): Wind River Canyon, stations WRC unless noted, see inset 2, Fig. 1.2 for location & unit abbreviations.

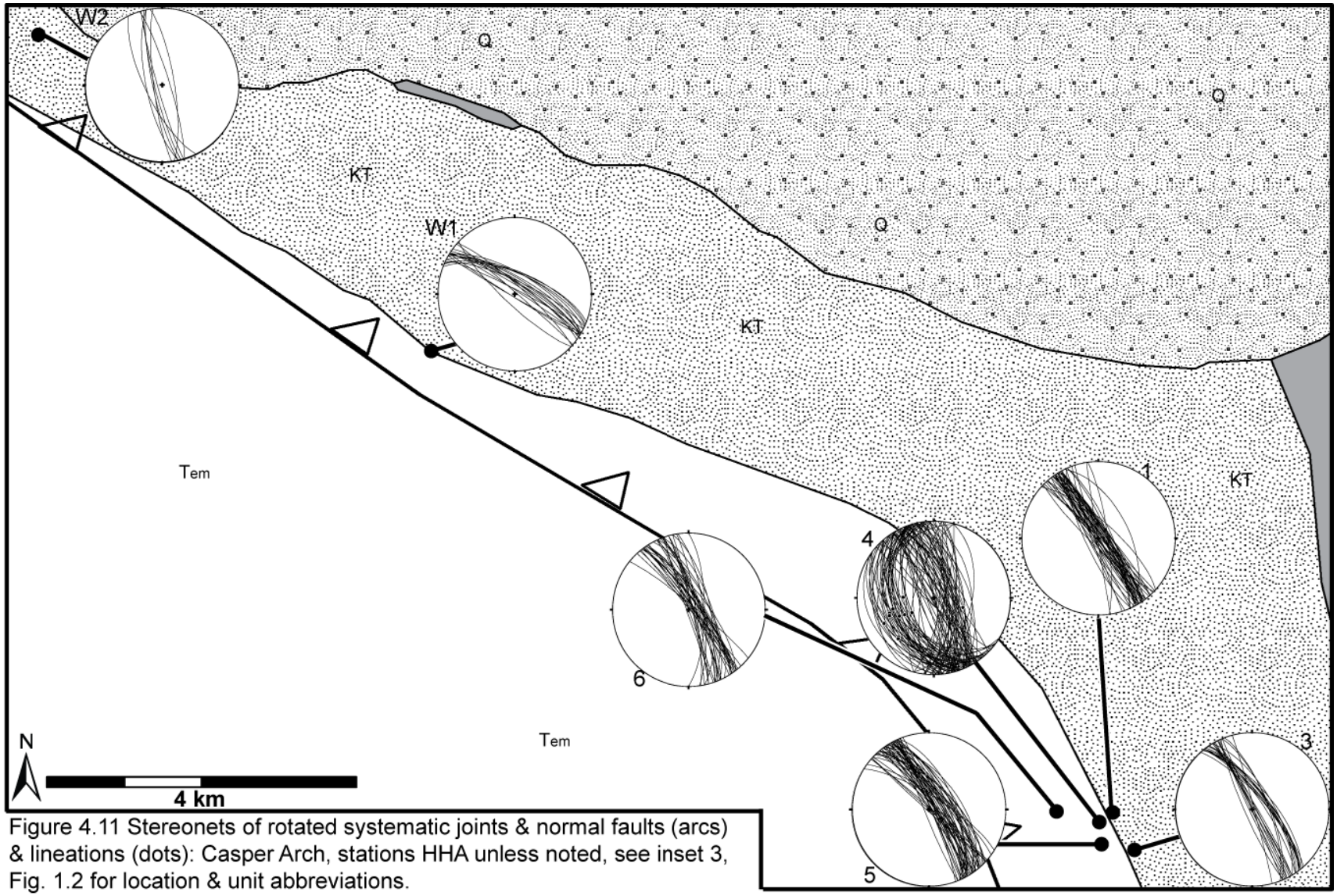

Figure 4.11 Stereonets of rotated systematic joints & normal faults (arcs) & lineations (dots): Casper Arch, stations HHA unless noted, see inset 3, Fig. 1.2 for location & unit abbreviations.

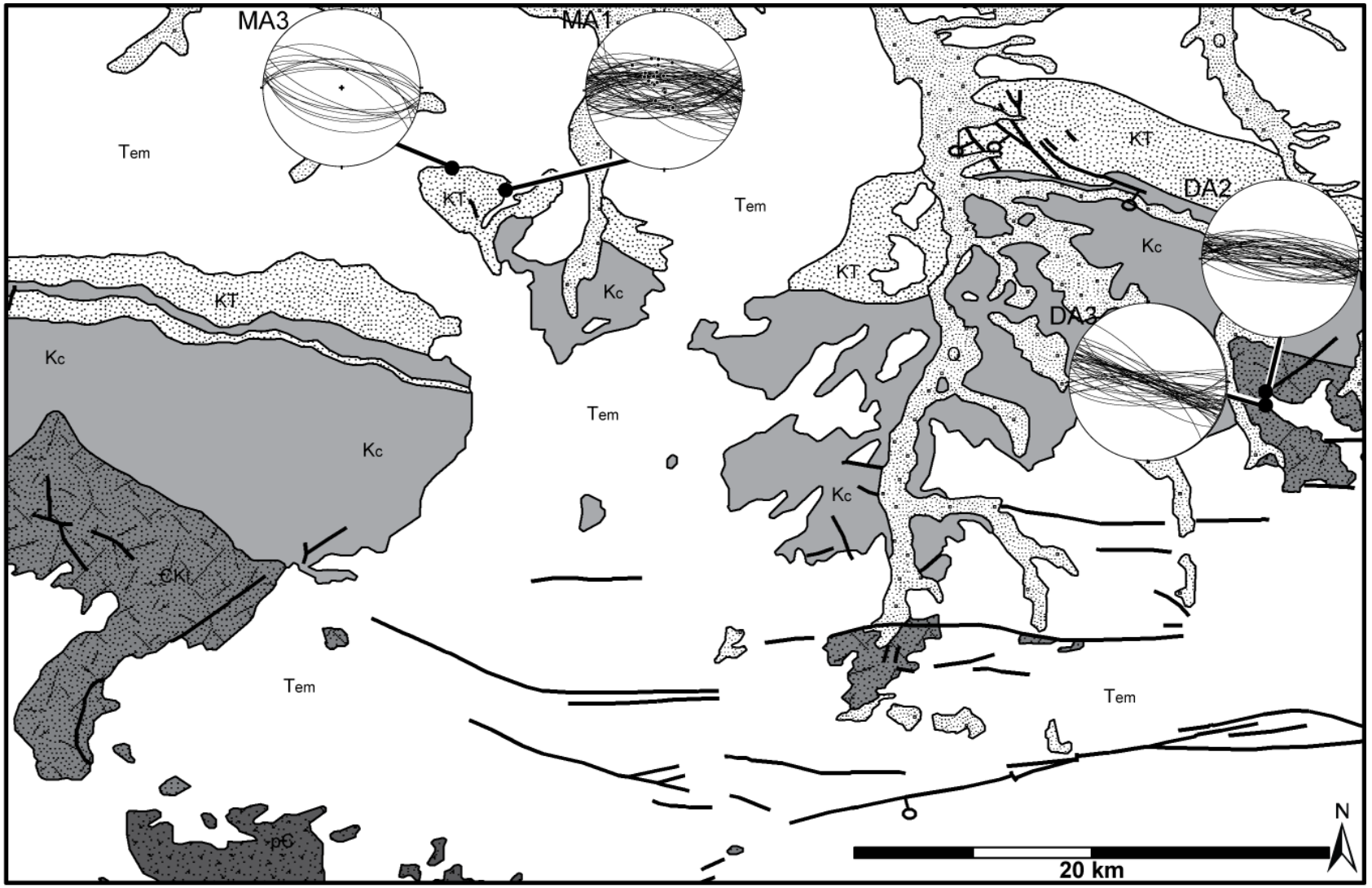

Figure 4.12 Stereonets of rotated systematic joints & normal faults (arcs) & lineations (dots): southern margin anticlines, see inset 4, Fig. 1.2 for location & unit abbreviations.

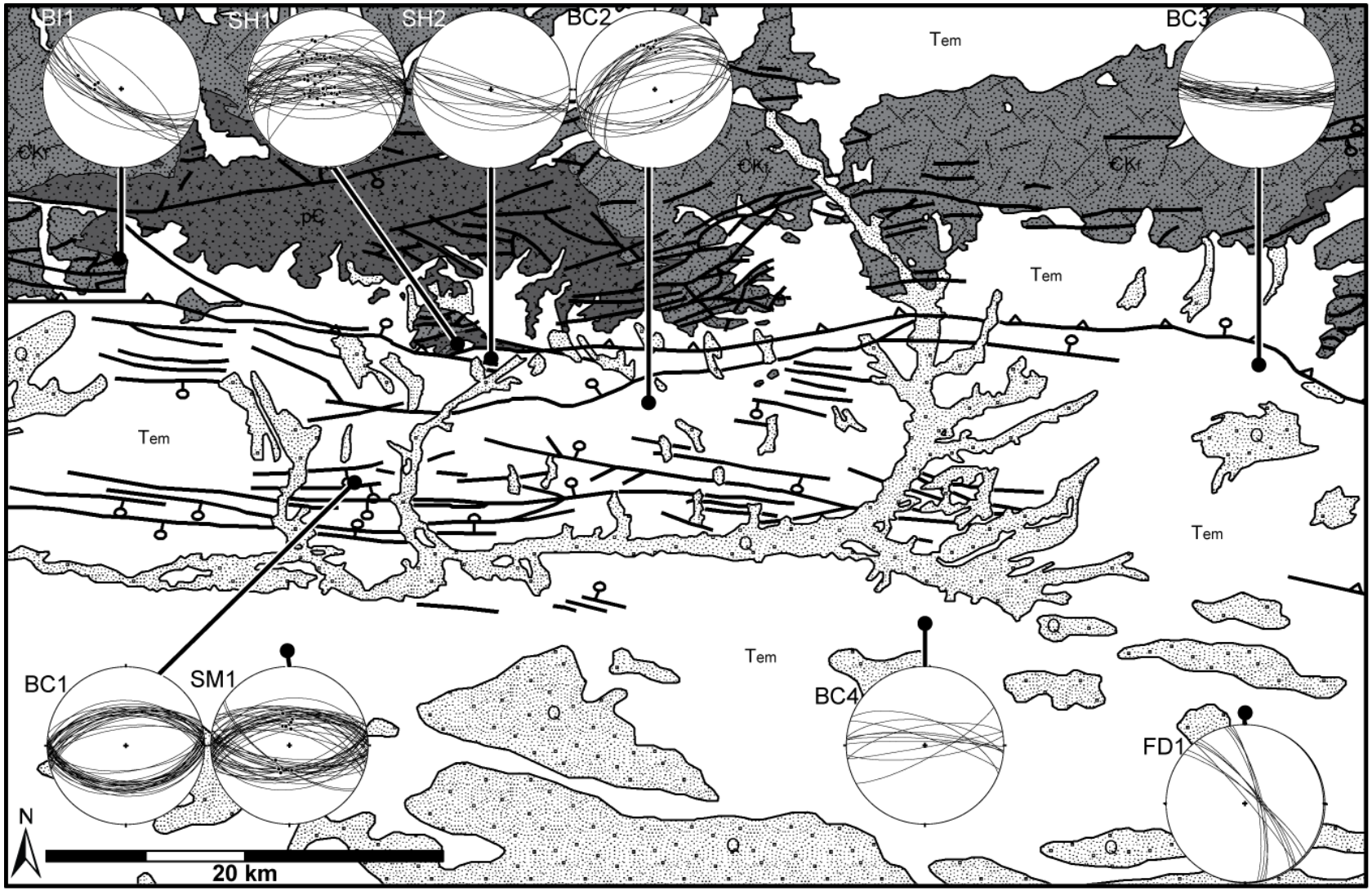

Figure 4.13 Stereonets of rotated systematic joints & normal faults (arcs) & lineations (dots): northern margin, see inset 5, Fig. 1.2 for location & unit abbreviations.

In the vicinity of Hells Half Acre along the Casper Arch, strikes of normal faults and joints in steeply-dipping and shallowly-dipping units both closely paralleled each other and the approximate surface trace of the Casper Arch Thrust (Fig. 4.11). The normal faults at station HHA4 may have been due to local topographic collapse (Appendix B.8).

Along the southern margin of the basin, the normal faults and joints paralleled the North Granite Mountains Fault system (Fig. 4.12). Station MA1 (Fig. 3.5) contained normal faults that cross-cut thrust faults.

Along the northern margin, normal fault and systematic joint strikes closely parallel the approximate surface trace of the Owl Creek Thrust (Fig. 4.13) where it protrudes into the basin around Copper Mountain and back around the embayment in which Madden gas field is located. More consistently striking east-west normal faults and systematic joints were found farther into the basin.

Because ideal σ_1 analysis results for normal faults are sub-vertical (Fig. 4.4) and because each systematic joint pole is a direct measurement of the inferred σ_3, the inferred σ_3 became more valuable for this set and so the ideal σ_1 results were not used. From the eigenvector analyses results (Tables A.3 & A.4) the inferred σ_3 can be obtained from the fracture planes and the inferred slip vector from the lineations. In this set, the inferred σ_3 was the E_1 vector for the planes and the E_2 vector from the lineations represented the inferred slip vector.

The subsurface data is presented on stereonets, with all the data from Frenchie Draw plotted on a single stereonet (Fig. 4.14) using Schmidt contours,

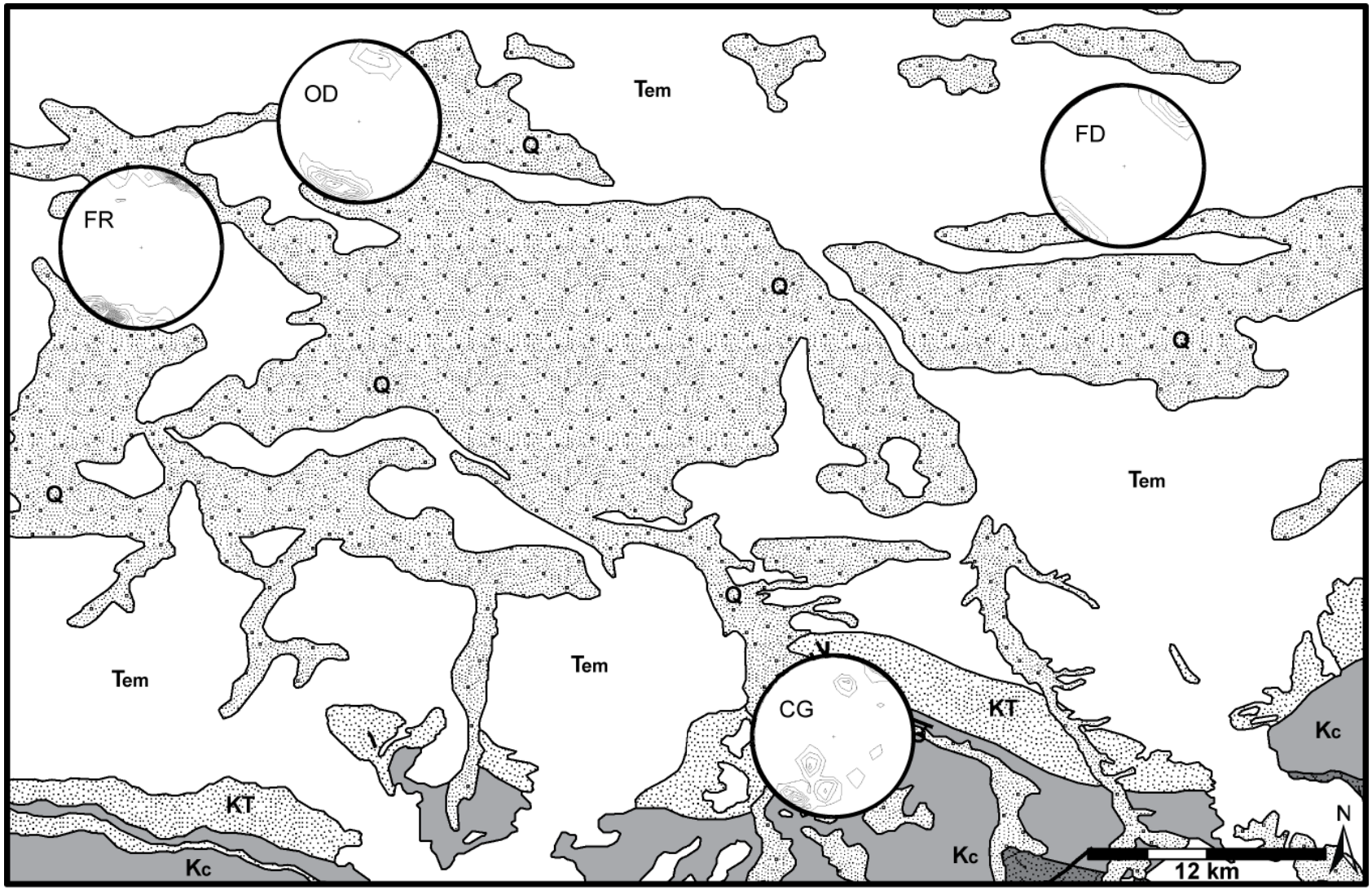

Figure 4.14 Non-induced fractures from micro-resistivity image logs, Schmidt contours, 2% intervals, see inset 8, Fig. 1.2 for location & unit abbreviations, FR: Fuller Reservoir; OD: Ocla Draw; CG: Castle Gardens; FD: Frenchie Draw.

partly because of the large amount of data, but mostly in order to blur the individual locations in a proprietary data set owned by EnCana Oil & Gas (USA) Inc. These stereonets are centered above approximate well locations, or at the approximate center of the field in the case of Frenchie Draw.

Eigenvector analyses were used to individually calculate the inferred stress axes for the induced fractures (n=3433), which result from the modern stresses, and the non-induced fractures (n=5562), of which the majority are natural (Table A.5). The E_1 vector was used as an inferred σ_3 direction because the majority of the fractures were joint-like and bedding-perpendicular (Figs. 4.15 & 4.16) and only a few (n=75) were previously interpreted as faults by log analysts. For example, the drilling-induced and borehole breakout features, which result from the present day stress field, tended to have tightly clustered strikes and 95% had dips greater than 74°. Breaking down the data by fracture category at Frenchie Draw (Fig. 4.15) further emphasized the bedding-perpendicular nature and parallelism of the majority of the fractures. However, the most certain natural fracture categories—the mineralized fractures and faults—differed (Fig. 4.15) in that they commonly had lower dips and more scattered strikes. This may have been due to the presence of some northwest-southeast and east-west-striking normal conjugate faults. Where these fractures dominate, the E_2 vector may represent the inferred σ_3 axis instead of the E_1 vector because the E_1 vector plots vertically.

The modern inferred stress axes (Fig. 4.17) were mainly calculated from the drilling-induced fractures, however, in two wells, this data was not available

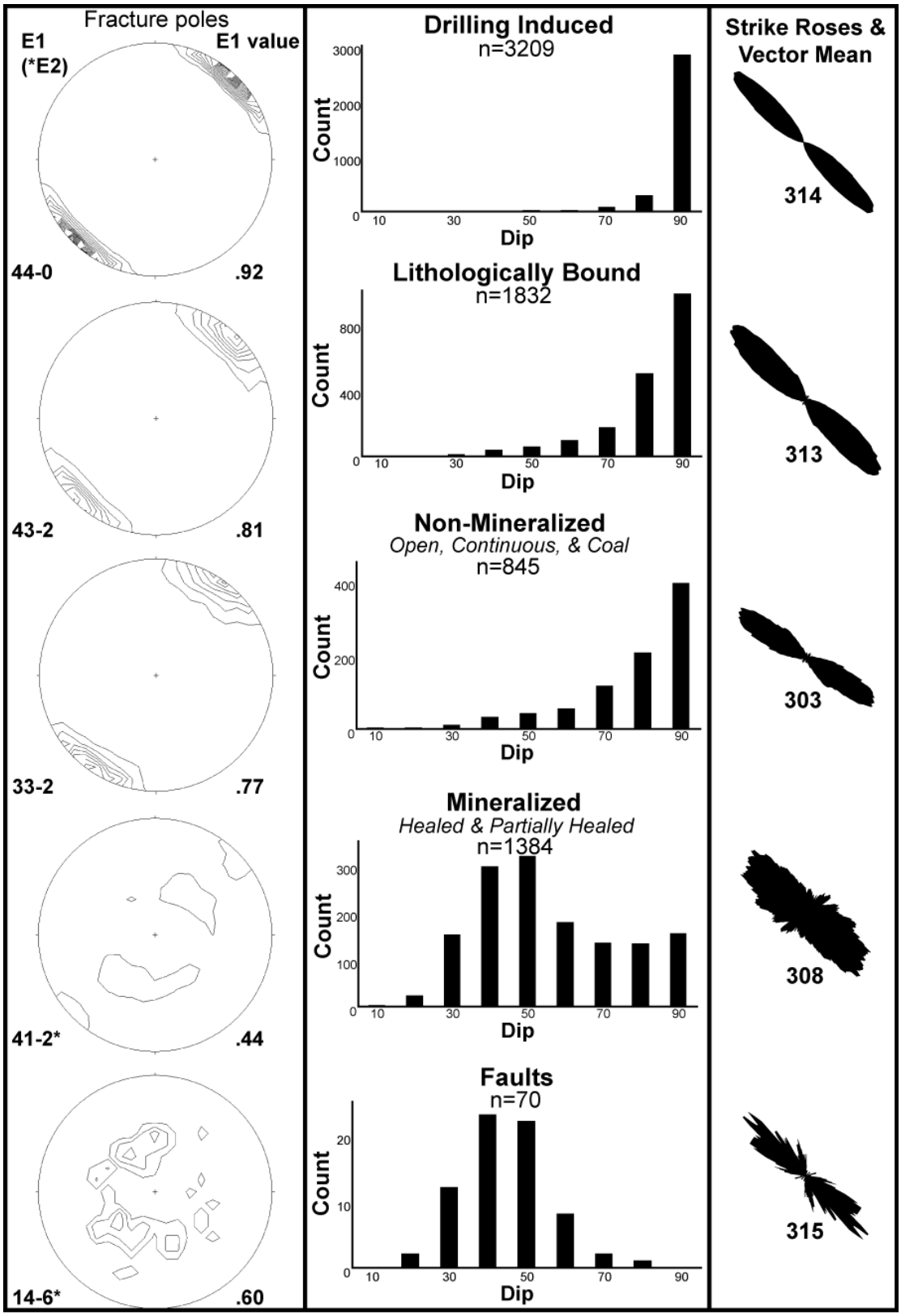

Figure 4.15 Subsurface fractures by category at Frenchie Draw, (20 wells) Schmidt contours, 2% intervals, dip histrograms, 10° smoothed rose diagrams.

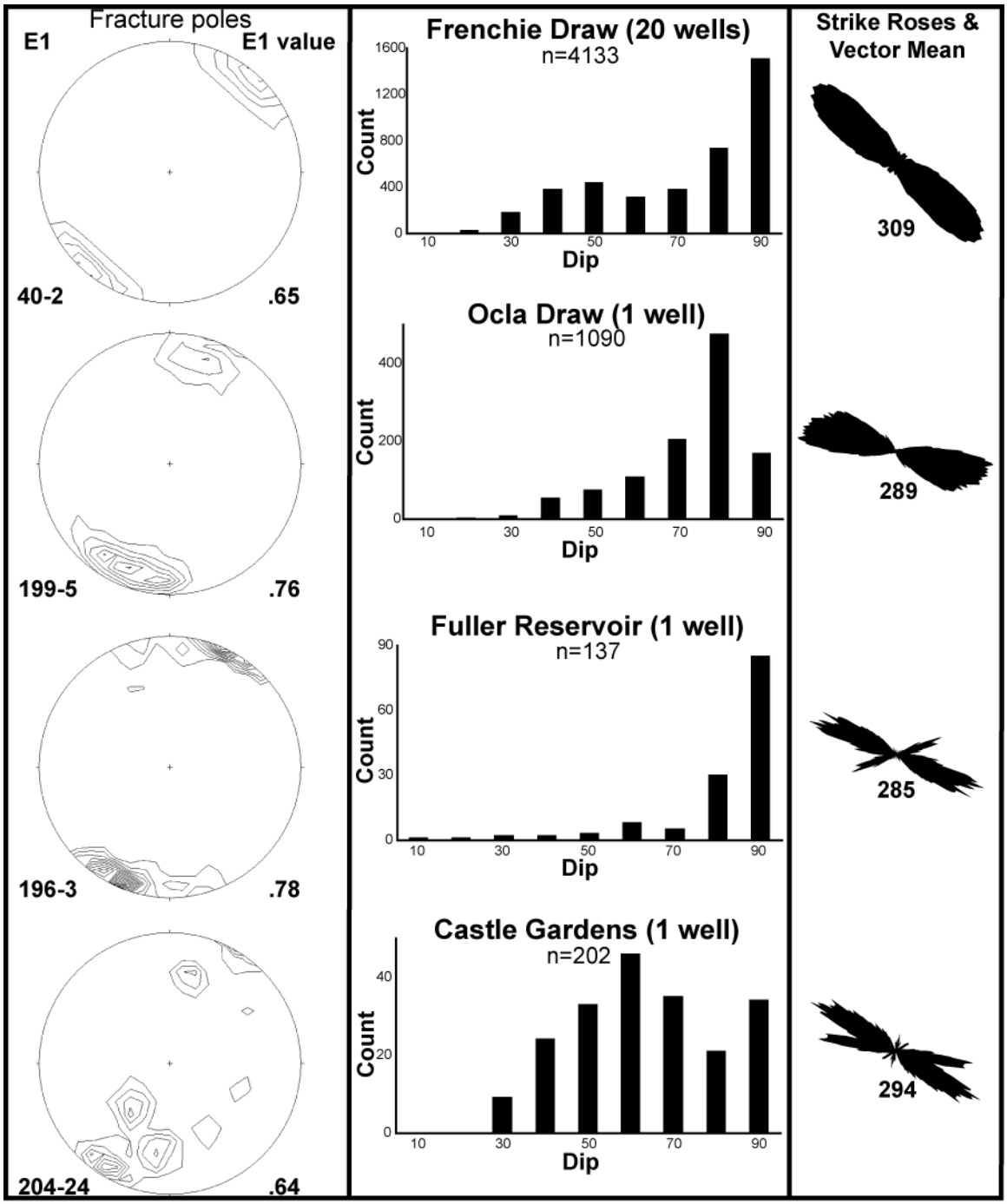

Figure 4.16 Subsurface non-induced fractures by field, Schmidt contours, 2% intervals, dip histrograms, 10° smoothed rose diagrams.

and borehole breakouts were used instead (Table A.5). Because borehole breakouts were interpreted by previous log analysts as planar features

perpendicular to drilling-induced fractures, eigenvector analysis could still be used with the inferred σ_3 being 90° from the trend of E_1. The mean trend of the inferred σ_3 for these features is N39°E. Another source of data was the single location in the study area from the World Stress Map database (Heidbach, 2008), which was also from borehole breakout.

In addition, a shallow 3.7 magnitude earthquake, which occurred May 17th, 2009, gave insight into the modern stresses in the Granite Mountains. The fault plane solutions for this earthquake (Fig. 4.17) were calculated by Hermann (2009) and showed a higher-angle plane oriented N71°E-73° and a lower-angle plane oriented N50°W-30°. Due to the earthquake's close proximity to the north-dipping South Granite Mountains Normal Fault, which strikes N70°W, and the earthquake's identification as being due to a roughly east-west trending normal fault (Hermann, 2009), the likely fault plane solution is the high angle plane, suggesting that, if perpendicular to the likely fault plane solution, the inferred σ_3 may trend N19°W.

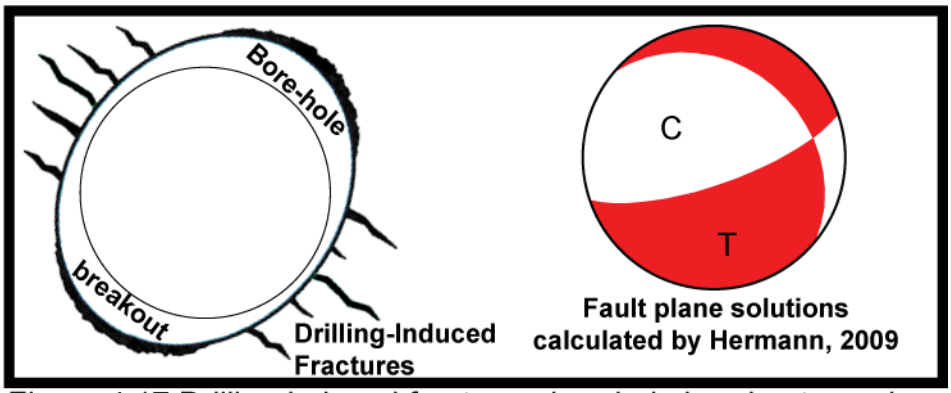

Figure 4.17 Drilling-induced fractures, borehole breakouts, and the May 17th, 2009 earthquake.

The majority of the digitized faults (Fig. 3.1) were mapped as normal faults and so in order to be directly comparable with set 2 fractures, the normal fault and systematic joint strikes at each location in this set were analyzed for their 2θ vector mean (Figs. 4.15, 4.16, & Table A.6) using LDIS (Erslev, 1998a). The calculated dispersions are not given because the eigenvalues already gave measures of clustering.

The 10° smoothed strike diagrams for this set are plotted along with the digitized strike diagrams and modern maximum compressive stress axes (Fig. 4.18). In this figure, the base map only displays the Cody Shale in order to highlight the anticlinal structures and Quaternary alluvium because the modern drainages tend to parallel faults observed from seismic data (P.J. Wynne, 2008, personal communication) and set 2 fracture strikes. Of note is that the fracture strikes in set 2 parallel the trapezoidal margins of the basin, with northwest-southeast-striking domains along the eastern and western margins and through the middle of the basin, and east-west-striking domains along the northern and southern margins (Fig. 4.18) extending to about 20 km into the basin from both the northern and southern margins. These two domains are easily observed in the summary of all the systematic joint data (Fig. 4.1) and also in the normal fault data, although less easily observed due to the dominance of normal faults striking east-west. These two domains in fracture set 2 were used to calculate two separate, bedding-parallel inferred σ_3 mean trends of N44°E for the northwest-southeast domain and N7°E for the east-west domain (Fig. 4.19).

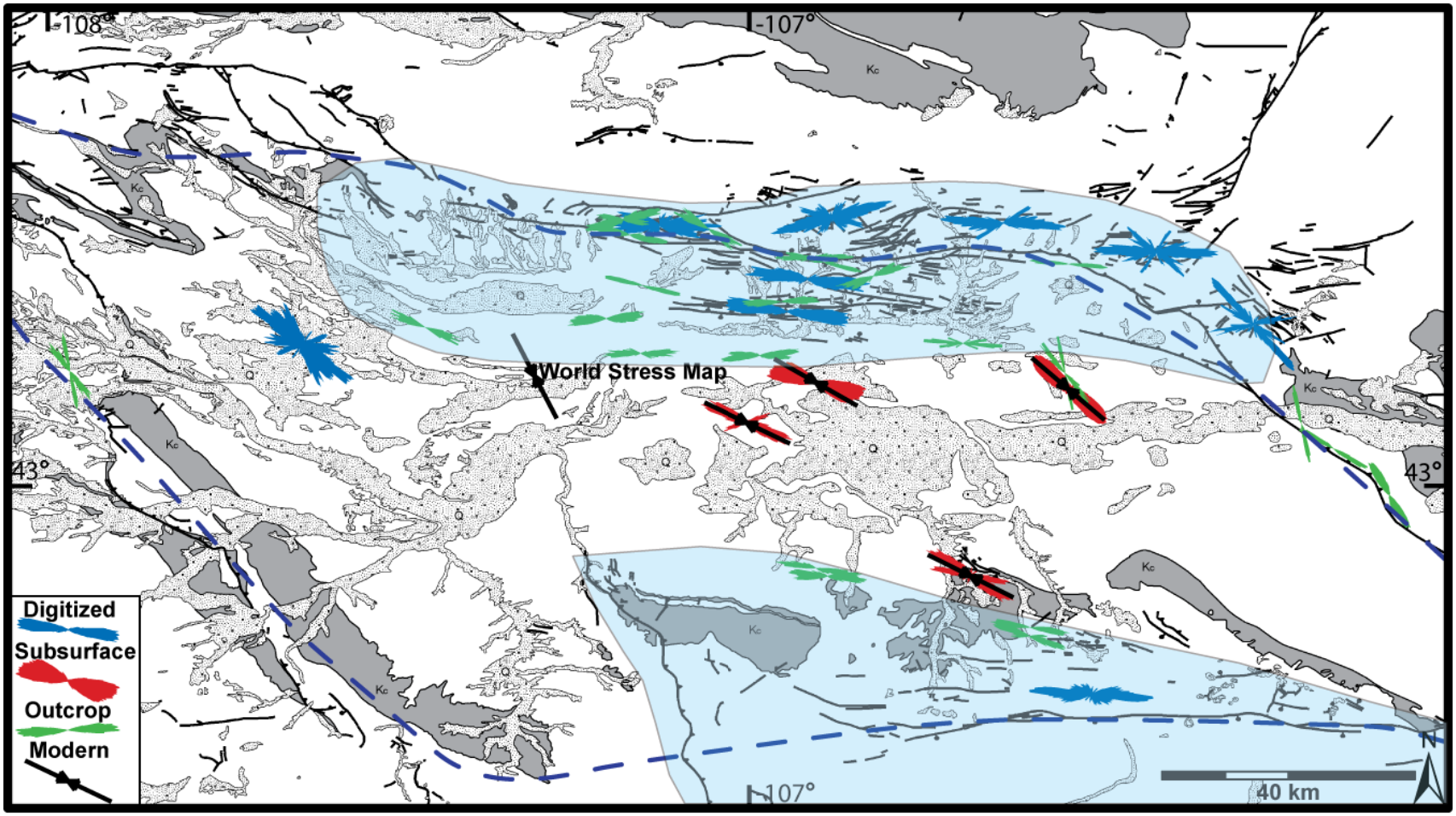

Figure 4.18 Fracture strike rose diagrams, 10° smoothed, digitized faults (blue), subsurface non-induced fractures (red), & outcrop systematic joints & normal faults (green) with modern maximum compressive stress trend (black arrows). Note how fracture strikes parallel the margins of the basin with a northwest-southeast trend and east-west trend (east-west domains highlighted in blue).

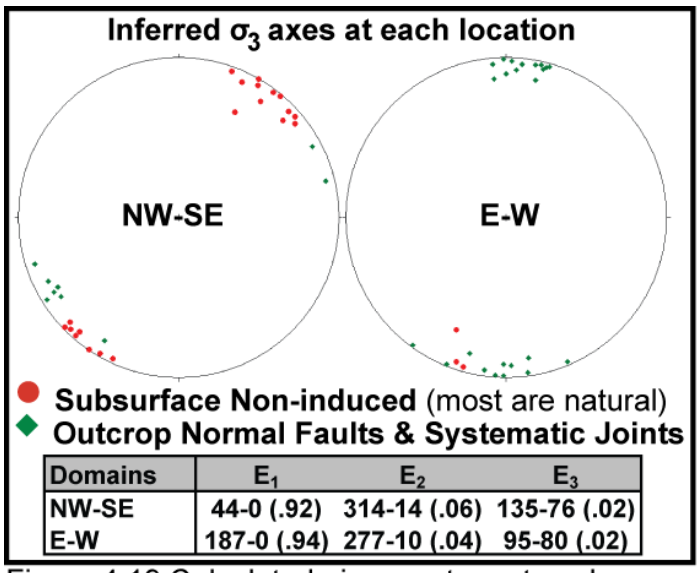

Domains	E_1	E_2	E_3
NW-SE	44-0 (.92)	314-14 (.06)	135-76 (.02)
E-W	187-0 (.94)	277-10 (.04)	95-80 (.02)

Figure 4.19 Calculated eigenvectors at each location grouped by the two domains, and used to calculate minimum compressive stress trends.

CHAPTER 5. DISCUSSION

Hypotheses for the causal mechanisms and timing of the observed fractures include fracture development due to: 1) pre-Laramide distal compression or forebulge migration during the Sevier orogeny; 2) syn-Laramide ENE-WSW horizontal compression; and 3) multiple post-Laramide hypotheses for fracture development including: i) near-surface topographic collapse and exhumation; ii) elastic strain release shortly following Laramide shortening; iii) left-slip faulting resulting in the basin's trapezoidal shape; iv) broad regional extension due to extensional plate interactions or epeirogenic uplift; and v) localized extension coupled to backsliding on listric thrust faults and collapse of basin-bounding arches.

Results from the fracture analyses performed were used to test these hypotheses. Fracture analysis methods relied on calculating the ideal σ_1 trend using lineation data or inferring the stress axes using calculated mean eigenvectors. Ideal σ_1 and inferred σ_3 results indicated two distinct fracture sets (Fig. 4.4).

The first set consisted of 135 strike-slip and 330 thrust faults that gave a calculated ENE-WSW bedding-parallel maximum compressive stress axis (Fig. 4.8). The second set consisted of 546 normal faults, 617 systematic joints, 9107

subsurface fractures, and 1 recent earthquake's previously calculated fault plane solution. This set contained two fracture orientations that gave calculated northeast-southwest and north-south bedding-parallel minimum compressive stress axes.

Mechanisms & Timing

First, a discussion of the relative ages of the units in which the fractures occur is appropriate. At all of the stations except those at Hell's Half Acre, the Wind River Formation is flat-lying (Table A.1), including in the core of Dutton Anticline, and lies above a significant angular unconformity with the Fort Union Formation along the basin margins. At Hell's Half Acre, the Lysite Member of the Wind River Formation dips as much as 24° (station HHA5), but within half a kilometer down-dip to the southwest it becomes flat-lying. It also contains some likely thrust faults at station HHA7 (Table A.1). It is likely that the Lysite Member experienced some continued Laramide shortening after a significant erosional event and was gently up-warped along the Casper Arch. No evidence supporting continued Laramide shortening in the Lost Cabin Member of the Wind River Formation and younger units was observed in this study. All units prior to the Lance Formation are considered pre-Laramide.

1. Pre-Laramide Fracturing:

   Only 16 of the 42 outcrop stations from this dataset were from pre-Laramide units (Table A.1) that are older than the Lance

Formation and the fractures at these stations have the same orientations as those in the younger units (Fig. 4.1, Table A.1-A.6). Because the thrust and strike-slip faults in these units have the same orientation as those in syn-Laramide units, it is not necessary to attribute them to pre-Laramide deformation. Northwest-southeast-striking systematic joints have been attributed to pre-Laramide fracturing due to their presence in both flat-lying and folded lower Cretaceous Frontier Formation sandstone (Hennings et al., 2000; Bergbauer & Pollard, 2004). However, because northwest-southeast-striking joints also appear in units as young as the Oligocene at the southeast corner of the basin (L.E. Hamlin, 2009, personal communication) and in the post-Laramide Wagon Bed Formation (Appendix B.9) and the drilling-induced fractures also strike northwest-southeast, it is not necessary to attribute them to pre-Laramide deformation.

2. Syn-Laramide Fracturing:

All 465 thrust and strike-slip faults from fracture set one were found in Cambrian Flathead Sandstone through the lower Eocene Lysite Member of the Wind River Formation. The ENE-WSW bedding-parallel maximum compressive stress calculated (Fig. 4.8) from these faults is consistent with previously calculated Laramide stress axes (Molzer & Erslev, 1995; Erslev & Koenig, 2009).

Predicted syn-Laramide normal faults and joints would strike either ENE-WSW, as splitting fractures parallel to the maximum compressive stress, or NNW-SSE, perpendicular to the maximum compressive stress due to outer arc extension (Hennings et al., 2000). Both the northwest-southeast and east-west fracture orientations in set 2 strike oblique to these predicted trends. Further, these two orientations are consistent with the modern stress axes (Fig. 4.17).

It is likely that outer arc extension was observed at station MA2 (Fig. 3.5) which is located on the crest of a small fold (Appendix B.7) where the systematic joints paralleled the anticlinal fold axis. It is because of this ambiguity that this station was not included in set 2. Also, ENE-WSW striking joints, which are likely syn-Laramide splitting fractures, were observed in the Cloverly Formation at Dutton Anticline but were not documented due to the onset of winter weather ending the field season. The majority of the field research focused on Eocene and younger units within the basin. It is for this reason that normal faults and joints that could be interpreted as Laramide are not represented in this study.

Although it is possible that pull-apart basins (Nilsen & Sylvester, 1995) in a strike-slip network along the margin of the Owl Creek arch may have mechanically allowed for east-west-striking normal faulting, the large scale of the normal faulting observed is

not consistent with Laramide compression. A plausible mechanism that would allow large-scale east-west-striking normal faulting during the Laramide would be possible compaction of the basin footwall and settling (Molzer & Erslev, 1995) allowing the tip of the east-west-trending Owl Creek hangingwall to collapse into the basin. However, this does not account for the east-west-striking normal faults in the basin footwall itself. A simpler model would be to link the fractures in the hangingwall to the same post-Laramide causal mechanism as the fractures in the basin footwall.

3. Post-Laramide Fracturing:

The vast majority of the fracture data, which comprises fracture set 2, is neither pre- nor syn-Laramide. The hypotheses for post-Laramide fracturing are discussed as follows:

i. Near surface mechanisms

Due to the lack of discernable northeast-southwest-striking joints in the subsurface data (Fig. 4.1), from depths as shallow as 1700 feet in the well at Castle Gardens, the non-systematic joints measured in outcrop with this strike are interpreted as caused by near surface mechanisms. Further, these non-systematic joints generally abutt the systematic joints, indicating they formed later, as they could not propagate across the pre-existing discontinuity.

These two observations support the interpretation that these are secondary, J_2 joints (J_{ns}=J_2). Being non-systematic, fracture analyses were not performed as the error bars for the calculated mean stress axes would be to wide.

The systematic joints (J_s=J_1) are found in the subsurface (Fig. 4.1) and so are not the result of near surface mechanisms. Only a few may have resulted from near surface infilling with the same orientation as existing J_1 joints. In a few instances, mostly near the edges of the outcrop, the J_1 and J_2 joints reversed their timing relationship—meaning that the joints in the J_1 orientation abutted joints in the J_2 orientation.

The northwest-southeast-striking joints are pervasive and consistent across Wyoming and Colorado (Hennings et al., 2000; Bergbauer & Pollard, 2004; Ruf & Erslev, 2005; Gillett et al., 2007; Cooley, 2009; C.L. Allen & L.E. Hamlin, 2009, personal communications) and are found at depths up to 12,300 feet in the subsurface data (Table A.5).

Also, these joints, along with the more east-west-striking joints found along the northern and southern margins, are unaffected by major topographic features such as the Wind River Canyon (Fig. 4.10). Here the systematic joints strike east-west and not north-south as would be expected if they were paralleling the steep

slopes and forming due to topographic collapse into the canyon (Whitehead, 1997).

Further, plotting the inferred σ_3 trends versus the bedding strike, both of which are converted to a single hemisphere by subtracting 180° as necessary, shows low correlation (Fig. 5.1). For this graph,

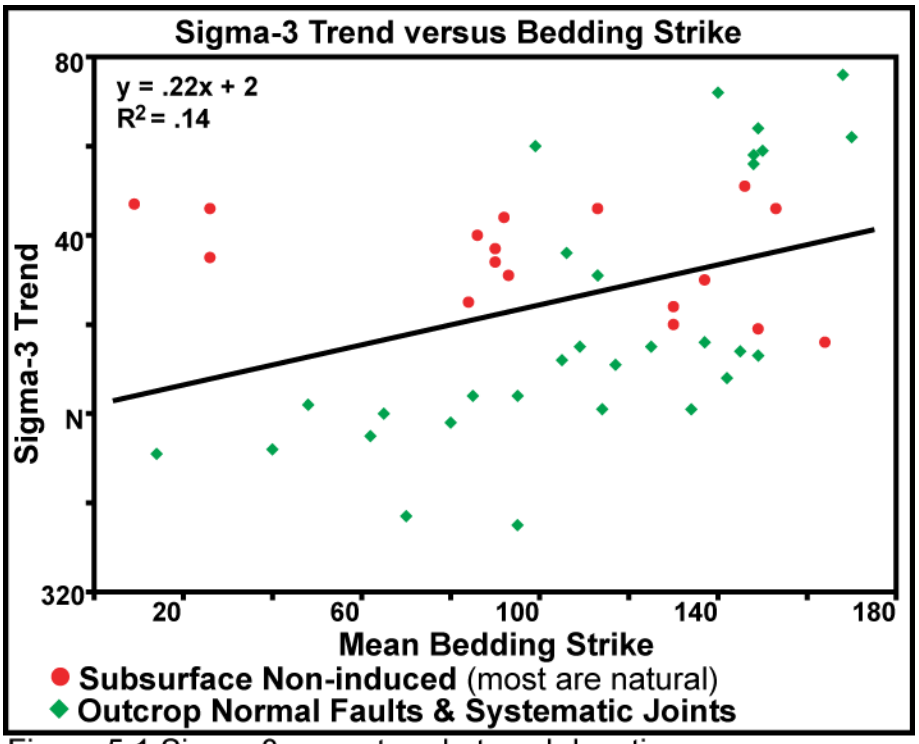

Figure 5.1 Sigma-3 mean trend at each location versus mean bedding strike, error bars are not given due to multiple sources of error including measuring in the field (~2° accuracy) and in calculating the eigenvectors.

the inferred σ_3 trend was preferentially taken from the systematic joint eigenvector analysis results (Table A.3), but also from the normal fault eigenvector analysis results (Table A.4) at stations where systematic joint data was not present. Bedding strike (Table

A.1; A.5) was used as a proxy for topographic slope strike because stations were either located on bedding dip-slopes or were flat-lying.

ii. Elastic strain release

Fractures due to release of Laramide elastic strain would only be possible in units lithified enough to store strain during Laramide shortening, which was unlikely for the Wind River Formation and possibly the Fort Union Formation. Further, trends of Laramide ideal σ_1 directions and trends of post-Laramide inferred σ_3 axes (Fig. 4.4) would be parallel indicating an opposite sense of movement. Predicted NNW-SSE striking joints are not observed. This orientation would be oblique to both the northwest-southeast and east-west-striking normal faults and systematic joints observed (Fig. 4.1).

iii. East-west left-slip faulting

East-west-striking left-slip faults are present in pre-Laramide units as young as the lower Cretaceous Cloverly Formation along the basin margins but were not found at any of the 17 stations in Eocene units (Table A.1) or in subsurface fracture data. Lineation pitches from all units indicate that the sense of movement on the outcrop minor faults is bimodal, with the majority being dip-slip with

little oblique-slip between the strike-slip and dip-slip end members (Fig. 5.2). Further, segregating this data into lineation pitches

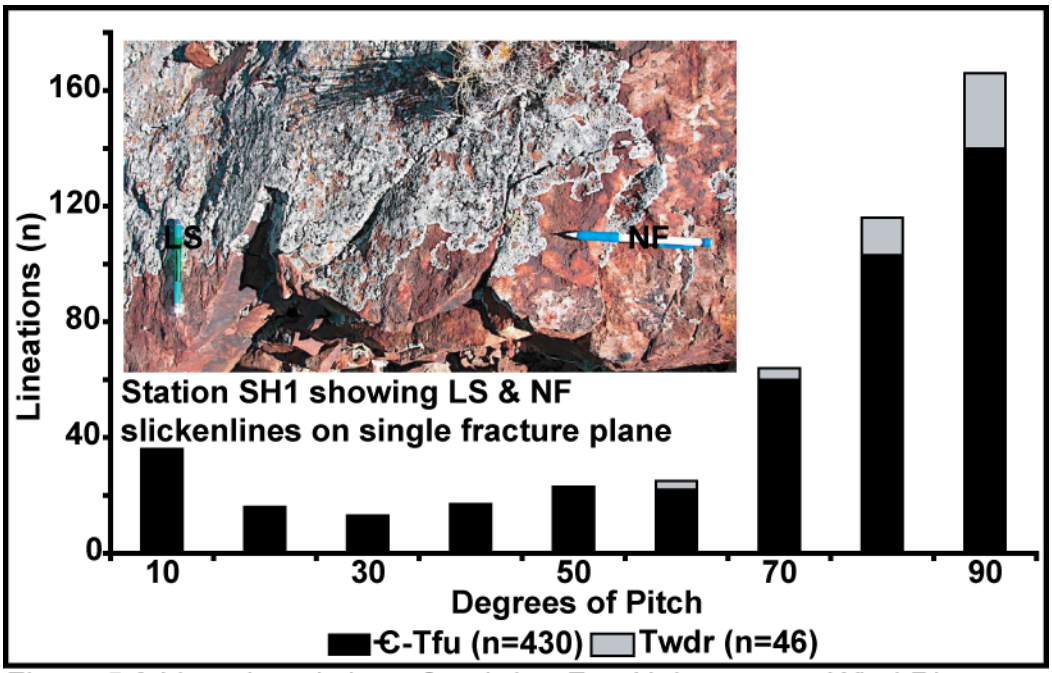

Figure 5.2 Lineation pitches, Cambrian-Fort Union versus Wind River, picture shows the one instance where strike-slip and normal lineations occured on the same plane but did not overlap.

measured in the Wind River Formation versus in older units, shows that although lineations were rarely observed in the Wind River Formation, they do not have a strike-slip component of movement. The calculated minimum compressive stress and the slip vector calculated from the lineations (Table A.4) are very close, indicating no oblique slip.

However, the earthquake that that resulted from the east-west-striking normal fault in the Granite Mountains may have had a small

component of strike-slip (Hermann, 2009) which may have been left-slip. It may be possible that north-south extension reactivated left-slip faults as normal faults along the margin of the Owl Creek arch. This may have been observed at station SH1 (Fig. 3.6; 5.2) where strike-slip and dip-slip slickenlines were found on the same approximate plane. Further, east-west-striking left-slip faulting would predict ENE-WSW striking normal faults and systematic joints, which were not observed (Fig. 4.1).

iv. Broad, regional extension

Two distinct orientations of northwest-southeast and east-west-striking normal faults and systematic joints are present in fracture set 2 and are easily observable in the systematic joint data (Fig. 4.1). Thus two minimum compressive stress axes were calculated as northeast-southwest and north-south. Thus, a single, consistent, regional extension was not observed; however, it is possible that one or both of these orientations represent different regional extensions.

In order for both to be interpreted as due to regional extension the timing of the two fracture orientations would be expected to be resolvable and this was not the case. Both northwest-southeast and east-west-striking normal faults and systematic joints occur throughout Cambrian to Eocene units. No field observations of

cross-cutting or abutting relationships between these two orientations was observed, instead, these sets are isolated into spatial domains (Fig. 4.18). In addition, the modern stress field appears to also be consistent with these two orientations (Fig. 4.17) in which northwest-southeast-striking drilling-induced fractures are observed within the basin, and roughly north-south-trending extension may be limited to the basin-bounding arches as shown by the earthquake in the Granite Mountains.

Observations from the fracture data (Fig. 4.18) indicate that the two sets appear to have distinct spatial boundaries. For example, the outcrop data at Shoshoni Mesa strikes east-west whereas nearby subsurface data at Ocla Draw strikes more northerly. Further observations supporting two distinct orientations come from the Castle Gardens well, which shows both orientations and may straddle the approximate boundary of these domains. Here, the more westerly striking, smaller lobe of the rose diagram (Fig. 4.16) is composed of healed fractures whose mean depth is 1100 feet shallower than the mean depth of the northwest-southeast-striking open fractures. Some rotation spatially between these domains may be possible. At this time however, simply plotting the inferred σ_3 trends versus either the location's latitude or longitude does not adequately answer this question.

More data is needed to adequately test the hypothesis that there is no rotation in the stress field between the two orientations. In the western half of the basin, obtaining more data is difficult because the Wind River Reservation, home to Shoshoni and Arapahoe tribes, occupies the western half of the basin and access is restricted. The two stations obtained, WD1 and MC1, were located alongside state-maintained highways.

Roughly north-south-trending extension is observed along the northern and southern margins and northeast-southwest-trending extension is observed along the eastern and western margins of the basin and through the middle of the basin. Transecting the middle of the basin from east to west there does appear to be a slight westerly rotation, however this returns to a strong northwest-southeast in the western half of the basin (Fig. 4.18).

It appears that the northwest-southeast trending systematic joints are due to regional extension as they are found over such a wide area of Wyoming and Colorado (Hennings et al., 2000; Bergbauer & Pollard, 2004; Ruf & Erslev, 2005; Gillett et al., 2007; Cooley, 2009; C.L. Allen & L.E. Hamlin, 2009, personal communications) and these joints may be due to regional extension.

The presence of drilling-induced fractures that also strike northwest-southeast indicates a potentially long-lived regional

extension. This extension may be at least as old as the N34°W trending mid-Miocene mafic dikes in northwest Colorado (Thompson et al., 1989), indicating that the extension is more likely due to transtensional plate interactions in the Gulf of California along with Basin and Range extension which began in the Miocene (Bird, 2002) rather than epeirogenic uplift in the Pliocene (Keefer, 1970). Variation between the modern minimum compressive stress as determined from drilling and the minimum compressive stress that caused the non-induced fractures only varies by a mean 4° (Table A.5).

The east-west-striking normal faults and systematic joints however, may be coupled to extension associated with late Miocene or early Pliocene collapse of the Granite Mountains (Bauer, 1934; Scott, 2002). These fractures along the southern margin are almost certainly co-genetic with the graben associated with the down-dropping of the Granite Mountains. However, because of the swath of northwest-southeast trending fractures across the middle of the basin (Fig. 4.18), lack of east-west-striking fractures across the basin, and relative weakness of rocks in tension (Van Der Pluijm & Marshak, 2004), it is unlikely that the faulting and collapse on the southern margin caused the east-west-striking normal faults and systematic joints along the northern margin. Thus, the data herein does not support regional extension

as a cause for the east-west-striking normal faults and systematic joints. Instead, it appears that the farthest north this collapse influenced east-west-striking normal faults and systematic joints was at Muskrat Anticline, about 20 km into the basin (Fig. 4.18).

The east-west-striking normal fault (Hermann, 2009) which caused the earthquake in the Granite Mountains is consistent with the east-west-trending graben associated with the collapse of the Granite Mountains indicating that this area has been undergoing a long-lived localized extension.

v. Localized extension

A hypothesis for the east-west-striking normal faults and joints, especially those along the northern margin of the basin, is that they are due to localized extension that is coupled to unloading of Laramide arches along the basin margins during regional extension. This allowed their underlying thrust faults to backslide as listric normal faults and their margins to collapse.

To test this hypothesis, the 2θ vector mean for each location in set two was compared to the strike of the closest basin margin (Fig. 5.3, Table A.6). The 2θ vector mean, which is perpendicular to the inferred σ_3, was used so that the digitized data could be included.

The basin margin outline given (Fig. 4.18) follows major, basin-bounding faults such as the Owl Creek-Casper Arch Thrust, the

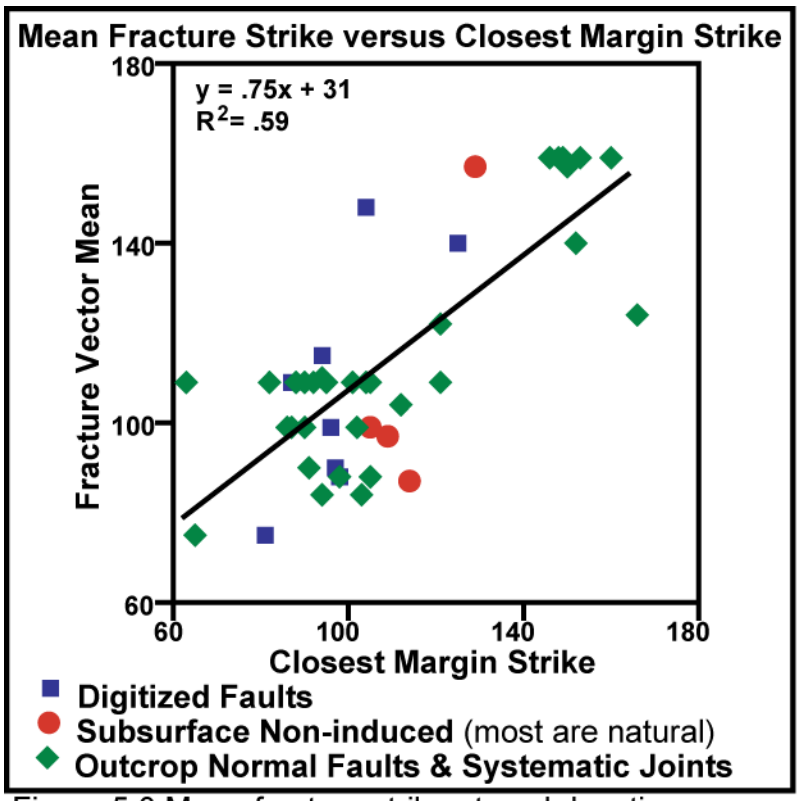

Figure 5.3 Mean fracture strike at each location versus closest margin strike, error bars are not given due to multiple sources of error including measuring in the field (~2° accuracy) and in calculating the inferred stress axes.

Cedar Ridge and North Granite Mountains normal faults, and blind faults associated with the anticlines on the western margin.

A triangle was used as an aid in measuring the mean strike of the basin margin. The apex of the triangle was placed at the data location with the acute bisector paralleling the shortest distance to the basin margin. Then, the mean strike was measured between where the sides of the triangle intersected the margin. For the digitized data, the approximate center of the domain (center of the

rose diagram, Fig. 3.1; 4.18) was used as the apex. This was done in order to smooth out minor variations in the strike of the margin.

The results (Fig. 5.3), thus obtained, show that a near one-to-one (slope of .75, R^2 value of .59), moderately high correlation exists between the mean fracture strike at each location and the strike of the closest basin margin. Also supporting this hypothesis are the east-west-striking normal faults in a 20 km zone into the basin along the Owl Creek Mountains and the hanging wall flat spots and reversal of fold vergence seen in seismic data. These observations all support the hypothesis of localized extension being due to the Laramide, thrust faults that underlie the basin-bounding arches having undergone post-Laramide backsliding and become normal faults (Fig 2.2) during arch collapse.

Structural Model

The final objective of this study was to build a structural model, consistent with seismic data, upon which future work, such as predicting zones of higher intensity fracturing, can be based.

The model (Fig. 5.4) proposes two potential mechanisms by which localized extension could be coupled to backsliding of listric thrust faults underlying the basin-bounding arches. In the first mechanism (Fig. 5.4A), major basin-bounding thrust faults backslide and induce a zone of tensional fracturing which may be similar to the 20 km zone of fracturing seen along the northern and

southern margins (Fig. 4.18). Normal faults in this zone likely sole into a bedding-parallel detachment, probably in a shale, which then merges into the main thrust. This mechanism is consistent with the observed faults with reverse senses of drag observed in the Wind River Canyon and the normal faults observed in the seismic data that do not propagate to great depth. Fracture intensity in this zone would be expected to be fairly consistent. The second possible mechanism (Fig. 5.4B) shows a smaller blind thrust fault, in which slip sense reversal causes the hanging wall fold to flatten and will eventually show reverse vergence, also consistent with the seismic data. Zones of higher intensity fracturing would likely occur at the edges of this flattening spot. Both mechanism appear to be active in the Wind River Basin.

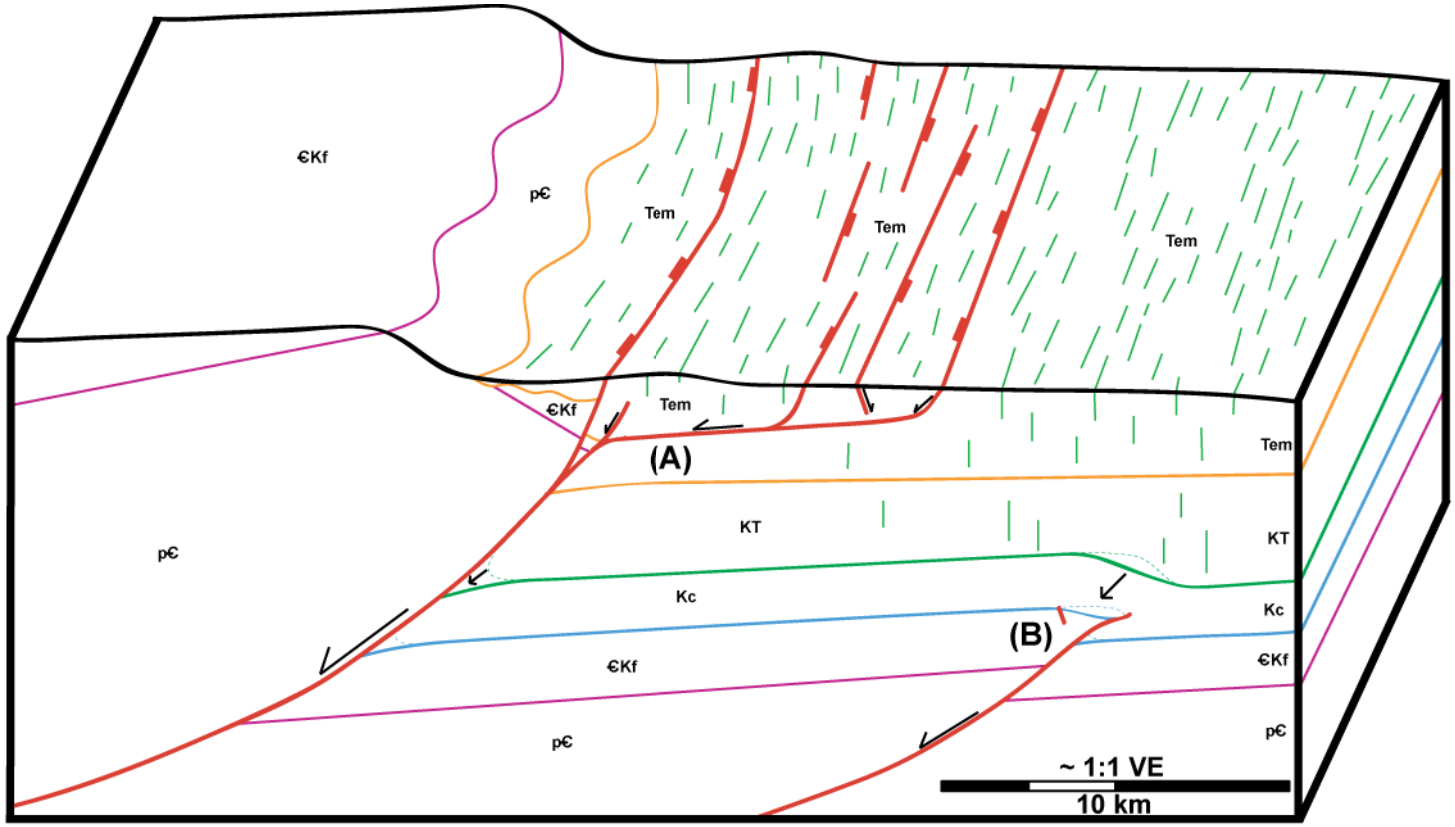

Figure 5.4 Schematic block diagram showing two possible mechanisms by which normal faulting (red lines) and jointing (short green lines) may occur due to backsliding. In (A), normal faults tie back to the main thrust fault along a bedding parallel detachment. (Note: the stratigraphic location of this detachment is unknown & may be lower in the section.) In this model normal faults can only form a certain distance from the main thrust and are surrounded by a halo of joints. In (B), fold vergence in the hangingwall & footwall of the thrust is flattened and finally reversed as the thrust becomes a listric normal fault. Antithetic normal faults and joints may form along the margins of the prior fold.

CHAPTER 6. CONCLUSIONS

In total, 10,941 outcrop and subsurface fractures and 1447 digitized fault strike segments were analyzed using eigenvector, ideal σ_1, and 2θ vector mean analyses to calculate the inferred axes of the stresses responsible for Phanerozoic deformation. These fractures were from units ranging from Precambrian to Miocene in age from across the Wind River Basin and included both major mapped faults and minor faults, and both open and healed joints. Timing relationships, ideal σ_1, and inferred σ_3 results based on bimodal clustering of the data (Fig. 4.4) indicate two distinct fracture sets.

In set 1, from strike-slip and thrust fault lineation data in Cambrian through lower Eocene units, a mean N66°E trending bedding-parallel maximum compressive stress was calculated using ideal σ_1 analysis (Fig. 4.8) and ranged from north-northeast to east-southeast. This is consistent with ENE-WSW Laramide horizontal compression (Molzer & Erlsev, 1995; Erslev & Koenig, 2009) calculated from similar fracture studies across the Rocky Mountains.

In set 2, northwest-southeast and east-west-striking normal faults and systematic joints were observed. N44°E and N7°E bedding-parallel minimum compressive stresses were calculated using eigenvector analysis of the fracture

geometries (Fig. 4.19). The fractures in this set were found in Cambrian through upper Eocene units.

The fractures in set 2 are present in the subsurface at depths up to 12,300 feet (Table A.5), indicating that they were not emplaced in the near-surface stress field, unlike the non-systematic joints which were only found in outcrop. Fractures in set two were not found in ENE-WSW or NNW-SSE orientations consistent with Laramide shortening, later elastic strain release, or east-west left-slip faulting. Thus, the fractures in set two are likely post-Laramide.

Northwest-southeast-striking normal faults and systematic joints are found across the region, on the eastern and western margins of the basin, and in a swath through the middle of the basin. They are consistent with the modern stress within the basin as determined from northwest-southeast-striking drilling-induced fractures and northeast-southwest borehole breakouts (Fig. 4.17). The calculated N44°E trending, bedding-parallel minimum compressive stress from these fractures may be due to far field stresses caused by transtensional plate interactions in the Gulf of California along with Basin and Range extension which began in the Miocene (Bird, 2002) and may be at least as old as the mid-Miocene mafic dikes with the same trend in northwest Colorado (Thompson et al., 1989).

East-west-striking normal faults and systematic joints are found in a 20 km zone along the northern and southern margins of the basin (Fig. 4.18) in units that are younger than Laramide tilting. The recent earthquake in the Granite Mountains is consistent with the range of values calculated for the minimum

compressive stress. The calculated N7°E trending, bedding-parallel minimum compressive stress from these fractures is likely co-genetic with the late Miocene or early Pliocene collapse of the Granite Mountains along the southern margin of the basin (Bauer, 1934; Scott, 2002) and likely continues to the present. Along the northern margin of the basin, these fractures are even more variable than along the southern margin, and closely parallel the Owl Creek-Casper Arch Thrust fault (Fig. 4.18; 5.3). This parallelism supports the hypothesis that backsliding occurred on this thrust system and is supported by seismic data showing fold flattening and vergence reversal. Backsliding is likely responsible for the Cedar Ridge Normal Fault and other normal faults, down-dropped blocks, and normal faults and systematic joints present in the hanging wall and basin footwall of this thrust.

The backsliding of the Owl Creek Thrust and late Miocene or early Pliocene collapse of the Granite Mountains, are likely contemporaneous and driven by the regional extension. It is likely that in the Rocky Mountains, post-Laramide orogenic collapse has occurred during regional extension and has unloaded these Laramide arches, allowing their underlying thrust faults to backslide as listric normal faults and their margins to collapse, creating zones of localized fracturing and extension.

This backsliding model (Fig. 5.4) may be critically important in predicting subsurface fracture intensity and fluid migration pathways, with broad implications for hydrocarbon recovery, especially in fractured plays within the basin such as Frenchie Draw.

Future Work

There is an abundance of industry data which could be used to test and refine these conclusions. Sources of additional micro-resistivity image log data include additional wells not included in this study and intervals from older stratigraphic units. Micro-resistivity image logs from horizontal wells would give data on fracture spacing. Additional data could also come from anisotropy data acquired from sonic logs and 3D seismic.

Additional outcrop data from the anticlines along the southern margin of the basin would be valuable as well. Joints and normal faults in these older units may be consistent with Laramide shortening and may have very different orientations, giving additional support to the interpretation that the fractures in set 2 are post-Laramide.

Potential exists for determining fracture intensity from fracture data used in this study as well as from seismic anisotropy data. These models could be as simple as a single cross section, with rheologic units similar to the stratigraphic groups defined in this study that could be used to model strain intensities for a blind thrust fault reversing its sense of movement as a listric normal fault. Also, a more complex 3D model, based on the actual unit and fault surfaces mapped from seismic data across the basin, could be used to model strain and fracture intensities.

Future work could also include looking for similarly-localized fracturing along other Laramide arch margins. This would further test the hypothesis of post-Laramide, regional orogenic collapse inducing localized backsliding.

REFERENCES

Allmendinger, R.W., 2005, Stereonet 6.3.3: Cornell University, Ithaca, New York.

Angelier, J., 1984, Tectonic analysis of fault slip data sets: Journal of Geophysical Research, v. 89, no. B7, p. 5835-5848.

Angelier, J., 1990, Inversion of field data in fault tectonics to obtain the regional stress—III. A new rapid direct inversion method by analytical means: Geophysical Journal International, v. 103, no. 2, p. 363-376.

Barnes, J. W., and R. J. Lisle, 2004, Basic Geological Mapping: Chichester, England, John Wiley & Sons, Ltd, 184 p.

Bauer, C.M., 1934, Wind River Basin: GSA Bulletin, v. 45, no. 4, p. 665-696.

Bergbauer, S., and D.D. Pollard, 2004, A new conceptual fold-fracture model including prefolding joints, based on the Emigrant Gap anticline, Wyoming: GSA Bulletin, v. 116, no. 3/4, p. 294-307.

Bergh, S.G., and A.W. Snoke, 1992, Polyphase Laramide deformation in the Shirley Mountains, south-central Wyoming foreland: The Mountain Geologist, v. 29, no. 3, p. 85-100.

Bird, P., 2002, Stress direction history of the western United States and Mexico since 85 Ma: Tectonics, v. 21, no. 3, p. 1014-1025.

Blackstone, D.L., Jr., 1993, Precambrian basement map of Wyoming: outcrop and structural configuration, in Schmidt, C.J., R.B. Chase, & E.A. Erslev, eds., Laramide basement deformation in the Rocky Mountain foreland of the western United States: GSA Special Paper 280, p. 335-337.

Brocka, C., 2005, Fracture analysis across Derby and Dallas Domes, west-central Wyoming: Implications for the history of hydrocarbon migration along bleached fracture sets: AAPG Search and Discovery Article, no. 90045.

Brown, W.G., 1988, Deformation style of Laramide uplifts in the Wyoming foreland, in Schmidt, C.J., & W.J. Perry, Jr., eds., Interaction of the Rocky Mountain foreland and the Cordilleran thrust belt: GSA Memoir 171, p. 1-25.

Brown, W.G., 1993, Structural style of Laramide basement-cored uplifts and associated folds, in Snoke, A.W., J.R. Steidtmann, S.M. Roberts, eds., Geology of Wyoming: Geological Survey of Wyoming Memoir No. 5, p. 312-373.

Burg, J.-P., M.N. Chaudhry, M. Ghazanfar, R. Anczkiewicz, and D. Spencer, 1996, Structural evidence for back sliding of the Kohistan arc in the collisional system of northwest Pakistan: Geology, v. 24, no. 8, p. 739-742.

Chamberlain, K.R., C.D. Frost, & R. Frost, 2003, Early Archean to Mesoproterozoic evolution of the Wyoming Province: Archean origins to modern lithospheric architecture: Canadian Journal of Earth Science, v. 40, p. 1357-1374.

Clift, P.D., J.F. Dewey, A.E. Draut, D.M. Chew, M. Mange, and P.D. Ryan, 2004, Rapid tectonic exhumation, detachment faulting and orogenic collapse in the Caledonides of western Ireland: Tectonophysics, v. 384, no. 1-4, p. 91-113.

Compton, R.R., 1966, Analysis of Pliocene-Pleistocene deformation and stresses in Northern Santa Lucia Range, California: GSA Bulletin, v. 77, no. 12, p. 1361-1380.

Constenius, K.N., 1996, Late Paleogene extensional collapse of the Cordilleran fold and thrust belt: GSA Bulletin, v. 108, no. 1, p. 20-39.

Cooley, R.D., 2009, Structural, lithological, and regional tectonic controls on P-wave azimuthal anisotropy: Casper Arch area, Wyoming: Master's Thesis, Colorado State University, Fort Collins, Colorado, 140 p.

Dickinson, W.R., M.A. Klute, M.J. Hayes, S.U. Janecke, E.R. Lundin, M.A. McKittrick, and M.D. Olivares, 1988, Paleogeographic and paleotectonic setting of Laramide sedimentary basins in the Rocky Mountain region; GSA Bulletin, v. 100, no. 7, p. 1023-1039.

Edwards, M.A., and T.M. Harrison, 1997, When did the roof collapse? Late Miocene north-south extension in the high Himalaya revealed by Th-Pb monazite dating of Khula Kangri granite: Geology, v. 25, no. 6, p. 543-546.

Erslev, E.A., 1991, Trishear fault-propagation folding: Geology, v. 19, no. 6, p. 617-620

Erslev, E.A., 1995, CALINE: Colorado State University, Fort Collins, Colorado.

Erslev, E.A., 1998a, LDIS 2: Colorado State University, Fort Collins, Colorado.

Erslev, E.A., 1998b, SELECT 1.2: Colorado State University, Fort Collins, Colorado.

Erslev, E.A., S.M. Holdaway, S.A O'Meara, B. Jurista, and B. Selvig, 2004, Laramide minor faulting in the Colorado Front Range: NM Bureau of Geology & Mineral Resources Bulletin 160, p. 181-203.

Erslev, E.A., 2005, 2D Laramide geometries and kinematics of the Rocky Mountains, Western U.S.A.: in Karlstrom, K.E. and G.R. Keller, eds., The Rocky Mountain Region – An Evolving Lithosphere: Tectonics, Geochemistry, and Geophysics: AGU Geophysical Monograph 154, p. 7-20.

Erslev, E.A., and S.M. Larson, 2006, Testing Laramide hypotheses for the Colorado Front Range arch using minor faults: The Mountain Geologist, v. 43, no. 1, p. 45-64.

Erslev, E.A., 2009, Integrated fracture analysis: an important tool for deciphering complex fracture patterns: AAPG Search and Discovery Article, no. 90090.

Erslev, E.A., and N.V. Koenig, 2009, 3D kinematics of Laramide, basement-involved Rocky Mountain deformation U.S.A.: Insights from minor faults and GIS-enhanced structure maps: in Kay, S., V. Ramos, and W.R. Dickinson, eds., Backbone of the Americas: Shallow subduction, plateau uplift and ridge and terrain collision, GSA Memoir 204, p. 125-150.

Fanshawe, J.R., 1939, Structural geology of the Wind River Canyon area, Wyoming: AAPG Bulletin, v. 23, no. 10, p. 1439-1492.

Fossen, H., 2000, Extensional tectonics in the Caledonides: synorogenic or postorogenic?: Tectonics, v. 19, no. 2, p. 213-224.

Fox, J.E., and G.L. Dolton, 1995, Wind River Basin Province (035): in Gautier, D.L., G.L. Dolton, K.I. Takashashi, and K.L. Varnes, eds., National assessment of United States oil and gas resources—results, methodology, and supporting data: U.S. Geological Survey Digital Data Series DDS-30, 21 p.

Gillett, C., 2009, Mechanisms of fracturing in northwestern Colorado: multi-stage deformation and the importance of post-Laramide extension: Master's Thesis, Colorado State University, Fort Collins, Colorado, 140 p.

Gillett, C., J. Detring, and E.A. Erslev, 2007, Fracture genesis in northwest Colorado: determining fracture timing and its importance to regional tectonics and fractured reservoirs, in New Structural Concepts and Applications in Rocky Mountain Hydrocarbon Plays: RMAG/PTTC Fall Symposium.

Gower, M.A., 1978, Catalog of Paleozoic, Mesozoic, and Cenozoic rock names for the Wind River Basin: Wyoming Geological Association 30th Annual Field Conference Guidebook, p. 39-45.

Gries, R., 1983, North-south compression of Rocky Mountain foreland structures: in Lowell, J.D., ed., Rocky Mountain foreland basins and uplifts: RMAG Guidebook, p. 9-32.

Hall, M.K., and C.G. Chase, 1989, Uplift, unbuckling, and collapse: flexural history and isostasy of the Wind River Range and Granite Mountains,

Wyoming: Journal of Geophysical Research, v. 94, no. B12, p. 17,581-17,593.

Hausel, W.D., P.J. Graff, K.G. Alvert, 1985, Economic geology of the Copper Mountain supracrustal belt, Owl Creek Mountains, Fremont County, Wyoming: Geological Survey of Wyoming, Report of Investigations No. 28.

Hausel, W.D., and W. Sutherland, 2003, Rattlesnake Hills 30' X 60' Quadrangle, Fremont and Natrona Counties, Wyoming: Wyoming Geological Survey Map Series 61, 1:100,000, 1 sheet.

Heidbach, O., M. Tingay, A. Barth, J. Reinecker, D. Kurfeß, and B. Müller, 2008, The World Stress Map database.

Hennings, P.H., J.E. Olson, and L.B. Thompson, 2000, Combining outcrop data and three-dimensional structural models to characterize fractured reservoirs: an example from Wyoming: AAPG Bulletin, v. 84, no. 6, p. 830-849.

Hermann, B., 2009, Fault plane solution calculations, <http://www.eas.slu.edu/Earthquake_Center/MECH.NA/20090517064518/index.html> Accessed June 8, 2009.

Jones, C.T., 1939, Geology of the Wind River Canyon, Wyoming: AAPG Bulletin, v. 23, no. 4, p. 476-491.

Keefer, W.R., 1965, Geologic history of the Wind River Basin, central Wyoming: AAPG Bulletin, v. 43, no. 11, p. 1878-1892.

Keefer, W.R., 1970, Structural geology of the Wind River Basin, Wyoming: Washington, United States Geological Survey, 35 p.

Krumbein, W.C., 1939, Preferred orientation of pebbles in sedimentary deposits: The Journal of Geology, v. 47, no. 7, p. 673-706.

Love, J.D., A.C. Christiansen, J.L. Earle, and R.W. Jones , 1978, Preliminary Geologic Map of the Arminto 1° x 2° Quadrangle, Central Wyoming: U.S. Geological Survey Open-File Report 78-1089, 1:250,000, 1 sheet.

Love, J.D., A.C. Christiansen, T.M. Brown, and J.L. Earle, 1979, Preliminary Geologic Map of the Thermopolis 1° x 2° Quadrangle, Central Wyoming: U.S. Geological Survey Open-File Report 79-962, 1:250,000, 1 sheet.

Love, J.D., and A.C. Christiansen, 1985, Geologic Map of Wyoming: Reston, Virginia, U.S. Geological Survey, 1:500,000, 1 sheet.

Machette, M.N., 1999, Quaternary fault and fold database of the United States: U.S. Geological Survey.

Markshak, S., and G. Mitra, 1988, Basic Methods of Structural Geology: Englewood Cliffs, New Jersey, Prentice Hall, 446 p.

Means, W.D., 1987, A newly recognized type of slickenside striation: Journal of Structural Geology, v. 9, no. 5/6, p. 585-590.

Molzer, P.C., 1993, Oblique slip in Laramide foreland arches: Master's Thesis, Colorado State University, Fort Collins, Colorado, 156 p.

Molzer, P.C., and E.A. Erslev, 1995, Oblique convergence during northeast-southwest Laramide compression along the east-west Owl Creek and Casper Mountain arches, Central Wyoming: AAPG Bulletin, v. 79, no. 9, p. 1377-1394.

Mueller, C., 1989, Frenchie Draw, in Bighorn and Wind River Basins: Wyoming Oil and Gas Fields Symposium, p. 174-175.

Nilsen, T.H., and A.G. Sylvester, 1995, Strike-slip basins, in Busby, C.J., and R.V. Ingersoll, eds., Tectonics of sedimentary basins: Cambridge, Massachusetts, Blackwell Science, p. 425-457.

Normark, R.M., 1978, Frenchie Draw Gas Field, in Resources of the Wind River Basin: WGA 30th Annual Field Guide Conference Guidebook, p. 277-280.

Paylor, E.D., II and A. Yin, 1993, Left-slip evolution of the north Owl Creek fault system, Wyoming, during Laramide shortening, in Schmidt, C.J., R.B. Chase, and E.A. Erslev, eds., Laramide basement deformation in the Rocky Mountain foreland of the western United States: GSA Special Paper 280, p. 229-242.

Petit, J.P., 1987, Criteria for the sense of movement on fault surfaces in brittle rocks: Journal of Structural Geology, v. 9, no. 5/6, p. 597-608.

Rackley, R.I., 1972, Environment of Wyoming Tertiary uranium deposits: AAPG Bulletin, v. 56, no. 4, p. 755-774.

Ruf, J.C., and E.A. Erslev, 2005, Origin of Cretaceous to Holocene fractures in the northern San Juan Basin, Colorado and New Mexico: Rocky Mountain Geology, v. 40, no. 1, p. 94-114.

Sava, D., and G. Mavko, 2007, Rock physics-based integration of geologic and geophysical data for fracture characterization, The Leading Edge, v. 26, no. 9, p. 1140-1146.

Scott, J.W., 2002, The Upper Miocene Moonstone Formation of central Wyoming: Linking vertebrate biostratigraphy and U-Pb geochronology with post-Laramide tectonism, in Tectonics, Climate Change, and the Late Cenozoic Evolution of the Rocky Mountains, Colorado Plateau, and Western Great Plains: GSA Annual Meeting.

Stearns, D.W., 1978, Faulting and forced folding in the Rocky Mountains foreland, in Matthews, V., III, ed., GSA Memoir 151, p. 1-37.

Steidtmann, J.R., 1993, The Cretaceous foreland basin and its sedimentary record, in Snoke, A.W., J.R. Steidtmann, and S.M. Roberts, eds., Geology of Wyoming: Geological Survey of Wyoming Memoir 5, p. 25-271.

Stone, D.S., 2007, The wrench fault concept – revisited and fortified by modern seismic evidence, in New Structural Concepts and Applications in Rocky Mountain Hydrocarbon Plays: RMAG/PTTC Fall Symposium.

Thaden, R.E., 1978, Geologic Map of the Bonneville Quadrangle, Fremont County, Wyoming: Reston, Virginia, U.S. Geological Survey GQ-1439, 1:24,000, 1 sheet.

Thaden, R.E., 1980a, Geologic Map of the Birdseye Pass Quadrangle, Showing Chromolithofacies and Coal Beds in the Wind River Formation, Fremont and Hot Springs Counties, Wyoming: Reston, Virginia, U.S. Geological Survey GQ-1537, 1:24,000, 1 sheet.

Thaden, R.E., 1980b, Geologic Map of the Picard Ranch Quadrangle, Showing Chromolithofacies and Coal Beds in the Wind River Formation, Fremont

County, Wyoming: Reston, Virginia, U.S. Geological Survey GQ-1539, 1:24,000, 1 sheet.

Thaden, R.E., 1980c, Geologic Map of the Guffy Peak Quadrangle, Showing Chromolithofacies and Coal Beds in the Wind River Formation, Fremont and Hot Springs Counties, Wyoming: Reston, Virginia, U.S. Geological Survey GQ-1527, 1:24,000, 1 sheet.

Thompson, R.N., P.T. Leat, A.P. Dickin, M.A. Morrison, G.L. Hendry, S.A. Gibson, 1989, Strongly potassic mafic magmas from lithospheric mantle sources during continental extension and heating: evidence from Miocene minettes of northwest Colorado, U.S.A.: Earth and Planetary Science Letters, v. 98, no. 2, p. 139-153.

Thompson, R.C., 2006, Stratigraphy & sedimentology of a Hadrosaur bone bed in the Lance Formation, Eastern Wyoming; mapped using GPS and GIS: Senior Thesis, Southwestern Adventist University, Keene, Texas, 15 p.

Thompson, R.C., and E.A. Erslev, 2009, Two-stage mechanical stratigraphy and extensional fracturing in the Wind River Basin, Wyoming: AAPG Search and Discovery Article, no. 90090.

USBM, 1990, Availability of Federally Owned Minerals for Exploration and Development in the Western United States: Denver, U.S. Bureau of Mines, 1:500,000.

Van Der Pluijm, B.A., and S. Marshak, 2004, Earth Structure, 2nd ed.: New York, New York, W. W. Norton & Company, Inc., 656 p.

Varga, R.J., 1993, Rocky Mountain foreland uplifts: products of a rotating stress field or strain partitioning?: Geology, v. 21, no. 12, p. 1115-1118.

Whitehead, N.H., III, 1997, Fractures at the surface, San Juan Basin, New Mexico and Colorado, in Hoak, T.E., A.L. Klatwitter, and P.K. Bloomquist, eds., Fractured reservoirs: Characterization and modeling: RMAG Guidebook, p. 27-39.

Wise, D.U., 1963, Keystone faulting and gravity sliding driven by basement uplift of Owl Creek Mountains, Wyoming: AAPG Bulletin, v. 47, no. 4, p. 586-598.

Zeilinger, G., D. Seward, and J.-P. Burg, 2007, Exhumation across the Indus Suture Zone: a record of back sliding of the hanging wall: Terra Nova, v. 19, no. 6, p. 425-437.

APPENDIX

Abbreviations for the outcrop stations, wells sites, digitized domains, and earthquake location

BC: Badwater Creek; BI: Birdseye Inlier; BR: Boysen Reservoir; CCA: Conant Creek Anticline; CG: Castle Gardens; CR: Cedar Ridge; DA: Dutton Anticline; FD: Frenchie Draw; FR: Fuller Reservoir; HHA: Hell's Half Acre; MA: Muskrat Anticline; MC: Muddy Creek; OD: Ocla Draw; RHQ: Rattlesnake Hills Quadrangle; SGME: South Granite Mountains Earthquake; SH: Steffen Hill; SM: Shoshoni Mesa; W: Waltman; WD: Winkleman Dome; WRC: Wind River Canyon; WSM: World Stress Map; WWRB: Western Wind River Basin

Codes for the type of fractures

J_s: systematic joint; J_{ns}: non-systematic joint; SS: strike-slip fault, either right-slip (RS) or left-slip (LS); TF: thrust fault; NF: normal fault (1 for the conjugate whose poles plot in the south and west quadrants and 2 for the conjugate whose poles plot in the north and east quadrants); I: drilling induced: NI: non-induced (natural)

Planes given in strike-dip (dip clockwise of strike), lineations and E_n vector in trend-plunge E_n value in (). Formation key in Fig 2.2

Table A.1 Summary of outcrop data by station

Abbreviations on page 1 of appendix

Station	Fm	Bedding	n	J_s	J_{ns}	NF	SS	TF	Latitude	Longitude
BC1	T_{wdr}	242-2	44			44			43.31	-107.95
BC2	T_{wdr}	70-10	26			26			43.34	-107.82
BC3	T_{wdr}	275-7	26	26					43.36	-107.54
BC4	T_{wdr}	314-4	11	11					43.25	-107.69
BI1	C_f	286-37	19			16	3		43.41	-108.06
BR1	T_{wdr}	325-8	46	46					43.32	-108.15
BR2	T_{wdr}	~flat	65			65			43.28	-108.2
BR3	T_{wdr}	228-2	30			30			43.23	-108.15
CCA1	T_{Rc}	334-38	83					83	42.8	-108.05
DA1	T_{fu}	215-7	26					26	42.96	-107.69
DA2	T_{wdr}	322-7	48	48					42.84	-107.6
DA3	J_n	137-16	43	43					42.84	-107.6
DA4	K_{cl}	128-32	14				14		42.83	-107.6
FD1	T_{wdr}	279-16	10	10					43.2	-107.55
HHA1	K_l	148-72	72	48	24				43.04	-107.09
HHA2	K_l	154-67	57					57	43.04	-107.09
HHA3	K_l	150-67	42	26	16				43.04	-107.08
HHA4	T_{wdr}	140-18	176	49	72	55			43.04	-107.09
HHA5	T_{wdr}	148-24	69	51	18				43.04	-107.09
HHA6	T_{wdr}	149-19	58	37	21				43.04	-107.09
HHA7	T_{wdr}	163-21	27					27	43.04	-107.09
MA1	K_l	265-12	95			71		24	42.91	-107.88
MA2	K_l	folded	30	30					42.92	-107.88
MA3	T_{fu}	149-12	16			16			42.93	-107.9
MC1	T_{wdr}	~flat	8	8					43.27	-108.46
SH1	C_f	80-40	70			48	13	9	43.37	-107.9
SH2	T_{wb}	105-8	12	12					43.36	-107.89
SM1	T_{wdr}	294-2	56			56			43.23	-107.98
W1	T_{fu}	113-52	31	20				11	43.09	-107.17
W2	T_{fu}	348-82*	17	8				9	43.13	-107.21
WD1	T_{wdr}	350-1	53	28	25				43.21	-108.97
WRC1	C_f	226-11	11				11		43.46	-108.17
WRC2	C_{gv}	~flat	40	9				31	43.43	-108.17
WRC3	C_{gv}	216-29	11				5	6	43.43	-108.18
WRC4	C_f	95-3	46			44	2		43.42	-108.18
WRC5	C_f	194-11	94			47	24	23	43.42	-108.18
WRC6	C_f	297-13	43			16	3	24	43.42	-108.18
WRC7	C_{gv}	220-4	4			4			43.42	-108.18
WRC8	C_g	109-18	58	36	14	8			43.41	-108.17
WRC9	T_{Rc}	245-4	81	25	15		41		43.4	-108.17
WRC10	T_{Rc}	125-29	46	46					43.4	-108.17
WRC11	P_t	116-59	19				19		43.4	-108.14

*overturned

Table A.2 Strike-slip & thrust fault average conjugate planes & their eigen analysis Abbreviations on page 1 of appendix, mean 2α is 17°

Station	RS	LS	E_1	E_2	E_3
BI1	225-53	83-64	155-6 (.65)	**54-62 (.35)**	248-28 (.00)
DA4	17-85	237-81	127-2 (.87)	**218-20 (.13)**	31-70 (.00)
SH1	259-89	280-77	179-7 (.96)	**274-30 (.04)**	77-59 (.00)
WRC1	77-83	280-81	179-1 (.94)	**269-35 (.06)**	87-55 (.00)
WRC5	58-88	260-85	159-2 (.96)	**250-19 (.04)**	64-72 (.00)
WRC9	37-76	80-77	329-15 (.87)	**238-1 (.13)**	143-76 (.00)
WRC11	23-87	64-60	312-18 (.84)	**54-34 (.16)**	199-51 (.00)
Mean	**228-90**	**81-85**	335-3 (.92)	**65-9 (.08)**	228-81 (.00)
Station	**TF1**	**TF2**	E_1	E_2	E_3
CCA1	351-23	168-23	350-89 (.85)	**80-0 (.15)**	170-1 (.00)
DA1	340-22	182-25	154-85 (.85)	**262-2 (.15)**	352-5 (.00)
HHA2	320-20	175-24	142-83 (.87)	**249-2 (.13)**	339-7 (.00)
HHA7	359-18	192-11	250-86 (.94)	**94-4 (.06)**	4-2 (.00)
MA1	316-32	141-12	223-80 (.86)	**47-10 (.14)**	317-1 (.00)
SH1	332-24	195-10	219-81 (.92)	**75-7 (.08)**	344-5 (.00)
W1	293-20	132-16	166-87 (.91)	**34-2 (.09)**	304-2 (.00)
W2	34-46	111-45	342-52 (.80)	**73-1 (.20)**	164-39 (.00)
WRC2	315-14	174-19	132-84 (.93)	**248-3 (.07)**	338-6 (.00)
WRC3	318-26	48-22	269-73 (.92)	**8-3 (.08)**	98-17 (.00)
WRC5	299-26	118-13	210-84 (.89)	**29-7 (.11)**	119-0 (.00)
WRC6	290-17	100-6	206-84 (.96)	**17-6 (.04)**	107-1 (.00)
Mean	**329-21**	**147-14**	243-87 (.91)	**58-4 (.09)**	148-0 (.00)

Table A.3 Systematic joint average planes & their eigen analysis

Abbreviations on page 1 of appendix

Station	J_s	E_1
BC3	94-82	**4-8 (.98)**
BC4	271-81	**181-9 (.90)**
BR1	104-85	**14-5 (.95)**
DA2	278-86	**188-4 (.94)**
DA3	106-88	**16-2 (.93)**
FD1	330-76	**240-14 (.93)**
HHA1	328-87	**238-3 (.96)**
HHA3	329-80	**239-10 (.96)**
HHA4	342-84	**252-6 (.89)**
HHA5	326-78	**236-12 (.95)**
HHA6	334-80	**244-10 (.95)**
MA2	137-78	**47-12 (.88)**
MC1	292-89	**202-1 (.94)**
SH2	102-77	**12-13 (.92)**
W1	301-79	**211-11 (.96)**
W2	166-84	**76-6 (.96)**
WD1	152-84	**62-6 (.90)**
WRC2	96-86	**6-4 (.93)**
WRC8	105-87	**15-3 (.96)**
WRC9	90-79	**360-11 (.93)**
WRC10	285-77	**195-13 (.97)**

Table A.4 Normal fault average conjugate planes (P) & lineations (L) & their eigen analysis Abbreviations on page 1 of appendix, mean 2α is 27°

Station	NF1(P)	NF2(P)	E_1	E_2	E_3
BC1	264-56	87-47	**355-4 (.60)**	149-85 (.40)	265-2 (.00)
BC2	243-54	71-58	**157-2 (.68)**	48-84 (.32)	247-6 (.00)
BI1	320-72	131-76	**216-1 (.88)**	309-73 (.12)	126-17 (.00)
BR2	269-55	88-53	**359-1 (.65)**	213-89 (.35)	89-1 (.00)
BR3	271-57	93-54	**2-2 (.66)**	150-88 (.34)	272-1 (.00)
HHA4	353-65	154-42	**75-12 (.63)**	302-73 (.37)	167-12 (.00)
MA1	247-74	94-75	**184-1 (.93)**	4-90 (.07)	274-0 (.00)
MA3	284-65	102-62	**13-2 (.80)**	246-88 (.20)	103-2 (.00)
SH1	267-65	89-80	**178-8 (.90)**	21-82 (.10)	269-3 (.00)
SM1	269-60	92-62	**181-1 (.76)**	70-87 (.24)	271-3 (.00)
WRC4	249-78	59-50	**335-14 (.80)**	190-73 (.20)	67-9 (.00)
WRC5	259-53	83-76	**171-12 (.81)**	11-79 (.19)	262-4 (.00)
WRC6	282-62	100-56	**11-3 (.73)**	220-87 (.27)	101-2 (.00)
WRC7	277-79	67-82	**172-2 (.91)**	263-33 (.09)	80-57 (.00)
WRC8	284-78	96-85	**190-4 (.97)**	287-65 (.03)	98-25 (.00)
Mean	**271-63**	**91-63**	**181-0 (.79)**	90-90 (.21)	271-0 (.00)
Station	**NF1(L)**	**NF2(L)**	E_1	E_2	E_3
BC2	353-45	152-64	21-78 (.67)	**165-10 (.33)**	256-7 (.00)
HHA4	108-57	239-45	189-71 (.67)	**80-7 (.33)**	348-18 (.00)
MA1	328-63	175-77	306-82 (.89)	**157-7 (.11)**	66-4 (.00)
SH1	342-66	192-82	328-81 (.93)	**170-8 (.07)**	79-3 (.00)
SM1	358-66	200-65	273-85 (.83)	**9-1 (.17)**	99-5 (.00)
WRC4	325-78	155-50	160-76 (.81)	**333-14 (.19)**	63-2 (.00)
WRC5	335-53	217-68	297-73 (.82)	**178-9 (.18)**	86-15 (.00)
WRC6	38-54	202-55	81-82 (.59)	**210-5 (.41)**	301-6 (.00)
Mean	**356-66**	**193-67**	282-86 (.84)	**184-1 (.16)**	94-4 (.00)

Table A.5 Summary of subsurface data by well & their eigen analysis

Abbreviations on page 1 of appendix

Well	Fm	Depth (ft)*	beds	Bedding	I	E_1	NI	E_1 value	E_1
FD.1	T_{fu}	7280	6	137-9 (.98)	17	**213-1 (.92)**	113	0.64	**30-0 (.64)**
FD.2	T_{fu}	6695			34	**211-1 (.95)**	140	0.46	**28-26 (.95)**
FD.3	T_{fu}	6680			3	**37-7 (.99)**	218	0.59	**210-2 (.59)**
FD.4	T_{fu}	7537	1856	270-4 (.99)	174	**44-0 (.94)**	209	0.77	**37-2 (.77)**
FD.5	T_{fu}	8752	2087	270-4 (.99)	898	**221-2 (.94)**	489	0.54	**214-0 (.54)**
FD.6	T_{fu}	8123	1521	273-1 (.99)	81	**30[2]-2 (.95)**	176	0.85	**31-4 (.85)**
FD.7	T_{fu}	6783			129	**215-4 (.92)**	68	0.53	221-6[3] **(.53)**
FD.8	T_{fu}	7137			75	**33-0 (.96)**	82	0.83	**221-2 (.83)**
FD.9	T_{fu}	7257	776	326-1 (.99)	165	**48-5 (.93)**	153	0.88	**51-7 (.88)**
FD.10	T_{fu}	7290	1747	9-1 (1.00)	139	**52-3 (.93)**	200	0.85	**47-12 (.85)**
FD.11	T_{fu}	7136	966	293-3 (.99)	205	**228-3 (.89)**	364	0.68	**226-6 (.68)**
FD.12	T_{fu}	7376	1079	26-2 (.99)	155	**46-4 (.91)**	136	0.68	**35-12 (.68)**
FD.13	T_{fu}	6783	4204	333-3 (.99)	267	**52-6 (.91)**	337	0.54	**46-5 (54)**
FD.14	T_{fu}	7480	1244	266-2 (.99)	167	**45-1 (.97)**	191	0.72	**40-1 (.72)**
FD.15	T_{fu}	6783			195	**46-2 (.96)**	551	0.57	**49-4 (.57)**
FD.16	T_{fu}	9842	2420	264-4 (.96)	226	**43-1 (.94)**	137	0.67	**25-7 (.67)**
FD.17	T_{fu}	11147	251	310-3 (.95)	27	**30-0 (.91)**	43	0.81	**20-3 (.81)**
FD.18	T_{fu}	8316			15	**27-2 (.86)**	89	0.75	**205-3 (.75)**
FD.19	T_{fu}	7611	1569	272-4 (1.00)	290	**226-0 (.92)**	373	0.78	**224-3 (.78)**
FD.20	T_{fu}	7457	1	206-11	28	**220-1 (.97)**	64	0.85	**226-1 (.85)**
OD.1	T_{fu}	7433	2116	310-2 (.99)	211	**209-3 (.93)**	1090	0.76	**199-5 (.76)**
FR.1	T_{fu}	6593	1532	329-9 (.98)	31	**26[2]-4 (.96)**	137	0.78	**196-3 (.78)**
CG.1	K_c	4060	3069	344-3 (1.00)	13	**206-6 (.97)**	202	0.64	**204-24 (.64**
All		**7459**	**26444**	**302-2 (1.00)**	**3545**	**39-1 (.97)**	**5562**	**0.95**	**35-1 (.95)**

*Average fracture depth over logged interval

[2]90° from E_1 trend (borehole breakout)

[3]E_2 vector

Table A.6 Extensional fracture vector mean & basin-bounding fault strike Abbreviations on page 1 of appendix

Station	Vector Mean	Strike
BC1	86	279
BC2	65	255
BC3	274	290
BC4	271	270
BI1	301	289
BR1	284	289
BR2	88	289
BR3	272	289
DA2	278	268
DA3	285	268
FD1	330	337
HHA1	328	339
HHA3	329	339
HHA4	340	339
HHA5	326	339
HHA6	333	339
MA1	274	264
MA3	283	264
MC1	292	284
SH1	87	279
SH2	282	279
SM1	270	279
W1	301	302
W2	346	304
WD1	332	320
WRC2	275	289
WRC4	63	289
WRC5	82	289
WRC6	281	289
WRC7	82	289
WRC8	284	289
WRC9	90	289
WRC10	285	289

Domain	Vector Mean	Strike
BH1	274	295
BH2	284	328
BM1	87	289
BM2	81	255
BM3	277	270
CR	276	279
BC	276	279
RHQ	278	268
WWRB	305	320

Field	Vector Mean	Strike
FD	309	337
OD	289	277
FR	285	279
CG	294	267

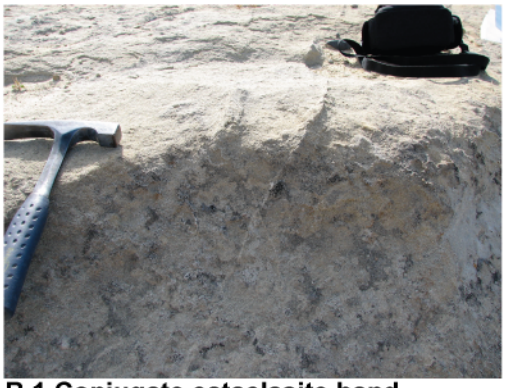

B.1 Conjugate cataclasite band, Wind River Formation, Station BR2.

B.2 Conjugate fractures, Great Horned Owl is acute bisector, Wind River Formation, Station MA1.

B.3 Normal fault surface showing Riedel fractures Wind River Formation, Station MA1.

B.4 Normal (white pencil) & strike-slip (green pen) slickenlines, Flathead Sandstone, Station SH1.

B.5 Normal fault down to north, Wagon Bed Formation, Station SH2.

B.6 Normal faults down to north, Wind River Formation, Station SM1.

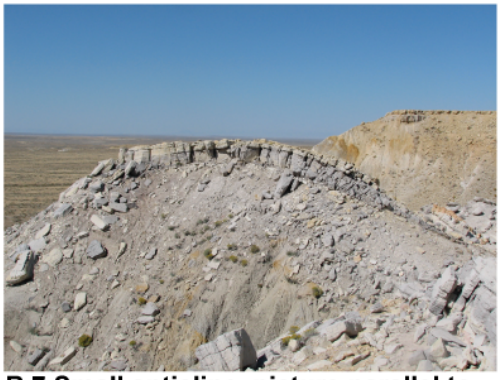

B.7 Small anticline, picture parallel to axis, Wind River Formation, Station MA2.

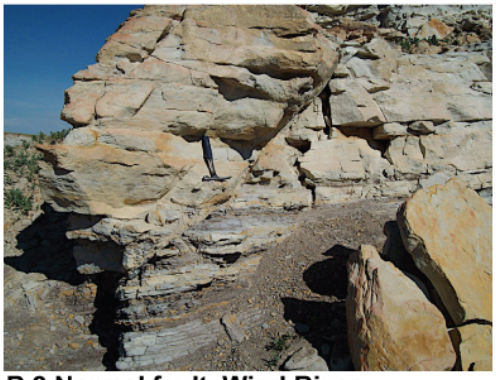

B.8 Normal fault, Wind River Formation, Station HHA4.

B.9 Clay-filled fracture, Wagon Bed Formation, Station SH2.

B.10 Sandstone fin showing hardened veneer, Lance Formation, Station HHA1.

B.11 Joint pavement directly on angular unconformity with Fort Union & Lance Formations, Wind River Formation, Station HHA4.